AD-A014 996

RESEARCH IN MATERIALS SCIENCE

D. J. Epstein, et al

Massachusetts Institute of Technology

Prepared for:

Advanced Research Projects Agency
Defense Supply Service

31 May 1975

TECHNICAL REPORT

ADA014996

275097

CENTER FOR
MATERIALS SCIENCE AND ENGINEERING

D D C

SEP 22 1975

B

Massachusetts Institute of Technology
Cambridge, Massachusetts 02139

REPORT DOCUMENTATION PAGE		READ INSTRUCTIONS BEFORE COMPLETING FORM
1. REPORT NUMBER	2. GOVT ACCESSION NO.	3. RECIPIENT'S CATALOG NUMBER
4. TITLE (and Subtitle) Research in Materials *Science*		5. TYPE OF REPORT & PERIOD COVERED Final Technical 1 June 1973 - 31 May 1975
		6. PERFORMING ORG. REPORT NUMBER
7. AUTHOR(s) R. Lagow		8. CONTRACT OR GRANT NUMBER(s) DAHC 15-73-C-0316
9. PERFORMING ORGANIZATION NAME AND ADDRESS Massachusetts Institute of Technology Center for Materials Science & Engineering Cambridge, Mass. 02139		10. PROGRAM ELEMENT, PROJECT, TASK AREA & WORK UNIT NUMBERS 3D10
11. CONTROLLING OFFICE NAME AND ADDRESS Defense Supply Service - Washington Room ID 245 - The Pentagon Washington, D.C. 20310		12. REPORT DATE 31 May 1975
		13. NUMBER OF PAGES 14
14. MONITORING AGENCY NAME & ADDRESS(if different from Controlling Office) ONR Resident Representative Massachusetts Institute of Technology Room E19-629 Cambridge, Mass. 02139		15. SECURITY CLASS. (of this report) Unclassified
		15a. DECLASSIFICATION/DOWNGRADING SCHEDULE

16. DISTRIBUTION STATEMENT (of this Report)

Unlimited

17. DISTRIBUTION STATEMENT (of the abstract entered in Block 20, if different from Report)

Unlimited

18. SUPPLEMENTARY NOTES

19. KEY WORDS (Continue on reverse side if necessary and identify by block number)

lithium, polylithium compounds, high temperature chemistry, organolithium compounds, polymeric intermediates, reactive intermediates

20. ABSTRACT (Continue on reverse side if necessary and identify by block number)

Recent work in our laboratory has resulted in the discovery of several new routes to polylithiocarbons, perlithiocarbons, and inorganic polylithium species. Previously for these classes of compounds, there were very few known examples, and there were no general synthetic routes in the literature. The new synthetic methods are all in the early stages of development and all involve the reaction of high temperature lithium vapor in the range of 800-1000°C with various organic, inorganic and polymeric species. During the

past year we have succeeded in the synthesis of the first perlithioalkanes, tetralithiomethane, $C(Li)_4$, and hexalithioethane, C_2Li_6. We have also prepared hexalithiobenzene, C_6Li_6, and presently have characterized over thirty such polylithium compounds. An intensive study of these species is now underway and efforts are underway to prepare other polylithiated species. It now appears that polylithiocarbons will be very useful reagents in organic synthesis as well as important monomers and crosslinking agents in polymer synthesis. The synthesis of several types of three dimensional polymers and high temperature materials is underway and is based on routes involving these new polylithium species. The preparation of a new series of diamond-like polymeric materials has been proposed and should result in a new class of high performance materials. Very significant progress has been made over the last year in the polymer area, although a significant amount of time and effort was spent on the construction of high temperature - high pressure apparatus for such syntheses. Polylithium compounds may also be useful as catalysts.

For Period - June 1, 1973 - May 31, 1975

Final Technical Report

RESEARCH IN MATERIALS SCIENCE

Sponsored By

Advanced Research Projects Agency
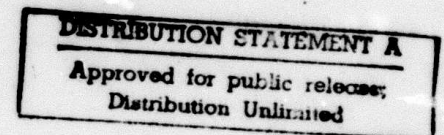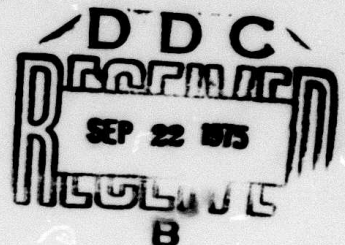
Contract No.   DAHC 15-73-C-0316

ARPA Order No.: 2469
Program Code No.: 3D10

Contractor:

Massachusetts Institute of Technology
Cambridge, Massachusetts   02139

Principal Investigator:

N. J. Grant (617) 253-5638

Project Scientists or Engineers:

I.   Optoelectronic Materials and Components: Miniaturized Thin Film
      Laser Sources and Modulators. D. J. Epstein (617) 253-4676

II.   Superconducting Transition Metal Alloys. R. M. Rose (617) 253-3230,
      M. MacVicar (617) 253-5617

III. Chemical Sythesis Using High Temperature Lithium Vapor Species,
      R. Lagow (617) 253-5617

Effective Date of Contract: June 1, 1973
Contract Expiration Date: May 31, 1975
Amount of Contract: $770,233

FINAL TECHNICAL REPORT

Period:	June 1, 1973 - May 31, 1975
Title:	Research in Materials Sciences
Project Title:	Optoelectronic Materials and Components: Miniaturized Laser Sources and Thin Film Modulators
Contract Number:	DAHC-15-73-C-0310
ARPA Order No.:	2469
Program Code No.:	3D10
Name of Contractor:	Massachusetts Institute of Technology Cambridge, Massachusetts 02139
Principal Investigator:	N.J. Grant, (617) 253-5638
Project Scientists or Engineers:	D.J. Epstein - (617) 253-4676 C.G. Fonstad - (617) 253-4634 H.P. Jenssen - (617) 253-6878 A. Linz - (617) 253-3208
Effective Date of Contract:	June 1, 1973
Contract Expiration Date:	May 31, 1975
Amount of Contract:	$770,233
Amount of Project:	$315,601

The views and conclusions contained in this document are those of the authors and should not be interpreted as necessarily representing the official policies, either expressed or implied, of the Advanced Research Projects Agency or the U.S. Government.

OPTOELECTRONIC MATERIALS AND COMPONENTS

MINIATURIZED LASERS AND THIN FILM MODULATORS

TABLE OF CONTENTS

(ii)

OPTOELECTRONIC MATERIALS AND COMPONENTS:
MINIATURIZED LASERS AND THIN FILM MODULATORS

I. INTRODUCTION

The research program described in this report was begun two years ago under ARPA support. It will be continued for another sixteen months beginning June 1, 1975, but, effective this date, responsibility for monitoring the program was transferred from ARPA to ONR. Were it not for this administrative change we would, at this time, be submitting our fourth Semiannual Progress Report. Because the transfer to ONR has involved the formal creation of a new contract, we are required to submit a "Final Report" even though the original tasks are continuing. As a consequence the present document lies somewhere between a progress and a final report. It is, on the one hand, more retrospective than a progress report, but on the other, is not quite the definitive document that we would submit as a final report. In particular, it does not stand alone as a complete and fully documented description of the research to date. For the full record the reader must also refer to our three previous Semiannual Technical Reports.

The research carried out under the subject contract has the following major objectives: (1) development of rare earth doped fluoride and oxide materials suitable for miniaturized optically pumped lasers; (2) development of LED pumps for these lasers; (3) growth and evaluation of electrooptical thin films suitable for optical modulators. Although the research is materials based, it is being carried out in a context which recognizes the interplay between materials development and device design. A summary of the accomplishments of the program is given in Table 1.

Table 1

Principal Accomplishments under
ARPA Contract DAHC-15-73-C-0316

Optoelectronic Materials and Components:
Miniaturized Laser Sources and Thin Film Modulators

I. Miniaturized Laser Sources

1. CW laser operation at 77°K of a 2.06 μm Ho:$\alpha\beta$YLF minilaser operating in internal reflection mode in 0.1 mm^3 dielectric cavity.

2. Experimental and theoretical studies of threshold as a function of temperature for several minilaser compositions.

3. Demonstration of importance of upconversion losses in determining laser threshold.

II. Light Emitting Diodes

1. Fabrication of GaAs:Si LED's matched to the 0.96 μm pump band of Yb^{3+}; external efficiency $\sim$ 1.5% into the air, $\sim$ 5% into laser crystal.

2. Study of growth parameters for Ga(As,Sb):Si system; fabrication of LED's having an emission bandwidth 25% narrower than for comparable GaAs:Si diodes.

3. Fabrication of 1.06 μm LED's from Ga(As,Sb) alloy system containing Si as amphoteric dopant.

III. Thin Film Electrooptics

1. Growth, by liquid phase epitaxy, of KTN films capable of light guiding; attenuation approx. 8db/cm.

2. Development of thin film modulator providing full modulation at 15 volts drive; good prospects for lowering drive voltage by a factor of at least three.

3. Demonstration of feasibility of growing multilayer electrooptic films.

IV. General

1. Installation of clean room for chemical preparation of crystal feed materials.

2. Development of solvent extraction techniques for synthesis of ultrapure materials.

3. Construction of holographic facility for fabrication of grating couplers.

The laser materials we have been studying involve a multiply sensi-tized dielectric host designed to be optically pumped by an LED having a spectral output matched to a sensitizer pump band. When we began our program we believed we had a good understanding of the important parameters that would enter into the design of an efficient minilaser. Early in the program we were able to demonstrate the basic validity of these design principles by obtaining lasing action in a 0.5 x 0.5 x 0.5 mm crystal of Ho-doped $\alpha\beta$YLF (LiY$_{0.45}$Er$_{0.5}$Tm$_{0.05}$:Ho), initially at liquid nitrogen tempera-ture and later up to 250°K. At the low temperature the crystal delivered a cw output of about 5 mw at a pump power of 150 mw supplied by a Kr ion laser pump. Laser oscillation occurred in an internal reflection mode, a configur-ation particularly attractive for integrated optics because it allows coupling to a waveguide structure by merely clamping the laser to the guide. In ex-pectation of obtaining improved minilaser performance we proceeded to grow and test a crystal of LiErF$_4$:Ho. To our initial surprise this crystal did not lase. It very quickly became clear that the presence of Tm was essential for getting a low laser threshold, and we have since been concerned with acquiring a de-tailed understanding, both theoretical and experimental, of the role played by this ion in the energy transfer process. Our recent studies of this problem are described in Sec. II where we report some very promising results obtained with Tm doped LiYbF$_4$:Ho, a crystal in which we hope to use the Yb absorption band at 0.96 μm for LED pumping.

Our original calculations of energy transfer were based on spectroscopic data obtained at low light levels. Our recent work has shown that, at pump levels approaching threshold, upconversion processes, which enter in a nonlinear way, begin to compete with direct transfer into the upper laser level. When Tm is added the direct transfer rate is enhanced relative to the upconversion rate and, consequently, the drain on the upper laser level via upcon-

version is inhibited. By designing a material with the proper concentration of Tm we can bring the threshold down to level compatible with LED pumps.

Our program to develop a minilaser has been instructive in a number of respects. It has forcefully demonstrated that progress in materials research is stimulated by device objectives that stretch materials requirements to the utmost. We would, in all probability, have not been too seriously concerned with upconversion losses had we not wanted to achieve low threshold lasing in the smallest possible volume. For example, the flash pumped αβYLF laser has been successfully developed with no consideration given, in the design, to nonlinear processes. Because the resultant laser has worked well there has been little impetus to inquire into the more subtle aspects of energy transfer. However, our results suggest that more careful attention to nonlinear effects might indeed lead to better material designs for all sensitized lasers. It is also clear that such designs will not be forthcoming unless spectroscopic studies of energy transfer are done in the nonlinear regime. This kind of research has been started under the contract and will be given more emphasis during the continuation of the program.

The diode pump program, described in Sec. III, has several distinct aspects: (1) the tailoring of materials to provide a diode emission spectrum matched to a sensitizer pump band; (2) the design and fabrication of suitable geometries for efficient pumps; (3) test and evaluation of finished diodes.

We are now producing GaAs:Si diodes that match the Yb^{3+} pump band at 0.96 μm and operate with internal efficiencies exceeding 50%, and are also investigating the materials system $GaAs_{1-x}Sb_x$:Si which has a narrower bandgap than GaAs. We have shown, as originally hypothesized, that LED's in the latter

system have a considerably narrower emission spectrum than comparable GaAs:Si diodes. A significant result of the Ga(As,Sb) work has been the demonstration of relatively efficient luminescence at 1.06 μm from Si-doped $GaAs_{0.94}Sb_{0.06}$. The low loss and low pulse dispersion of fibers at 1.06 μm makes this wavelength extremely important for fiber optic communications systems; for such systems, $GaAs_{1-x}Sb_x$ looks very attractive when compared with the alternatives, $In_xGa_{1-x}As$ and InP. The use of silicon doping is significant in that it introduces deep acceptor levels which give longer wavelength emission for much lower alloy compositions than would be achieved with, for example, zinc doping.

In the immediate future we will continue the development of GaAs:Si pump diodes. The areas in which improvements can be made include better junction heat sinking, elimination of optically inactive junction areas, improved contacts, and increased overall efficiency. Our calculations show that the LED's being developed should provide a pump flux adequate for cw operation of a Ho minilaser at room temperature.

We will also continue our study of $GaAs_{1-x}Sb_x$ sources at 1.06 μm because this is a wavelength not accessible to GaAs and because once efficient high brightness $GaAs_{1-x}Sb_x$ sources at 1.06 μm are developed it will be a trivial matter to also produce them at 0.96 μm for pumping Yb sensitized minilasers.

In Sec. IV we describe our success in the growth by liquid phase epitaxy of KTN films capable of guiding light. KTN is a material particularly attractive for thin film optical devices, because, for certain compositions, it has an electrooptic coefficient considerably higher than found in other materials and, consequently, is well suited to electrooptic applications that require low drive voltage. Using one of our films, we have fabricated

a light modulator that provides nearly full amplitude modulation at about 15 volts drive. By modifying the film composition and with a slight redesign in device configuration we should be able to reduce the drive by at least a factor of three.

Our original films had an excessively high optical attenuation, about 28 db/cm. As a result of more experience with the growth procedure we have been able to reduce the loss to about 8 db/cm. The growth process is not yet fully under control and will be looked at in considerably greater detail during the remainder of the program.

A brief discussion of some of the electromagnetic issues involved in coupling an internal-reflection laser to a thin film waveguide is given in Sec. V. (For greater detail the reader should consult Semiannual Technical Reports 2 and 3). When the refractive index of the laser host is sufficiently large relative to the guide index it is possible to couple from laser to guide via the evanescent field of the laser cavity mode. This method is not possible in general so other coupling methods must be found. One desirable scheme involves the introduction of a dielectric grating into the coupling region, the grating wavelength being chosen to compensate for the phase mismatch between the laser and waveguide modes. A holographic facility to construct such gratings has been built and satisfactory test gratings have been fabricated.

Success in developing optically pumped lasers depends in no small way on the ability to prepare single crystals of excellent optical quality, free of all contaminants. It has not been generally recognized that the preparation of such crystals requires control over the purity of chemicals and feedstocks

to a degree comparable to that required in semiconductor technology. The techniques ordinarily used for synthesizing fluoride and oxides for laser hosts fall considerably short of yielding the required purity and, consequently, we have had to develop the special processes for feed preparation described in Sec. VI. Careful attention to purity must be paid to each chemical component entering into the synthesis and extreme care must be taken to avoid recontamination as one proceeds from step to step. Materials are synthesized and purified by solvent extraction in a class 100 air clean room, further purified (when required) in a specially designed zone refiner, and grown under computer control in a controlled atmosphere furnace. The expertise we have acquired in developing the required purification and growth techniques puts us in a unique position to carry out laser studies in crystals of a quality not generally available to others.

II. MINILASER DEVELOPMENT

2.1 Material Design

The design of an efficient optically pumped minilaser requires a material with a number of important features:

1. a large cross-section for stimulated emission;

2. a long lifetime for the upper laser level;

3. a high absorption cross-section at the wavelength of the pump light;

4. efficient transfer of energy from the pump level (or levels) to the upper laser state;

5. low probability for de-excitation of the upper laser level by upconversion processes.

A material such as Nd:YAG, despite its general success, fails as a minilaser because it does not efficiently absorb pump light. The absorption can be enhanced by increasing the Nd concentration but the resultant interaction among Nd ions quenches the fluorescence and raises the lasing threshold. The inherent problem in Nd:YAG is that the Nd ion plays the dual role of activator (lasing ion) and sensitizer (absorber of pump light*), and , in YAG, it cannot perform both functions well at the same time. Our interest has been in material systems where the sensitizer and activator functions are separately provided by ions specifically selected for each task. A notable example is Ho: $\alpha\beta$YLF (Ho: $LiY_{1-x-y}Er_xTm_4F_4$) which contains Ho as the lasing ion, Er as the ion designed to absorb pump light and Tm to assist in the transfer of energy between the excited Er levels and the upper laser level of Ho.

Laser systems that employ sensitizer and activator combinations allow great flexibility in design. In particular, as shown in Table 2, it becomes possible to

---

* An ion that does not directly absorb pump light but assists in the transfer of energy to the lasing ion is also a sensitizer.

Table 2

Activator - Sensitizer Combinations for
LED Pumped Lasers

Activator Ions	Sensitizer Ions	Laser Wavelengths	Pump Band
Ho^{3+} $^5I_7 - {}^5I_8$	Er^{3+}	2 μm	1.50 μm
Ho^{3+} $^5I_7 - {}^5I_8$	Ni^{2+}	2 μm	1.20 μm
Ho^{3+} $^5I_7 - {}^5I_8$	Yb^{3+}	2 μm	0.96 μm
Tm^{3+} $^3H_4 - {}^3H_6$	Er^{3+}	1.8 - 1.9 μm	1.50 μm
Tm^{3+} $^3H_4 - {}^3H_6$	Yb^{3+}	1.8 - 1.9 μm	0.96 μm
Tm^{3+} $^3F_4 - {}^3H_6$	Yb^{3+}	~1.5 μm	0.96 μm
Tm^{3+} $^3F_4 - {}^3H_5$	Cr^{3+}	2.3 μm	0.65 μm
Tm^{3+} $^3F_4 - {}^3H_5$	Yb^{3+}	2.3 μm	0.96 μm
Nd^{3+} $^4F_{3/2} - {}^4I_{11/2}$	Cr^{3+}	1.06 μm	0.65 μm

conceive a multiplicity of lasers compatible with LED pumps. However, the development of such lasers requires a clear understanding of the details of energy transfer between sensitizer and activator ions. It is our intention, eventually, to study transfer processes, in various hosts, for all activator/sensitizer pairs listed in Table 2. To date, however, our studies have been limited to Er^{3+} and Yb^{3+} as sensitizers in fluoride hosts containing Ho^{3+} as the activator. These studies and their implications for minilaser development are described below.

2.2 Er^{3+} Sensitized Ho^{3+} Lasers

In Semi-Annual Technical Report No.2 it was reported that laser action could not be achieved in $LiErF_4$:0.3% Ho even though our earlier spectroscopic measurements had shown high transfer efficiency from Er^{3+} to the $Ho:^5I_7$ level. The failure of this particular composition to lase was surprising in view of the fact that laser operation is easily obtained in the closely related αβYLF compositions, e.g. $LiY_{0.5}Er_{0.5}Tm_{0.05}F_4$:0.25% Ho. It was suspected that the disparity might be due to the role played by Tm in energy transfer, particularly at high pump intensity. Accordingly, experiments were performed to measure the Ho^{3+} fluorescence in both materials as a function of pump intensity up to values typically encountered under lasing conditions.

In these experiments optically thin samples of $LiErF_4$:0.3% Ho and $LiY_{0.5}Er_{0.5}Tm_{0.05}F_4$:0.25% Ho were pumped at 514.5 nm with a cw argon laser. The pump beam was focused to a spot 100 μm in diameter and power up to 4 watts was used. To reduce sample heating, the pump beam was chopped at low duty cycle and special care was taken to heat sink the samples. Fluoescence was monitored with a 0.3 m monochrometer; a liquid nitrogen cooled InAs detector was used to measure the 2 μm $Ho:^5I_7$ fluorescence and the 1.2 μm $Ho:^5I_6$ fluorescence was measured with a photomult-

iplier. Neutral density filters were used to attenuate the fluorescence so that each detector always operated in its linear range.

The dependence of the $Ho:^5I_7$ fluorescence on pump power for the two materials is shown in Fig. 2.1. At low pump intensities the fluorescence is linearly proportional to pump power and the experimentally determined ratio of the fluorescence efficiency in $LiErF_4$ to that in $\alpha\beta YLF$ is 1.3. This value is to be expected because in $\alpha\beta LF$ the transfer quntum efficiency from the $Er:^4S_{3/2}$ pump level (Fig. 2.2) to the $Tm:^3H_4$ - $Ho:^5I_7$ system is $\sim$ 3. Because half the energy in the $Tm:^3H_4$ - $Ho:^5I_7$ system is in the $Ho:^5I_7$ level, the net transfer efficiency is $\sim$ 3/2. The transfer quantum efficiency for $LiErF_4$: Ho is $\sim$ 2, and, consequently, its fluorescence efficiency should be $\sim$ 4/3 that of $\alpha\beta YLF$.

As the pump power is increased, the $LiErF_4$: Ho fluorescence saturates at a level approximately 1/2 that needed for laser threshold. The $\alpha\beta YLF$ fluorescence continues to increase although it also shows a decrease in transfer efficiency.

To see why $Ho:^5I_7$ fluorescence saturated, the $^5I_6$ fluorescence was also monitored (Fig. 2.3). At low pump intensities the $Ho:^5I_6$ fluorescence varies quadratically with pump power, a dependence characteristic of fluorescence arising from an upconversion process. We believe the upconversion involves the transition $Er:^4I_{13/2}$, $Ho:^5I_7 \rightarrow Er:^4I_{15/2}$, $Ho:^5I_5$ with the $Ho:^5I_5$ decaying rapidly to the fluorescing level $Ho:^5I_6$ by multiphonon emission. At higher pump powers the functional variation of the fluorescence takes on a linear dependence as the $Ho:^5I_7$ population saturates. Beyond this point the effect of the pump is to increase the occupation of the $^5I_6$ level. As this level becomes more heavily populated the fluorescence continues to increase, but at a sublinear rate, and when the level eventually saturates, the fluorescence becomes independent of pump power.
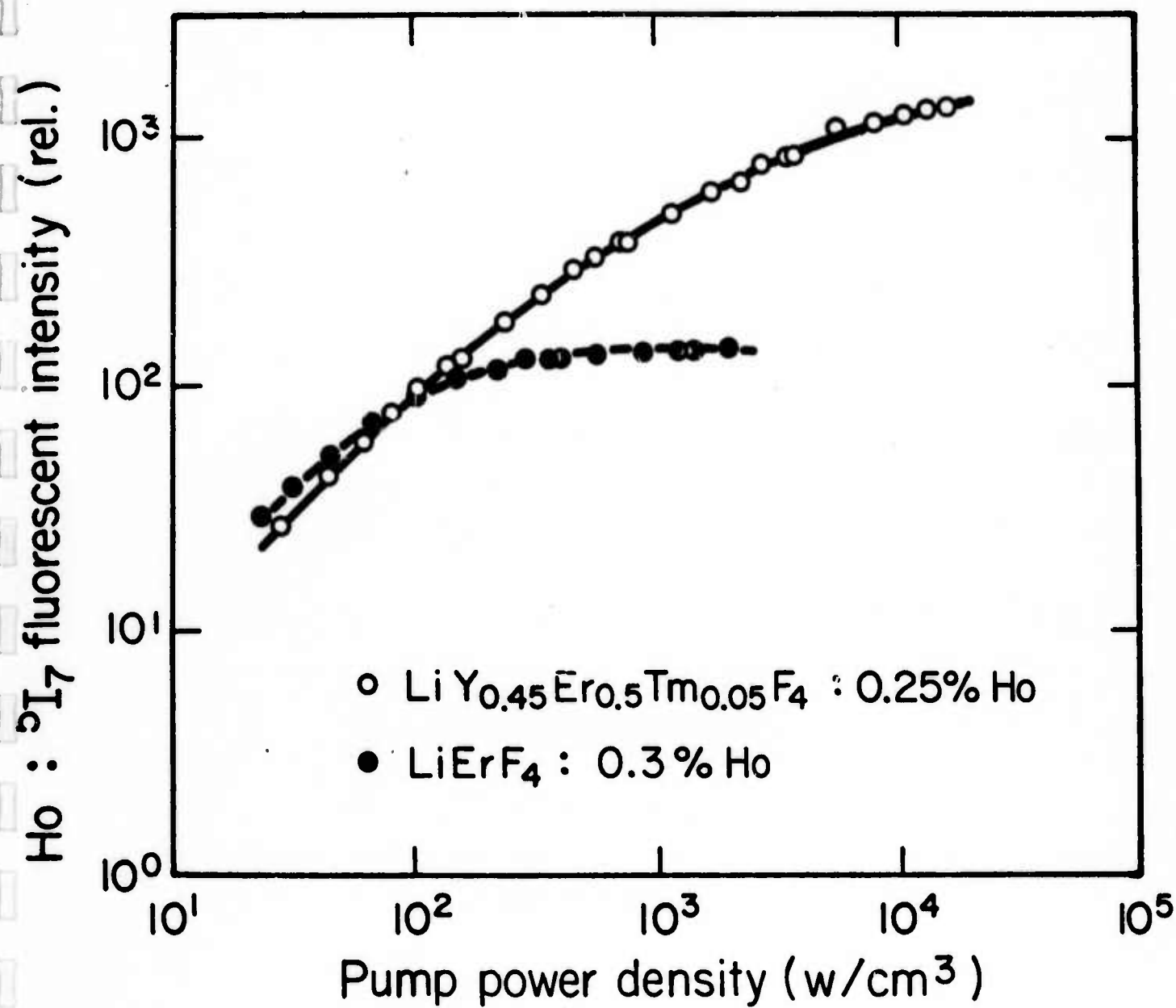
Fig. 2.1 Dependence of Ho:^{5}I$_7$ fluorescence on pump power density.
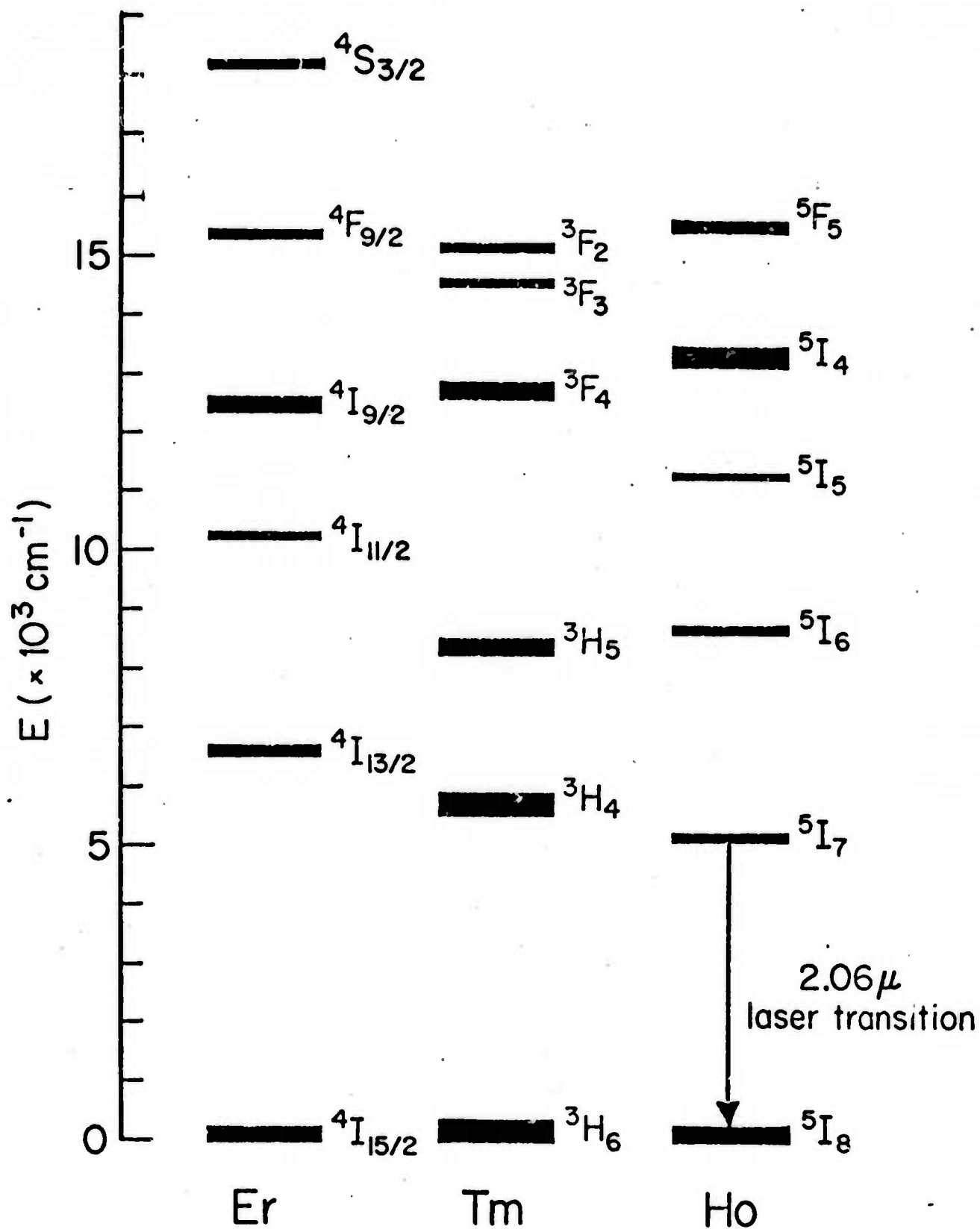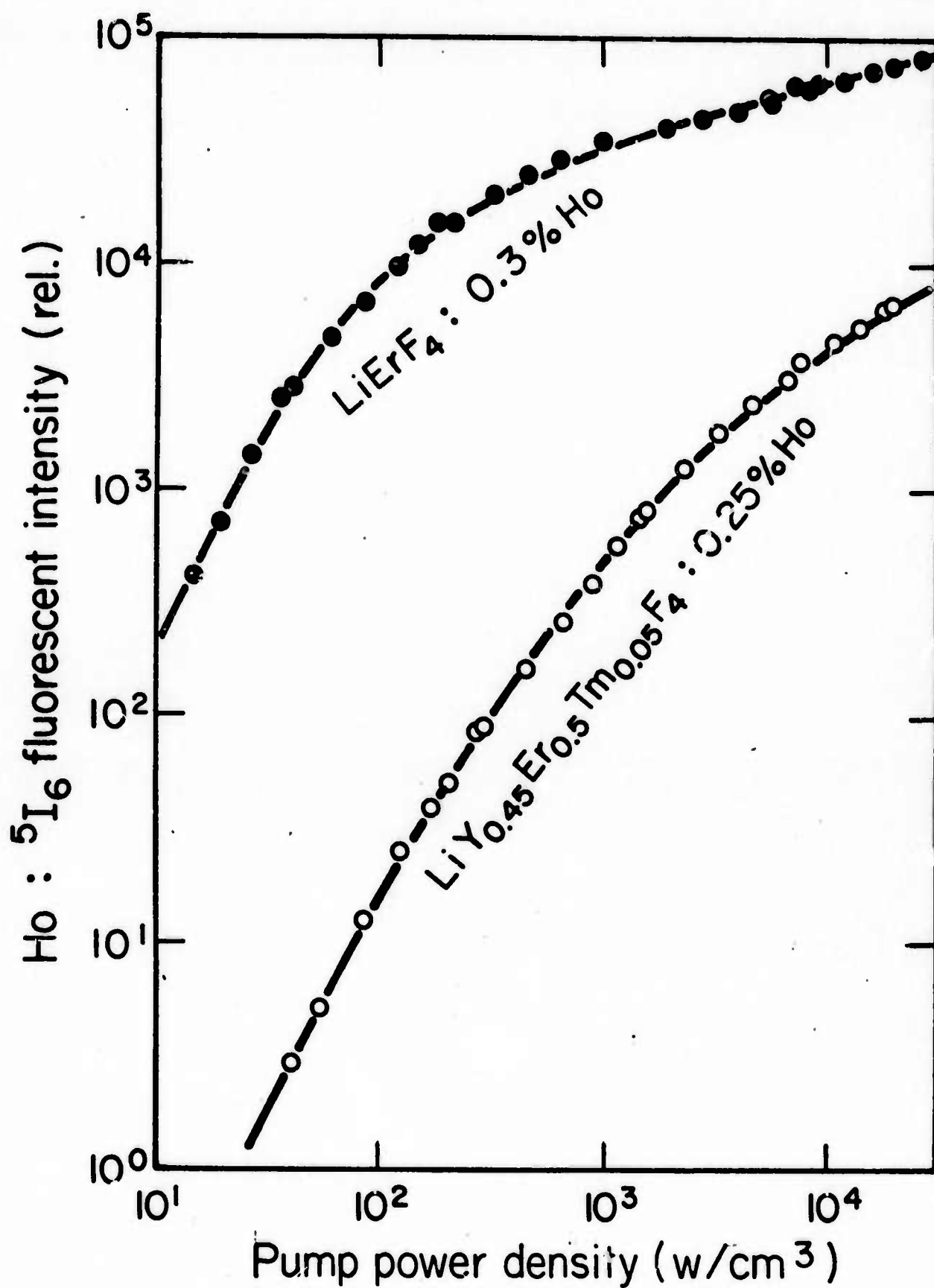
Fig. 2.2   Energy levels of Er, Tm, and Ho in YLF.

Fig. 2.3 Dependence of Ho:$^5I_6$ fluorescence on pump power density.

This situation is very similar to that in the Yb-Tm system which was discussed in Semi-Annual Technical Report No.3. There it was shown that upconversion can cause fluorescence saturation at a level far below that needed for laser operation. The important role of Tm is now easily seen. In LiErF$_4$:Ho, energy transfer from the Er:^{4}I$_{13/2}$ to Ho:^{5}I$_7$ is fast (0.8 ms) compared to the Er:^{4}I$_{13/2}$ fluorescent lifetime (15 ms) so that the transfer efficiency is high, but it is slow compared to the transfer time in αβYLF (< 10 μs). The faster transfer provided by Tm more effectively drains the Er:^{4}I$_{13/2}$ level and thereby inhibits the upconversion step.

Upconversion may also be limiting the performance of αβYLF as evidenced by the following facts. When the Er:^{4}I$_{13/2}$ level in αβYLF is pumped with 1.5 μm light, fluorescence is observed at 1.2 μm from the Ho:^{5}I$_6$ level. Also, when αβYLF is flash-lamp pumped at intensities near that needed for laser threshold, the Ho:^{5}I$_7$ lifetime is ∿ 7 ms as compared to 13 ms at low intensity pumping. Thus the Ho:^{5}I$_7$ level is ∿ 50% quenched, perhaps by the upconversion process. More accurate measurements of transfer rates and system modeling is needed to fully understand this problem

2.3 Yb^{3+} Sensitized Ho^{3+} Laser

In our program to develop laser materials suitable for LED pumping we chose to concentrate initially on fluoride hosts containing Yb^{3+} as a sensitizer for Ho^{3+}. Ytterbium is a desirable sensitizer ion because it has a pump band at 0.96 μm (see Table 2), a wavelength where we know it is possible to build reliable, high brightness LED's.

In previous studies of Yb → Ho energy transfer (see Semi-Annual Technical Report No.3) we had concluded that it would be necessary to dope LiYbF$_4$:Ho with Tm to obtain an energy transfer rate large enough to avoid the deleterious effects of upconversion loss. The analysis indicated in particular, that efficient lasing should be

obtainable in $LiYb_{0.95}Tm_{0.05}F_4$:0.25% Ho. A crystal having this composition was grown and, as predicted, showed good performance in laser operation.

In this material pump energy absorbed by Yb^{3+} is quickly and efficiently transferred to the $Tm:^3H_4$ level (Fig. 2.4) and then transferred in a second rapid step to the upper laser level $Ho:^5I_7$. The addition of 0.25% Ho does not significantly alter the first step in the transfer process because we know that in $LiYbF_4$ doped only with 0.25% Ho the transfer from $Yb:^2F_{5/2}$ to $Ho:^5I_7$ is slow and inefficient.

Not all the transferred energy ends up in the $Ho:^5I_7$ level. It was pointed out in Semi-Annual Progress Report No.2 that the $Ho:^5I_7$ and $Tm:^3H_4$ levels are in good enough thermal contact to ensure thermal equilibrium between these levels. For the 20:1 Tm to Ho ratio occurring in our particular crystal the excitations, at room temperature, are about equally divided between the two levels as a result of thermalization.

Laser performance was evaluated using a crystal wafer 2.0 mm long with plane parallel end faces to which evaporated silver mirrors were applied (Fig. 2.5). The crystal was mounted on the cold finger of a liquid nitrogen dewar. A linear tungsten filament was imaged onto the crystal to form a gain region 2.0 mm x 0.5 mm on the crystal's surface.

The effective pump power density $w(x)$ at a distance x into the crystal can be found from the expression

$$w(x) = \int \alpha(\lambda)e^{-\alpha(\lambda)x} \phi(\lambda) \, d\lambda \qquad (2.1)$$

where $\phi(\lambda)$ is the spectral irradiance of the pump light at the crystal surface, $\alpha(\lambda)$ is the absorption coefficient of the $Yb:^2F_{5/2}$ absorption band and the integral is taken over the entire absorption band. The function $\phi(\lambda)$ was obtained by combining
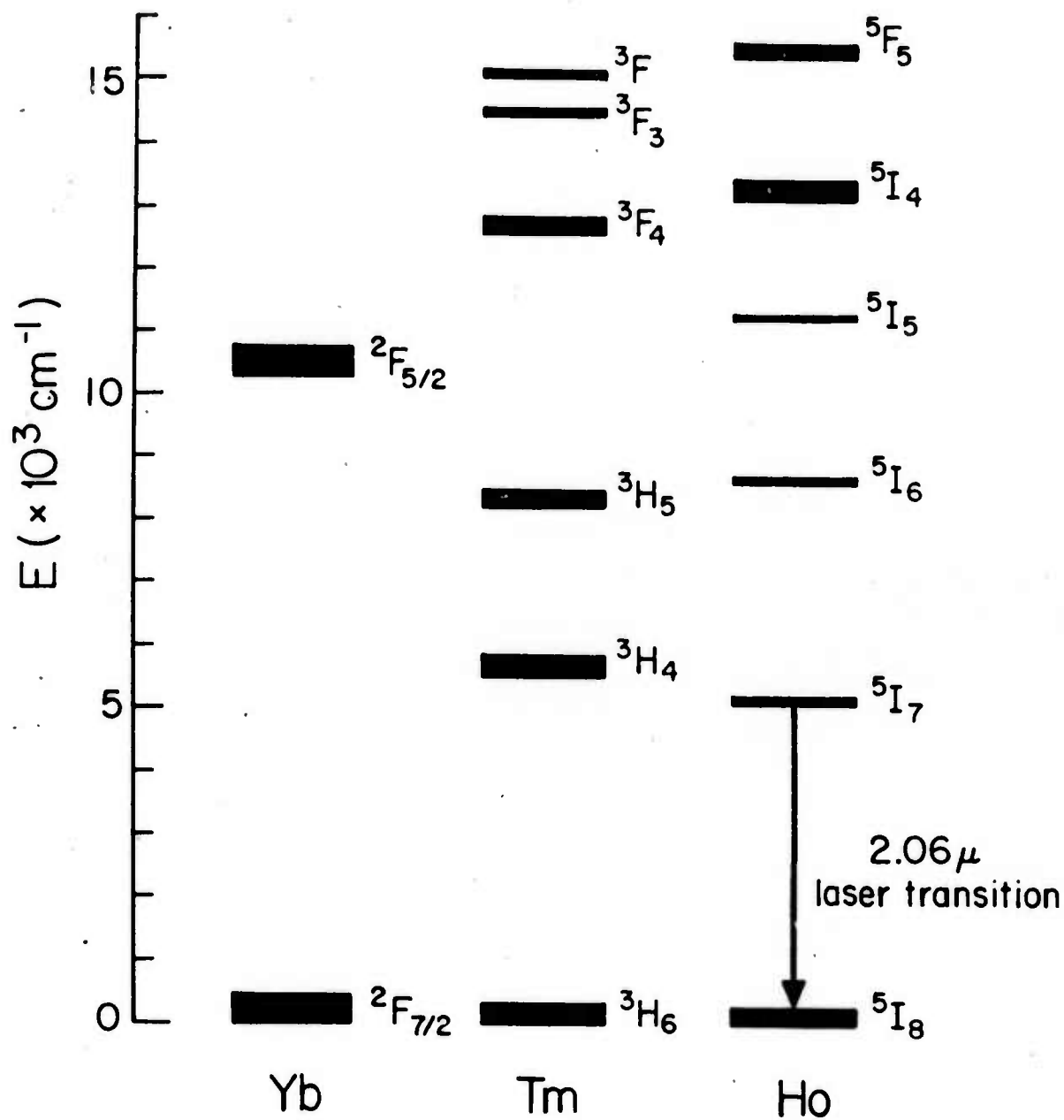
Energy Levels for the Ions Yb^{3+}, Tm^{3+}, Ho^{3+}

Fig. 2.4
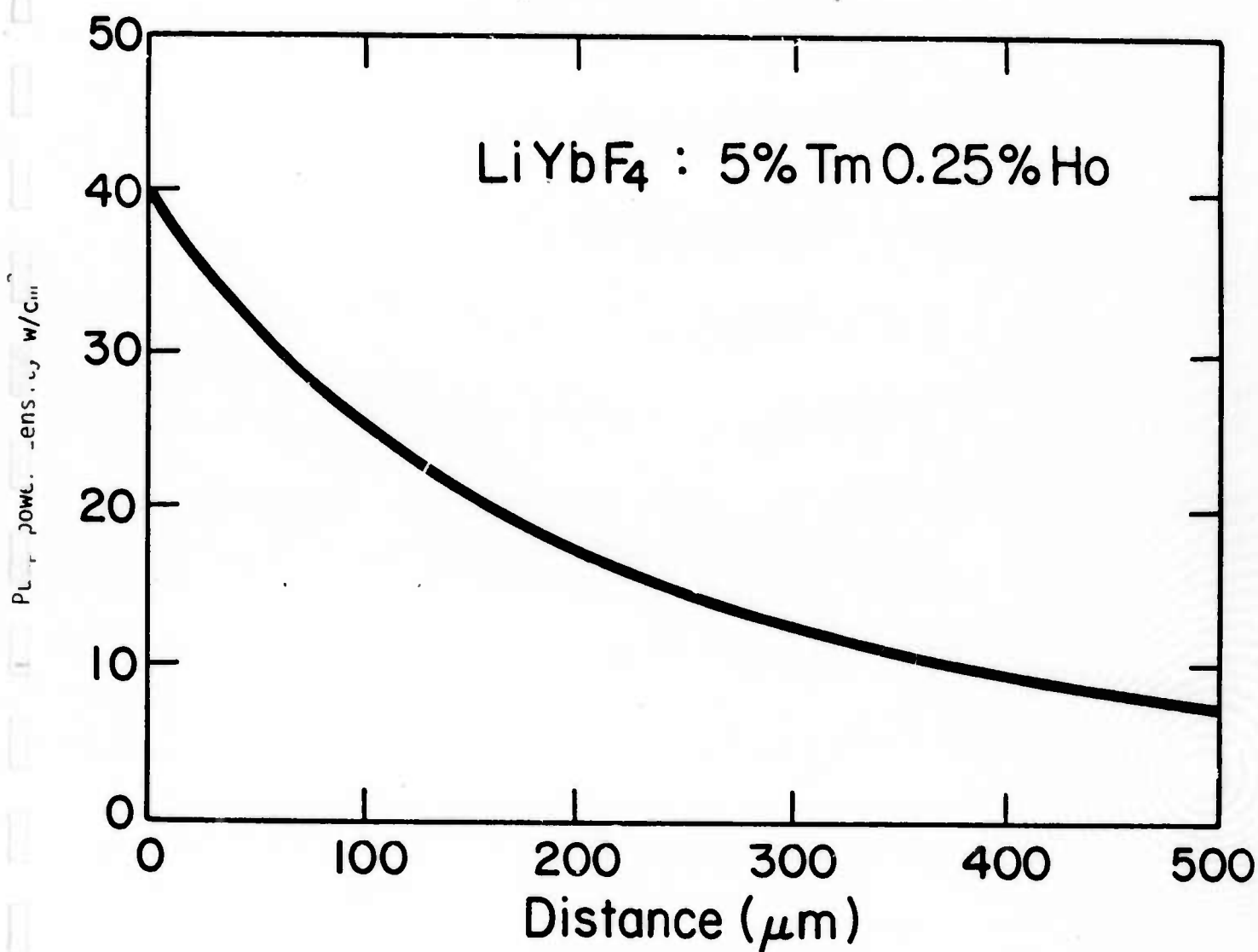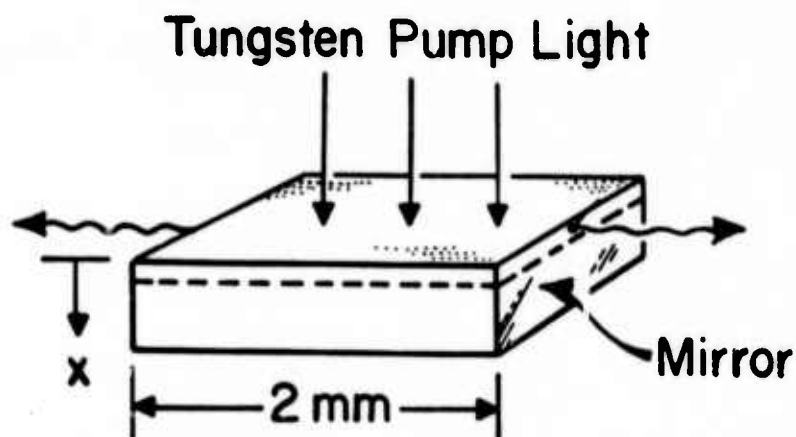
Fig. 2.5   Distribution of pump power density at threshold;for
           tungsten pump.

the known form of the spectral irradiance of the tungsten lamp with a calibration measurement that established the irradiance level at one point on the spectral curve. By numerically integrating Eq. 2.1 we can obtain the distribution of the pump power density in the sample at threshold (Fig. 2.5). From the measured divergence of the output beam, about 1%, we conclude that the lasing volume is approximately 100 μm thick. It follows from Fig. 2.5 that the average pump power density is about 35 watts/cm^3.

To see if the measured pump power density at threshold is a reasonable value, we can predict what it should be by making the following assumptions: (1) the temperature of the crystal is 80°K, (2) the energy transfer quantum efficiency from Yb to Ho is unity, and (3) the reflectivity of the mirrors is 98.5%. The threshold pump power desnity w_{th} is then given by

$$w_{th} = \frac{hc(L_0 + L_R)}{2\lambda_p f_u \tau \sigma L} \tag{2.2}$$

where h is Planck's constant, c the velocity of light, λ_p the pump wavelength, f_u the fraction of excited ions in the upper laser level, τ the fluorescence lifetime of the upper laser level, σ the stimulated emission cross-section, and L is the length of the crystal. L_0 is the non-resonant round trip cavity loss; assuming only mirror losses, $L_0 = 2\ln(\frac{1}{R})$, where R is the mirror reflectivity. L_R is the resonant loss and is given by $L_R = 2\sigma N f_1 L$, where N is the concentration of lasing ions in the material and f_1 is the occupation factor of the lower laser level. For the assumptions above, the calculated threshold pump power is 29 w/cm^3, in good agreement with the experimental value.

2.4 LED Pumping Considerations

Optical pumping of sensitized materials with light emitting diodes is potentially very efficient since the diode's emission can be matched to the broad Yb absorption

band as shown in Fig. 2.6. Also shown is the emission spectra of a Si-doped GaAs LED with peak emission at 967 nm and a full linewidth at half maximum intensity of 600 nm. For this LED the pump power density varies with distance into the sample as shown in Fig. 2.7; the curves, calculated from Eq. 2.1, are normalized to a source intensity of 1 w/cm^2 at the sample surface.

Because the peak diode emission shifts with temperature and Si concentration it is important to know how the pump light absorption varies as the peak is shifted. The result is shown in Fig. 2.8.

For the tungsten-lamp pumped laser described above a threshold power density of 35 w/cm^3 was required. Based on the results shown in Fig. 2.7 and using the average of the σ and π absorption coefficients, we conclude that, at liquid nitrogen temperature, threshold can be obtained with about 1 w/cm^2 flux from an LED. This is not a severe requirement and, indeed, this threshold flux can probably be reduced somewhat by using higher quality mirrors to reduce the laser resonance loss which, at low temperature, is the dominant factor in determining threshold. At room temperature, laser threshold is determined mainly by resonant loss of the large terminal-level population. For room temperature LED pumped operation of LiYbF$_4$: 5% Tm, 0.25% Ho, the threshold pump power can be calculated from Eq. 2.2. Neglecting resonator losses, 280 w/cm^3 is needed for threshold. This will require 75 w/cm^2 flux from LED. We point out in the following section that this flux level is within the design range of the LED's we can fabricate.
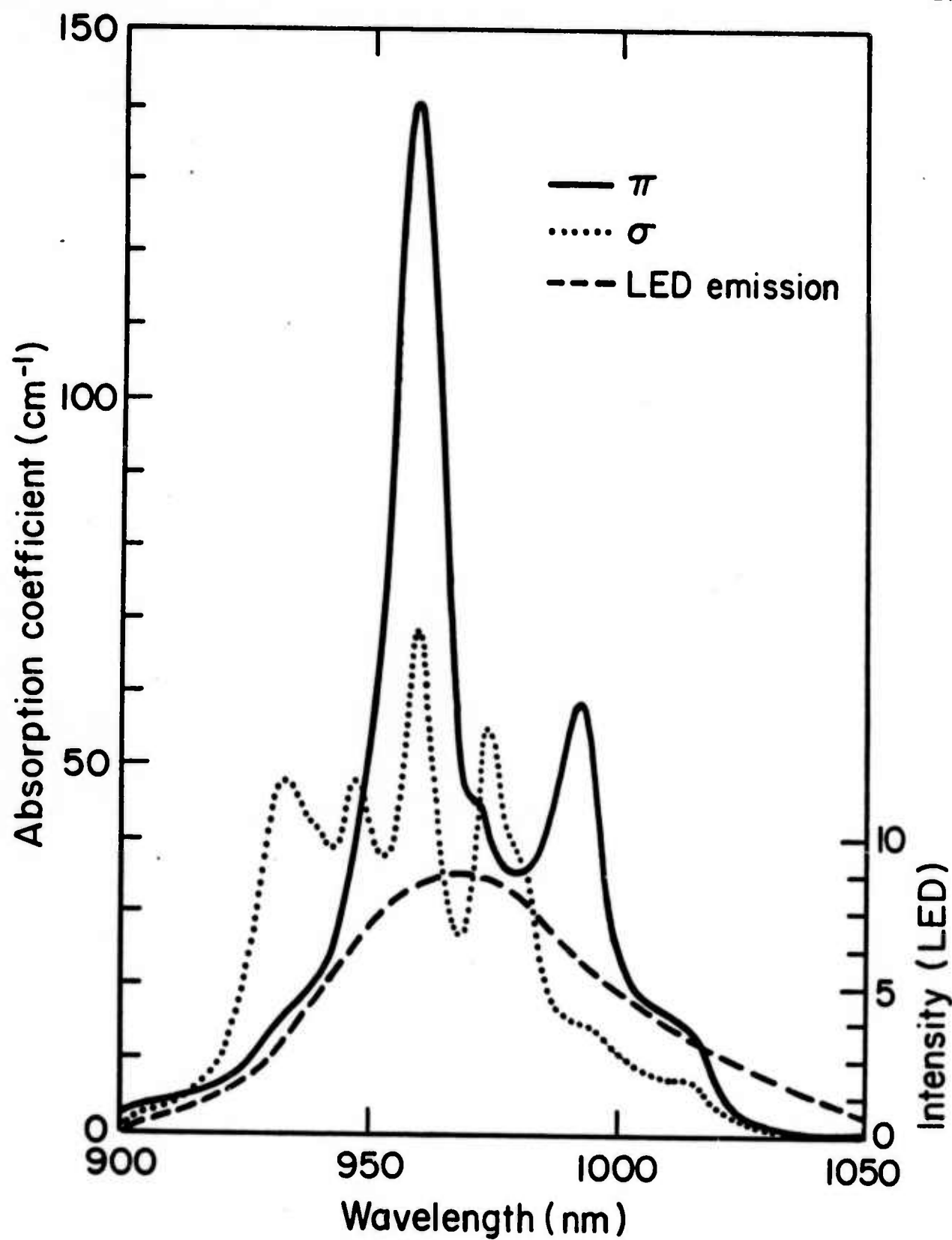
Fig. 2.6 Room temperature absorption coefficient of LiYbF$_4$ vs. wavelength. Typical LED emission spectrum is also shown.
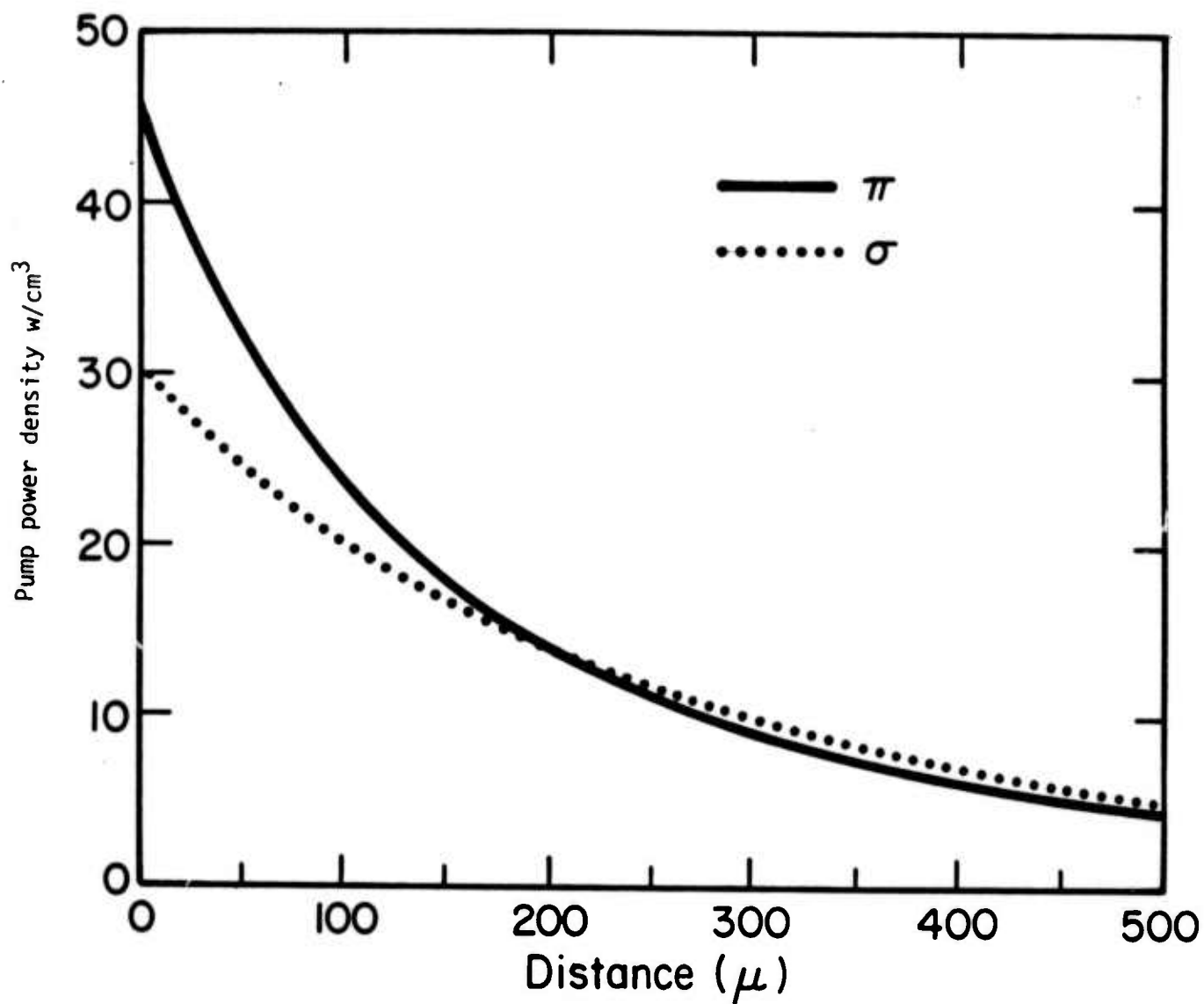
Fig. 2.7 Distribution of power density in laser crystal for LED pump having spectral distribution shown in Fig. 2.6. Vertical scale is normalized for LED supplying 1 w/cm^2 at crystal face.
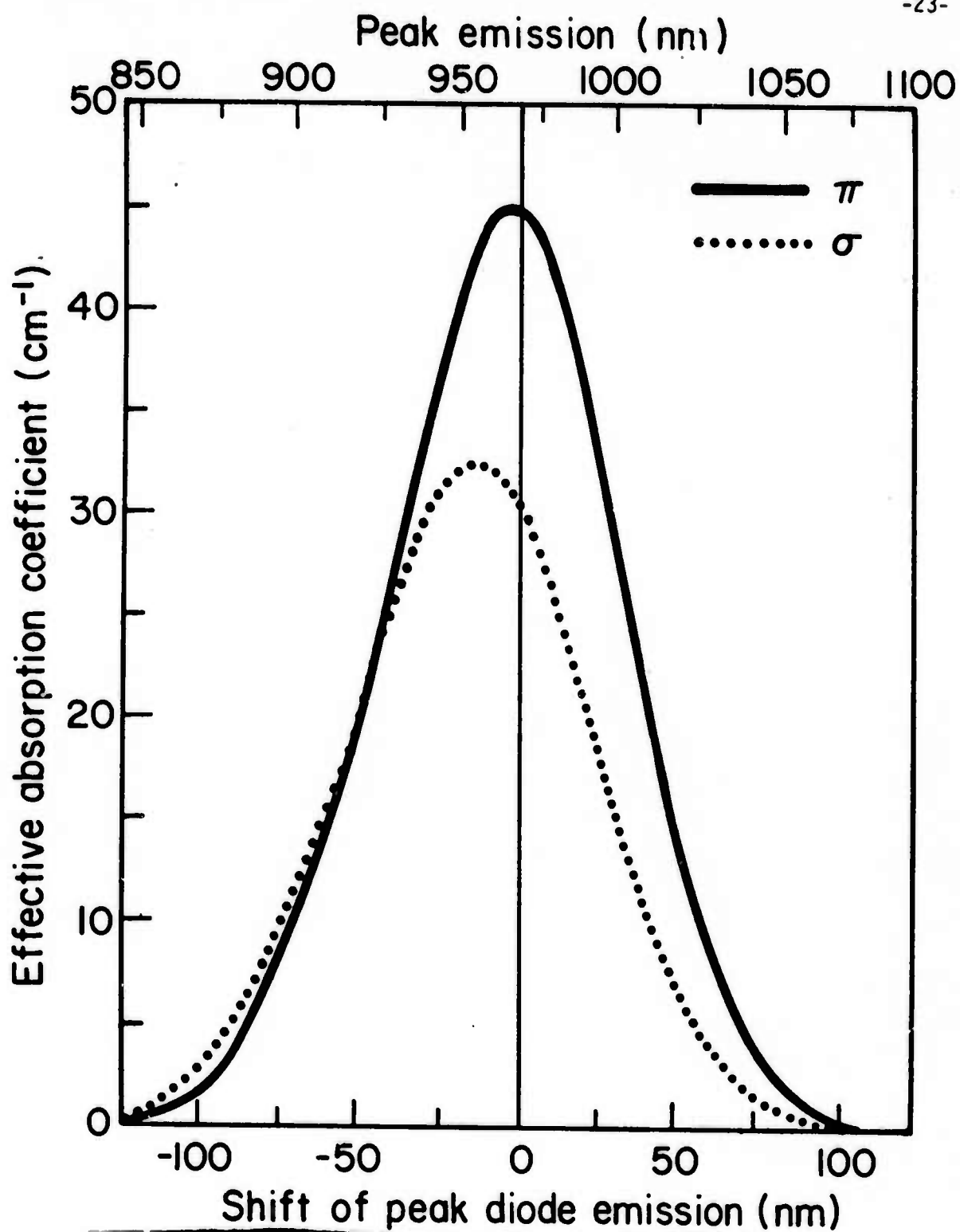
Fig. 2.8 Effective absorption coefficient for LED pumped
LiYbF$_4$ vs. shift of peak diode emission. Zero
shift is for a LED with peak emission at 967 nm.

III. DIODE PUMPS

3.1 Diode Pumps Program Objectives and Structure

There have been two distinct aspects to the program to develop semiconductor light emitting diodes designed specifically to pump minilasers: (1) the design of suitable device geometries, the development of fabrication procedures to realize them, and their testing and evaluation, and (2) the tailoring through materials development efforts of the diode emission spectrum to optimally, efficiently, and adequately pump the laser absorption or "pump" band at 0.96 μm. The latter aspect of the effort has led to the study of gallium arsenide antimonide ($GaAs_{1-x}Sb_x$) a material we have found to be extremely exciting not only for this application but also for potential use as 1.0 to 1.1 μm LEDs and laser diodes for fiber optical communications. We have recently begun considering the quarternary, aluminum gallium arsenide antimonide ($Al_yGa_{1-y}As_{1-x}Sb_x$), for use in heterostructure devices with $GaAs_{1-x}Sb_x$, and find that this pair is superior to the alternative of indium gallium arsenide ($In_yGa_{1-y}As$) and indium gallium arsenide phosphide ($In_yGa_{1-y}As_{1-x}P_x$) because of the insensitivity of the lattice constant to the aluminum fraction. We, thus, find ourselves at the forefront of material research on the Ga(As,Sb)/(Al,Ga)(As,Sb) system. which we feel will be the primary system used in sources for optical fiber systems, and ultimately in monolithic semiconductor integrated optical circuits in the future. These issues will be discussed further in Section 3.4.

For pumping the solid state minilasers, the diodes will have planar emitting surfaces to which the lasers can be intimately attached, and they will be designed to deliver the maximum amount of radiation into the laser rod. They will further be constructed so that the junction can be well heat-sunk to permit operation at high current levels, $\sim$ 500 A/cm^2.

Optimally matching the emission spectrum to the laser rod absorption band requires as narrow an emission band as practical, peaking at the laser absorption maximum. To achieve this, two approaches are being followed: (1) the use of silicon-doped gallium arsenide (GaAs) diodes, and (2) the use of silicon-doped gallium arsenide antimonide ($GaAs_{1-x}Sb_x$) diodes. Both systems emit further into the infrared than do conventional zinc-doped GaAs LED's required to match the Yb^{3+} pump band and each has its own particular advantages. The GaAs:Si system, for example, has been the subject of considerable study so that our work with it is as much development as research. We have consequently been concerned in this program with developing our own capability to grow the required diode layers, with tailoring the pump diode emission spectrum, and with maximizing the emission intensity and overall pump efficiency. The $GaAs_{1-x}Sb_x$ system, on the other hand, is much more poorly understood and the work on this system is considerably more basic, requiring us to start with the determination of parameters in the growth system and the behavior of dopants in the alloy system. This system was chosen over $In_yGa_{1-y}As$ because it looked to be equally as good and had not been widely studied. Our preliminary investigations of $Al_yGa_{1-y}As_{1-x}Sb_x$, the companion quaternary to $GaAs_{1-x}Sb_x$, now make it look superior, as we will discuss.

To summarize: the diode minilaser pump program's two aspects of device design and materials development, are being addressed via three primary efforts, or thrusts: (1) the design, fabrication (including technology development), and evaluation of specialized diode geometries; (2) the growth, testing, and evaluation of Si-doped GaAs LED's with emission tailored to pump the Yb^{3+} minilaser absorption band and with efficient, high intensity output; and (3) the growth and characterization of Si-doped $GaAs_{1-x}Sb_x$ LEDs in order to fully understand this system and to evaluate it for ultimate use as pump diodes and optical fiber sources.

Initial diodes and minilaser-diode structures will evolve from a combination of the results of efforts 1 and 2 above. Further structures will involve more sophisticated, heterostructure diode geometries and materials developed in the third effort. In the following sections we will summarize progress in each of these areas during the last twenty-four month period, concentrating on results of the last six months.

3.2 Diode Fabrication and Evaluation

Device development efforts have concentrated on the pump diode geometry illustrated in Figure 3.1. This device is designed to side-pump square cross-section "ring" or internal reflection mode lasers. The fabrication sequence for an earlier version of this device is illustrated in Figure 3.2. An ordinary micro-photograph of a typical device is shown in Figure 3.3a; Figure 3.3b shows the same device, viewed under an infrared microscope, with a current through it of 60 mA. The center emitting area is approximately 1.5×10^{-3} cm^2; and the current density is ~ 20 A/cm^2. Both of the devices shown in this figure are of the earlier design.

Comparing Figure 3.1, and the devices illustrated in Figure 3.2 one can see some changes which have been made from the latter, earlier devices. The most important change has been the inversion of the substrate and epi-layers, that is, the emitting surface is now the substrate. This change is expected to have significant advantages for high current operation and uniformity of emission, because the junction region, where heating occurs, is a factor ten closer to the header and heat sink, and because the contact to the thin p-type layer is now a large area contact. The new contact scheme reduces the spreading resistance problem[*]

---

[*] This is the problem of the voltage drop due to current flowing from the contact at the edge of the emitting area to points near the center of the emitting area keeping the diode from turning on in the center and leading to non-uniform emission across the emission area.

Emitting area
(15×15mil)

Au contact

SiO₂

p-r₁ junction

p-GaAs : Si

n-GaAs : Si

n-GaAs (substrate)

GaAs : Si
(LPE layer)
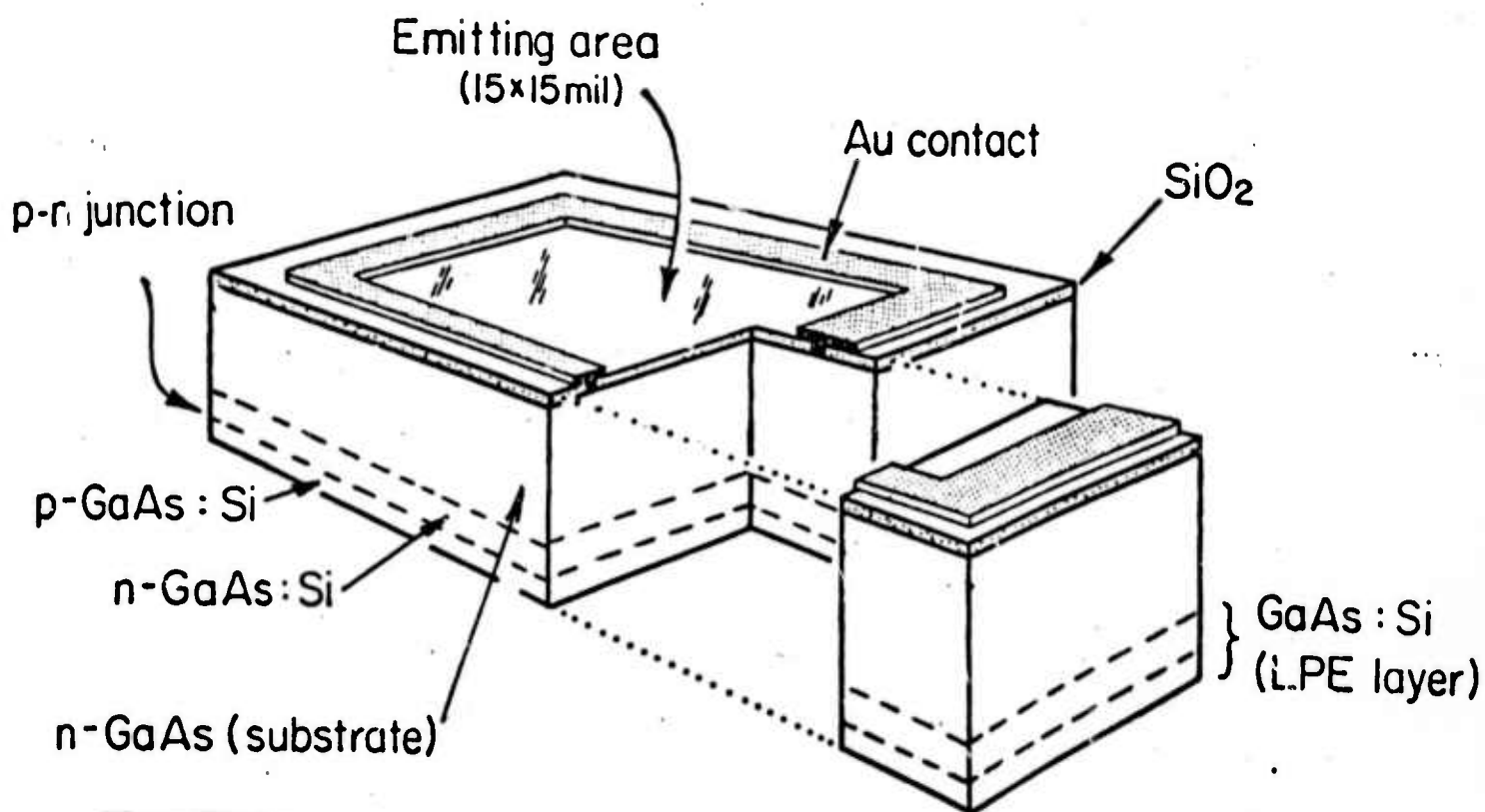
Fig. 3.1 Cutaway view of pump diode configuration for side pumping internal reflection mode minilaser.
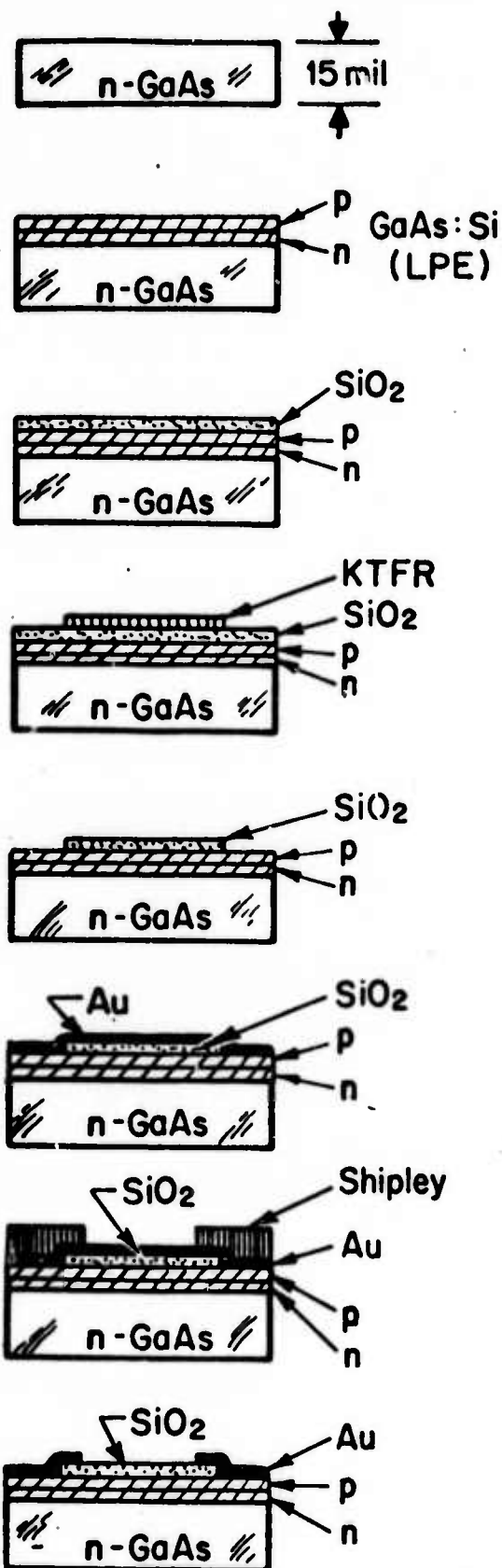
n-GaAs — 15 mil	Substrate n-GaAs
p GaAs:Si / n (LPE) on n-GaAs	Diode layers epitaxially grown
SiO₂ / p / n on n-GaAs	Deposited silicon dioxide mask 3500 Å
KTFR SiO₂ p n n-GaAs	KTFR Photoresist mask, spun-on and developed
SiO₂ p n n-GaAs	Silicon dioxide mask pattern etched and KTFR mask removed
Au SiO₂ p n n-GaAs	Gold (Au) vapor deposited over entire surface 3000 Å
SiO₂ Shipley Au p n n-GaAs	Shipley photoresist mask, spun-on and developed
SiO₂ Au p n n-GaAs	Gold contact etched and Shipley photoresist removed

Fig. 3.2 The sequence of steps in the fabrication of the original pump diode structure. The diode differs from the one shown in Fig. 3.1. In the latter the epi-layers are on the bottom.

a
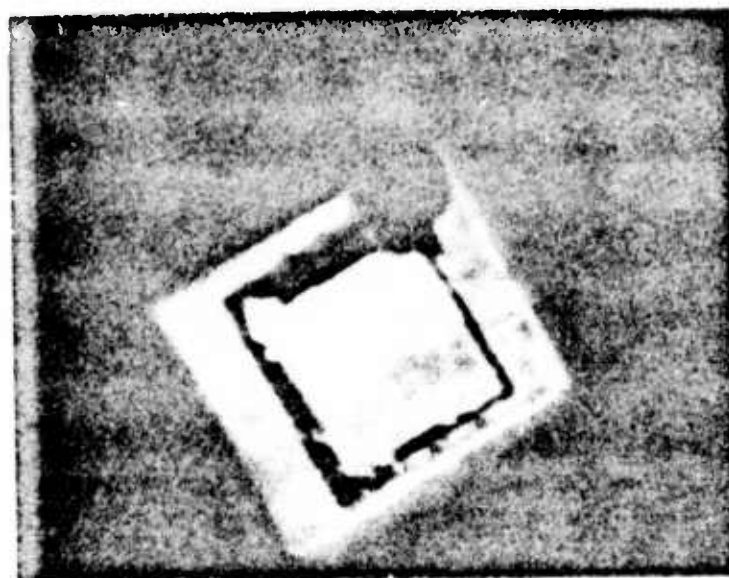
b

FIGURE 3.3. Photomicrographs of a device like that illustrated in Figure 3.1. a) Viewed through an ordinary microscope. b) Viewed through an infrared microscope. The contact in this particular device has been damaged by previous testing and is not typical.

which can become a matter of considerable concern at high current density. Another change is the use of plated Ni and plated Au for the p-side contact, and plated Au on the n-side. These contacts have been adopted from standard GaAs diode laser practice and are expected to reduce contact resistance, further reducing heating problems.

Development of fabrication procedures and the generation of the necessary mask sets for the new "inverted" pump diodes is continuing. The first such diodes should be ready shortly. In the meantime, testing of the initial type of devices has continued. The change in header from a TO-5 transistor header to a TO-39 coined eyelet header has helped the heating problem some; however, measurements at high current levels (> 100 A/cm^2) are still being made under pulsed conditions using the pulse amplifier described in the previous semi-annual report (see Figure 3.4). We find that the emission increases linearly with current density and we see no saturation of the emission even well above 500 A/cm^2. This indicates that we will be able to maintain efficiencies existing at low current up to the high current densities that will be necessary to reach the minilaser threshold.

The apparatus to measure the spatial profile of the emission has been used successfully and indicates a smooth profile with a broad forward directed peak. From these measurements it was learned that the assumption of uniform emission over the hemisphere made in the previous semi-annual report to calculate external efficiency from a measurement of the emitted power density at a distance directly in front of a diode over-estimated the efficiency. A more appropriate approximation would be to take the average over the hemisphere to be on the order of 50% of the density measured in this way. Consequently, an efficiency of 2% rather than 4%, as previously deduced, is found.

To check the efficiency measurement by a more direct technique, a calibrated
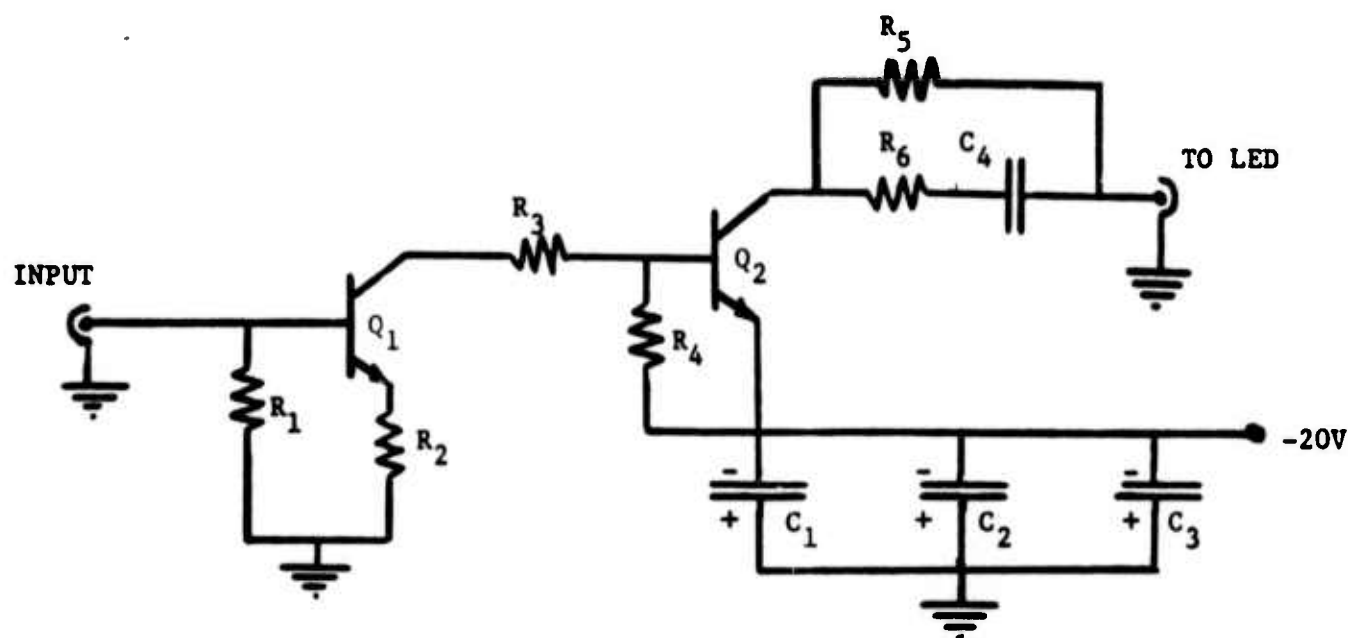
Component identification:

$R_{1,2}$	47 Ω, 1/2 W	C_1 0.1 µf, disc
R_3	100 Ω, 1/2 W	C_2 50 µf
R_4	390 Ω, 1/2 W	C_3 0.01 µf, paper
R_5	4.57 Ω, 2 W	C_4 0.0018 µf, disc
R_6	5.6 Ω, 1/2 W	
Q_1	2N5160 (Motorola)	
Q_2	2N4431 (TRW)	

FIGURE 3.4. Electrical schematic of the high current, fast rise-time pulse amplifier used to test diodes at high current densities.

integrating sphere which fortuitously became available to us, was used. With this instrument, a quantum efficiency of ≈ 1.5 % was measured on a device with all but the center emitting area masked. This value is consistent with the power efficiency figure deduced from the power density and spatial profile data.

Recalling the initial feasibility arguments made for the diode pumped minilasers, it was assumed there that an overall power efficiency of 2.5% could be achieved, and it would appear that we are slightly short of this goal. The difference is that the measurements have been made on unencapsulated diodes emitting into air while the calculations were made for diodes pumping a laser rod with n ≈ 1.5. The critical angle doubles with this change of n and four times the amount of light can escape from the diode surface. The external pumping efficiency would similarly quadruple.

Measurements of external efficiency with a dome made of a transparent material with n = 1.5 would, of course, be extremely desirable but this is experimentally difficult and we have not devoted any effort to making such measurements. We feel confident that diodes having an external pump quantum efficiency of 1.5% in air will have an efficiency of at least 5% pumping into the higher index laser rods.

The lasing threshold of the minilaser rods have been estimated to be 7.5 w/cm^2 of Si:GaAs diode pump radiation. If we assume an external quantum efficiency of 2% (again being conservative), then a current of 300 A/cm^2 will yield the necessary power density of ≈ 7.5 w/cm^2. The successful operation of a diode pumped minilaser appears well within our grasp, and we expect to achieve the goal in the near future.

3.3 Silicon-Doped Gallium Arsenide

The optimum silicon doping level in gallium arsenide has previously been determined to be 1.4 atomic percent Si in the melt. Layers of this composition are being grown regularly for use in fabricating pump diodes. (See the previous section). During these growths minor improvements are made in the growth procedures but the growth is largely routine. For a description of the growth philosophy and illustrations of the growth system and technique the reader is referred to prior semi-annual technical reports and proposals. A curve of the emission spectrum of a GaAs:Si diode grown from a melt containing 1.4 atomic percent Si is given in Figure 3.5.

3.4 Gallium Arsenide Antimonide

The study of $GaAs_{1-x}Sb_x$ as an alternative to GaAs the pump diode material has of necessity been largely concerned with characterization of the growth system and of the diode emission spectra. An important feature of this study has been the continued use of silicon as the dopant. Silicon is an amphoteric dopant so the p-n junction can be grown in a _single_ LPE step and it introduces relatively deep acceptor levels so longer wavelength emission is obtained from lower antimony fraction alloys.

Our measurements of the n-to-p transition temperature for silicon concentrations in the melt ranging from 0.1 atomic percent to 1.4 atomic percent and the x, in $GaAs_{1-x}Sb_x$, equal to 0.03 and 0.06, are shown in Figure 3.6. Similar results have been reported in earlier technical reports except that higher antimony series was listed as having x = 0.07. The value of 0.06 has been determined from electron microprobe and x-ray diffraction measurements made on grown layers. The measurements of emission spectra characteristics reported previously have also been corrected for this, and additional data has
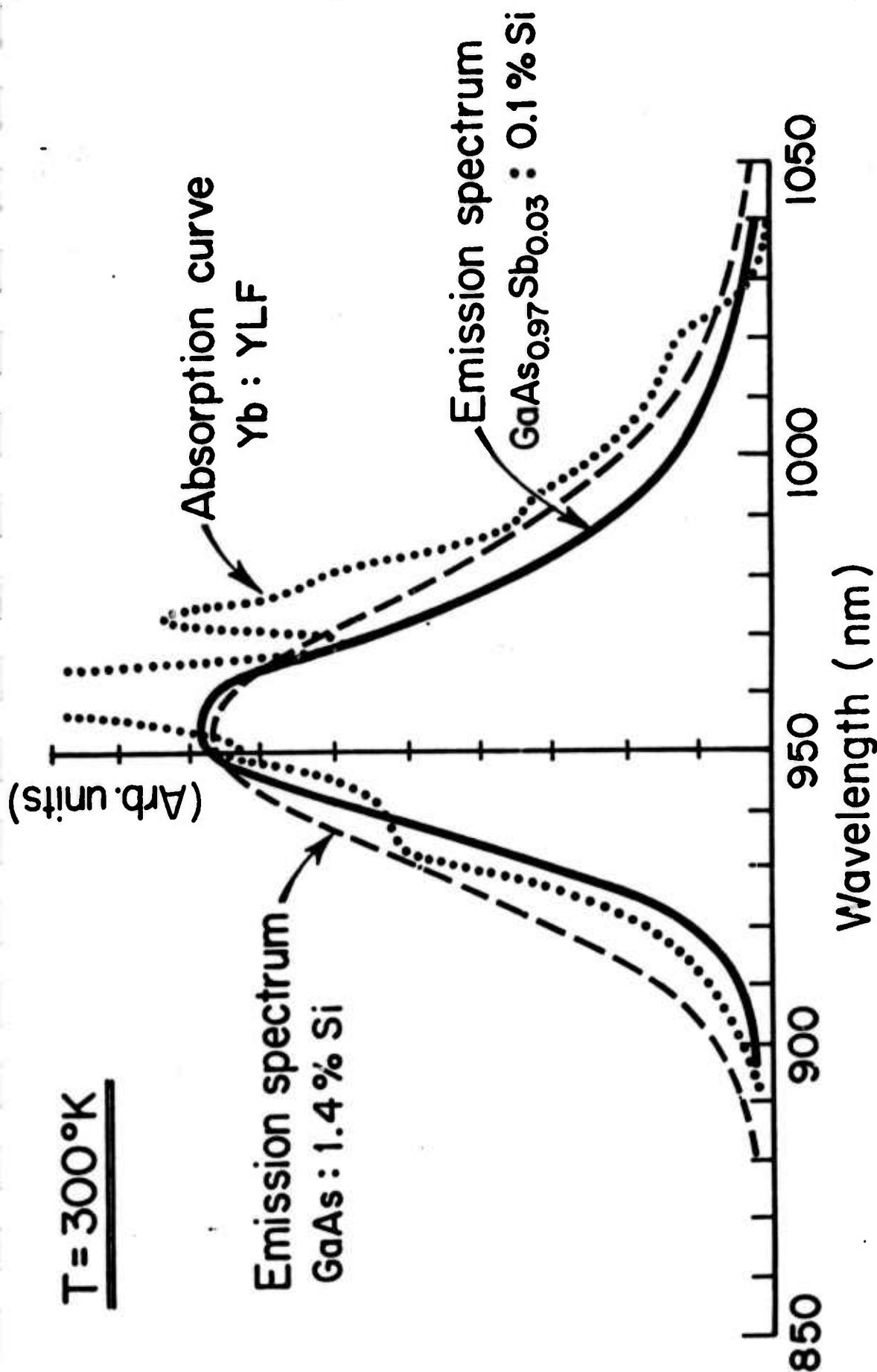
Fig. 3.5 A comparison of the Yb absorption spectrum with the emission spectra of GaAs:Si and Ga(As,Sb):Si LED's grown in this program. The emission curves have been adjusted to have the same peak value; the absorption spectrum curve is absorption coefficient, arbitrary units.
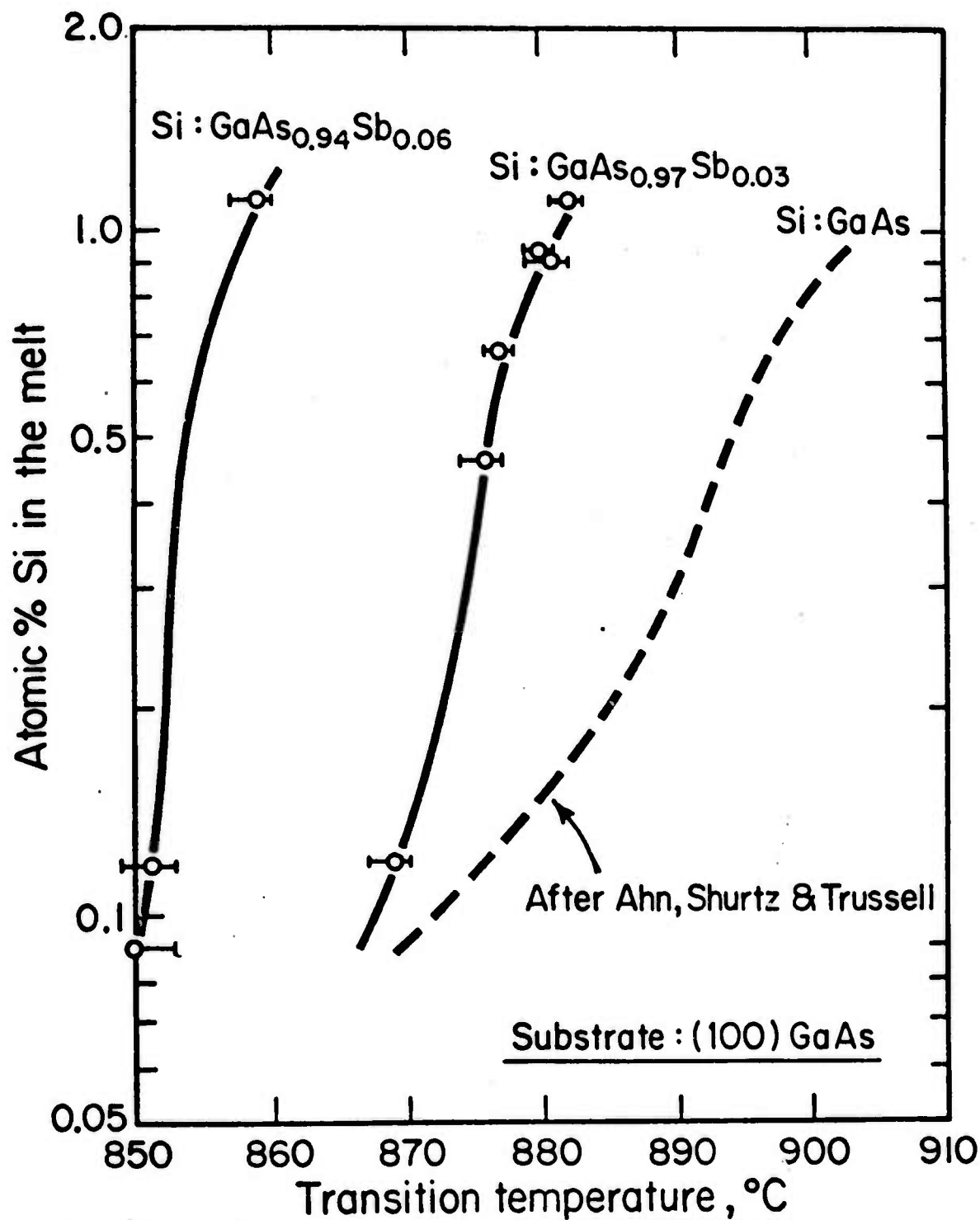
Fig. 3.6 The n- to p-type transition temperature for the amphoteric dopant Si in $GaAs_{1-x}Sb_x$, x = 0.0, 0.03, 0.06, as a function of Si concentration in the melt.

been added: the emission linewidth as a function of peak wavelength is shown in Figure 3.7 and the emission linewidth as a function of atomic percent silicon in the melt is shown in Figure 3.8.

The electron microprobe measurements mentioned above were made on angle lapped sample with the primary objective of determining the uniformity of the layers with regard to Sb fraction. It had been anticipated that the composition would be graded near the substrate but in fact the layers appeared to be very uniform, right to the substrate.

X-ray diffractometer measurements of lattice constants were made on several $GaAs_{1-x}Sb_x$ layers. The values determined were $a = 5.652$ Å, 5.665 Å, and 5.678 Å, for $x = 0.00$, 0.03, and 0.06 respectively. The lattice mismatch indicated is thus 0.23% for the $x = 0.03$ layers and 0.46% for $x = 0.06$.

Relatively crude efficiency measurements made on the $GaAs_{1-x}Sb_x$ LED's indicated that the $x = 0.03$ devices were about 1/3 as efficient (or $\sim 0.5\%$) as the GaAs LEDs , and the $x = 0.06$ devices were of the same order though definitely less efficient. This is an area where more work clearly must be done.

The original argument for going to a ternary pump diode, $GaAs_{1-x}Sb_x$ in our case, was that a lower Si concentration could be used and a narrower emission obtained. The justification for this is found in Figure 3.5 which compares the emission spectrum of a GaAs:Si diode and a $GaAs_{1-x}Sb_x$:Si diode both peaking at the pump band maximum, which is also shown. The $GaAs_{1-x}Sb_x$ diode, $x = 0.03$, was doped with 0.1 atomic percent Si in the melt and has a 25% narrower emission line that the GaAs:Si diode which was grown from a melt containing 1.4 atomic percent Si. In Figure 3.8 the emission curves are drawn with the same maximum height; the gallium arsenide antimonide diodes are in fact less efficient as was mentioned earlier. The GaAs diodes are therefore still the
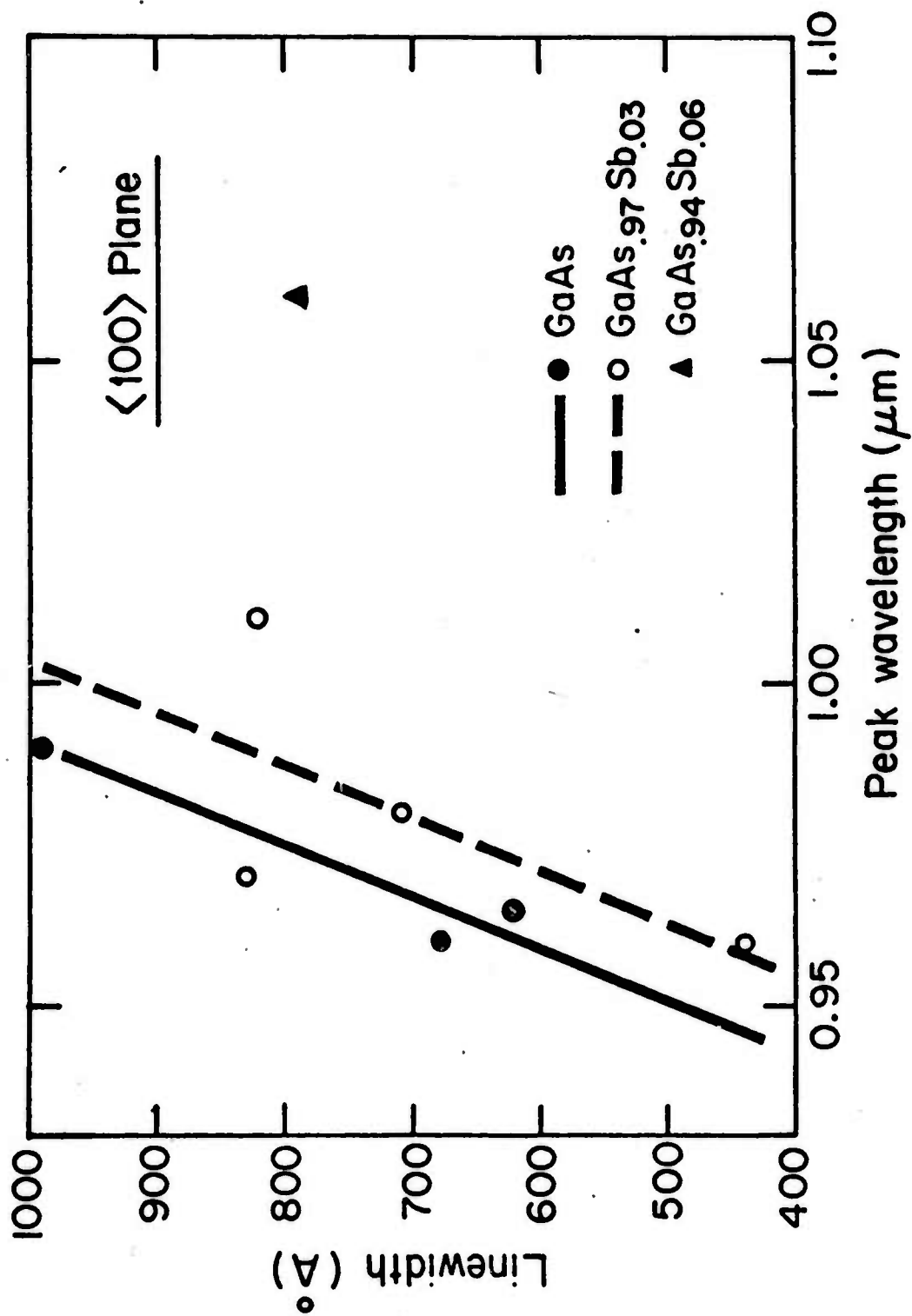
Fig. 3.7 Emission linewidth (half width) as a function of peak wavelength.
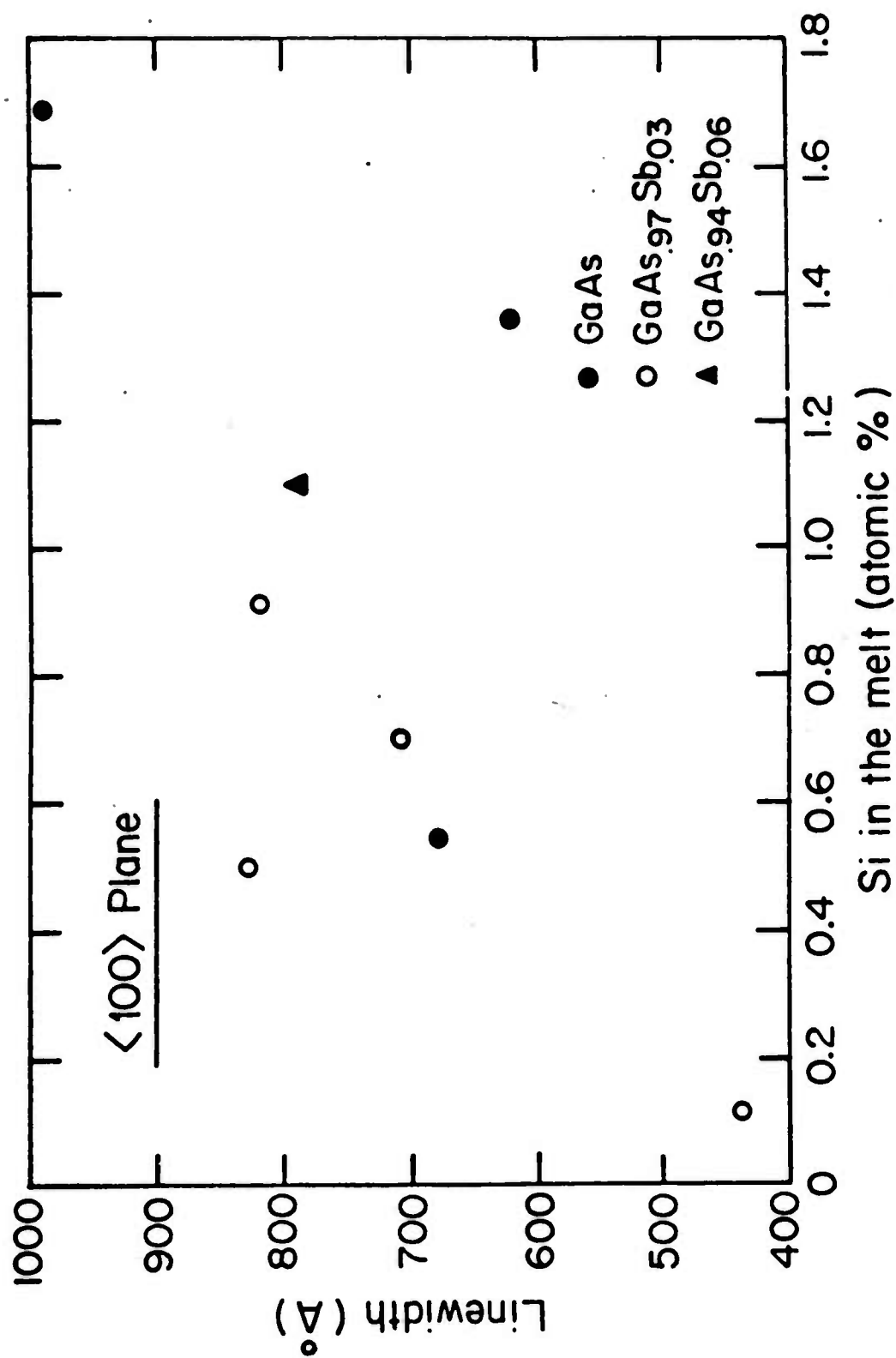
Fig. 3.8   Emission linewidth as a function of atomic percent
Si in melt.

best in overall pumping efficiency but as we improve the efficiency of the $GaAs_{1-x}Sb_x$ LEDs they will be superior.

Another significant result of our investigations of $GaAs_{1-x}Sb_x$ has been the demonstration of 1.06 µm emission with a full width at half maximum of 0.079 µm from $x = 0.06$ LEDs grown from a 1.1 atomic percent Si melt. A spectrum of such a diode superimposed on the low-loss fiber absorption curve is shown in Figure 3.9. Fiber loss at 1.06 µm is about half what it is in the 0.8 to 0.9 µm band and pulse dispersion for LED sources is approximately 25% of what it is at 0.9 µm. Thus the 1.06 µm band is a very important one for fiber communications and it becomes highly desirable to develop, for this wavelength, an efficient LED that can be fabricated in a simple way. In our process only a single epitaxy step is involved thereby eliminating the need for lattice matching layers or grading.

The growth of a simple 1.06 µm LED in $GaAs_{1-x}Sb_x$ should only be the beginning of the gallium arsenide antimonide story. For high brightness sources, low threshold diode lasers, fast detectors, and utlimately integrated optical circuits, heterostructure confinement geometry devices will be required and here we find that $GaAs_{1-x}Sb_x$ is superior to the present composition, $In_yGa_{1-y}As$, because it has a readily accessible lattice matching quaternary, aluminum gallium arsenide antimonide $(Al_yGa_{1-y}As_{1-x}Sb_x)$.

The study of $Al_yGa_{1-y}As_{1-x}Sb_x$ will form the basis for a separate research program but paper studies of it have been made in this program. Three advantages of it are immediately found: (1) the insensitivity of the lattice constant to the Al fraction, similar to the situation in $Al_yGa_{1-y}As/GaAs$, (2) the ease with which Al can be introduced into the grown epi-layers from a melt that is changed minimally from the melts used to grow $GaAs_{1-x}Sb_x$, and
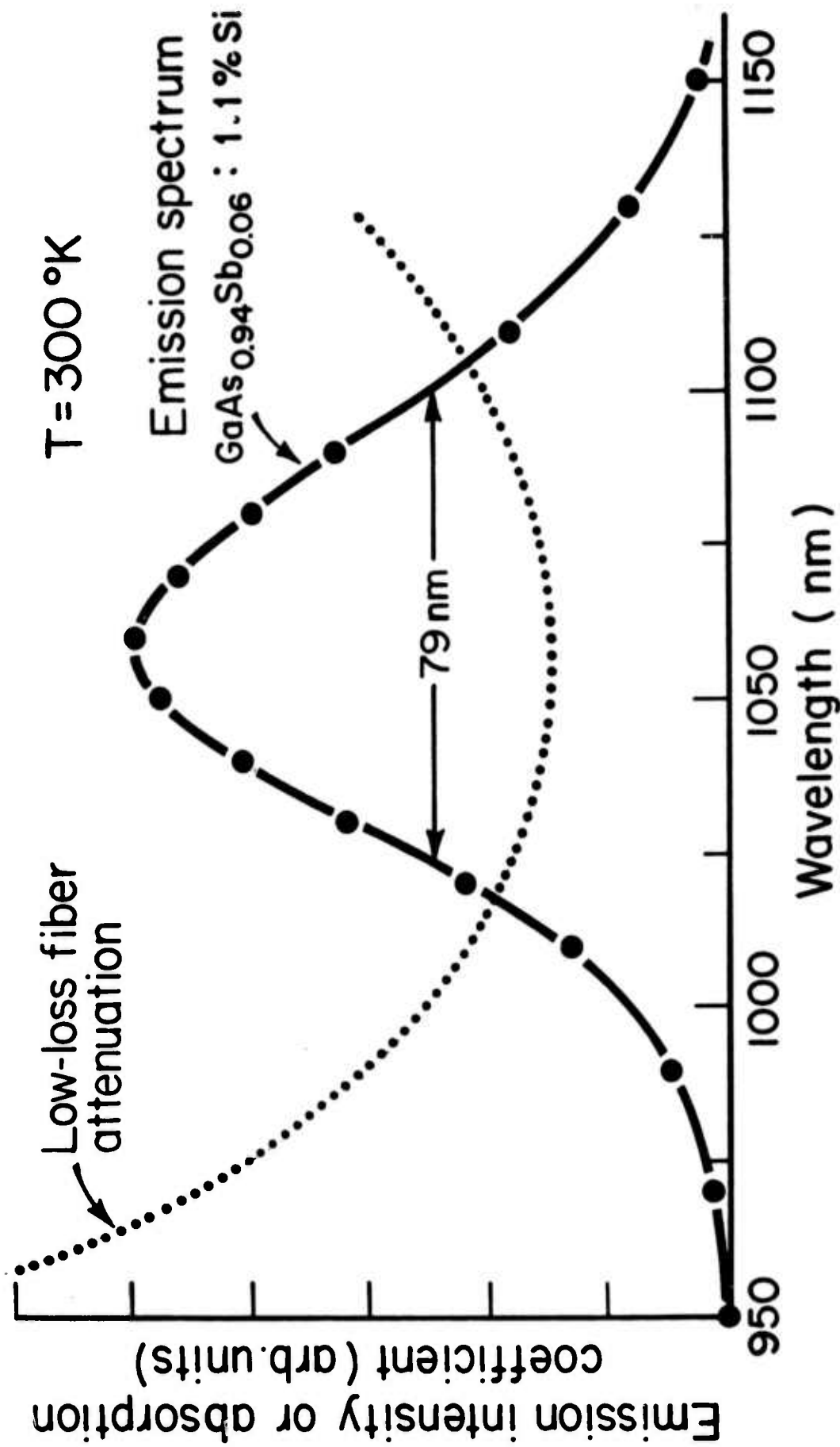
Fig. 3.9 Emission spectrum of $GaAs_{0.94}Sb_{0.06}$:Si diode compared with attenuation curve for low loss glass fiber.

(3) the increase of the band-gap with increasing Al fraction. The first and third points can be understood readily from Figure 3.10 in which the lattice constants, a,[*] and energy gaps, E_g, of the two quaternaries (Al,Ga)(As,Sb) and (In,Ga)(As,P) are plotted and compared. The point is that in $In_yGa_{1-y}As_{1-x}P_x$, both x and y must be varied to vary E_g while maintaining a constant "a", while in $Al_yGa_{1-y}As_{1-x}Sb_x$, x can be held constant while E_g is varied by varying y; "a" is relatively insensitive to y.

The second point of the three comes from the fact that a very small fraction of Al in the Ga-rich LPE melt leads to a large fraction of Al in the grown layers. For example to grow a layer containing y = 0.10, a melt containing only 0.1 atomic percent Al need be used. This small fraction of Al will not disturb the melt solubilities and the same composition melts that are used to grow $GaAs_{1-x}Sb_x$ can be used to grow $Al_yGa_{1-y}As_{1-x}Sb_x$, same x and y < 0.2, but just adding small amounts of Al. Because the exact y value is not critical, the poor control over y is unimportant.

The important advantages of the gallium arsenide antimonide/aluminum gallium arsenide antimonide system are clear and it is significant that our experience with gallium arsenide antimonide LPE can be directly transferred to the quaternary. We feel that these compounds will be very important in future semiconductor optical fiber and monolithic integrated optical circuits.

---

[*] Because Vegard's law is satisfied by these compounds the lattice constant varies linearly with alloy composition and thus composition can be obtained from this figure also.
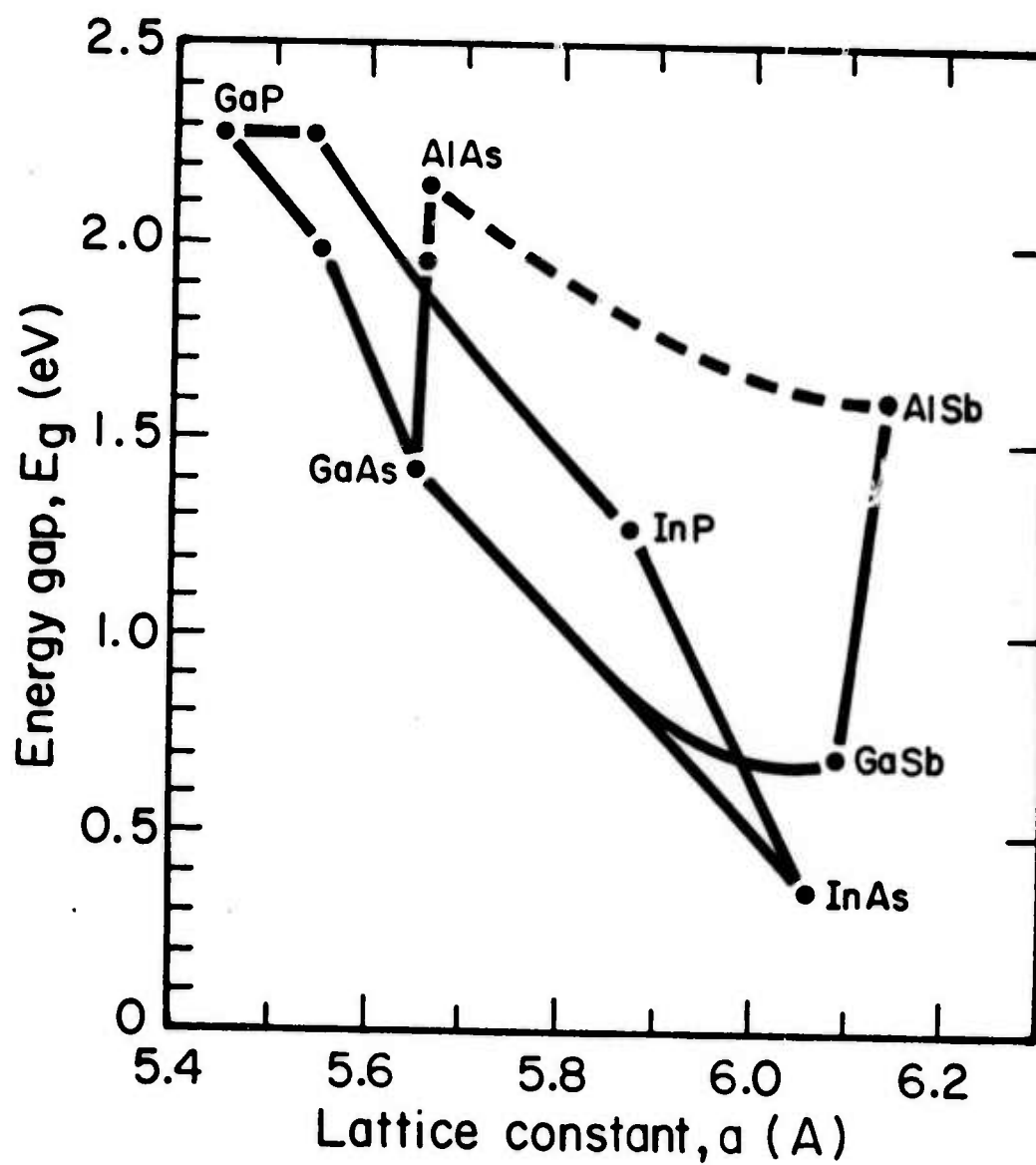
Fig. 3.10 Lattice constants and energy gaps for the quarternaries $In_yGa_{1-y}As_{1-x}P_x$ and $Al_yGa_{1-y}As_{1-x}Sb_x$.

IV. KTN THIN FILMS

4.1 Accomplishments

The major accomplishments in the KTN program have been:
1) the development of a liquid-phase-epitaxy dipping technique for the growth of single crystal KTN thin films; 2) the characterization of the dielectric and optical properties of these films; and 3) the fabrication and evaluation of a KTN thin film modulator. The motivation for our materials device program came first from the recognition that KTN, with chemical formula $K\,Ta_{1-x}Nb_xO_3$, possesses a large room temperature electrooptic effect for concentrations $0.25 < x < 0.35$, implying a low drive voltage for electrooptic device applications, and second from the assumption that the thin film growth technique would eliminate or reduce inhomogeneity problems encountered in the growth of bulk KTN.

4.2 Growth of Single Crystal Films

We patterned our LPE dipping process after the technique used for the growth of magnetic-bubble thin films. For the substrate we used the end member of the KTN system, $KTaO_3$, which has the lowest optical index of any KTN composition. Consequently, all non-zero Nb concentration films grown on this substrate should support guided modes. The $KTaO_3$ substrates were typically 1 mm thick and about 18 mm in diameter with faces perpendicular to (100) directions. Both surfaces are polished with diamond grit (3 μm, 1μm, 0.25 μm) and Syton to a flatness of 1/4 wavelength and a parallelism of 20 seconds of arc.

The starting melt was obtained from a mixture of K_2CO_3, Ta_2O_5, and Nb_2O_5 powders. Although this is a three component system, the use of the binary KTN phase diagram (Fig. 4.1) is useful for predicting the mole ratio of Nb:Ta

crystallized in the film.

The growth process is begun by lowering the temperature to the desired starting point and then dipping the substrate into the melt. A 15 mole % excess of potassium serves as a flux. The starting melt compositions used were $K_{1.15}Ta_{1-x}Nb_xO_3$ with x varying from 0.4 to 0.6. The crystallized films were of composition $K\ Ta_{1-x}Nb_xO_3$ with x ranging from 0.10 to 0.35. The growth temperatures in these runs varied from 1100°C-1140°C.

The actual temperature cycle is shown in Fig. 4.2. The important features in this cycle are, first, a long soak of 7 to 12 hours and, second, a temperature lowering of 1-2°C/hr. during the actual dip. Dip durations varied from 1-2 hrs. and axial rotation rates changed from 30-100 rpm with best results at about 60 rpm. After removing the sample from the melt, it was spun for 10 seconds at 1000 rpm to eliminate excess flux droplets from the film surface. One advantage of the growth technique is the ability to recycle the melt several times before replenishing the contents. Another advantage is the capability of growing different film compositions from the same starting melt components by varying only the growth temperature.

The "as grown" films were typically 10-20 microns thick with rippled surface features similar to those observed in the growth of $LiNbO_3$ and sillenite films. Such features must be polished before any guiding experiments can be performed. Initial films had a slight bluish tint indicating oxygen deficiencies. The addition of a small amount of SnO_2(0.04 mole %) to the melt eliminated this coloration, presumably by compensating for oxygen vacancies.
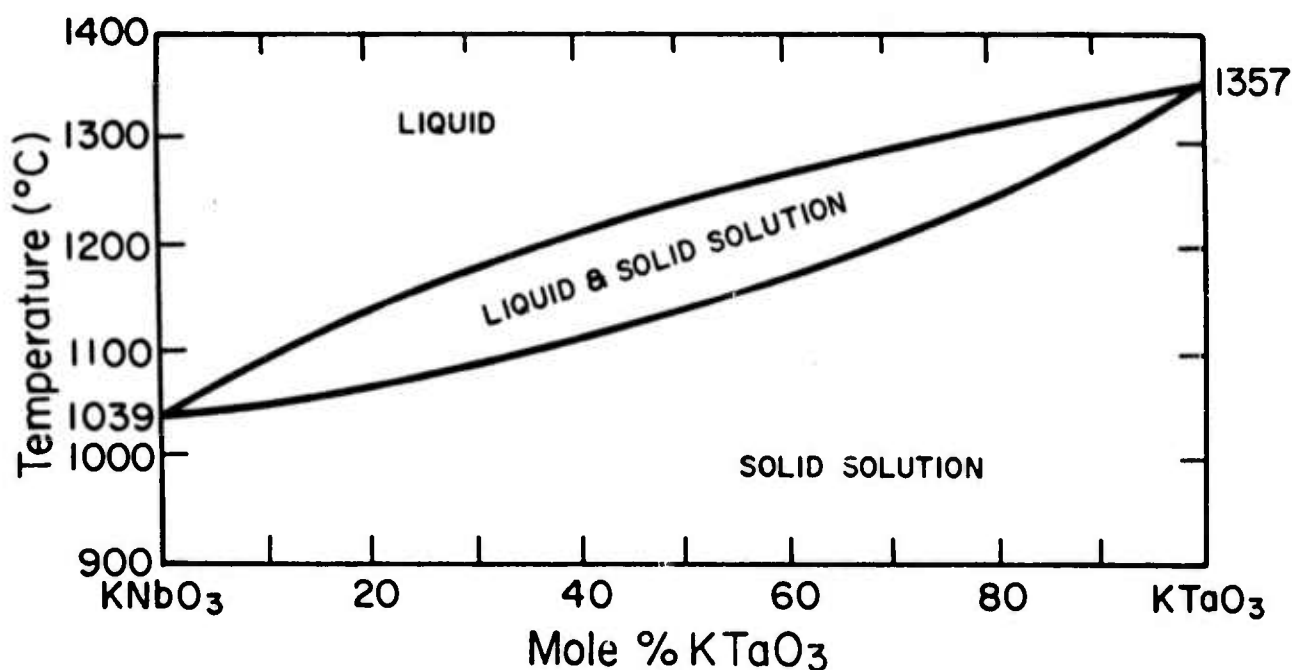
Fig. 4.1   Phase diagram for KTN

Recently a multi-layered dip was performed. An edge view of the
two films on a $KTaO_3$ substrate is shown in Fig. 4.3. The top film con-
tains 25 mole % Nb, the lower film is a 27 mole % Nb. This double dip
suggests the possibility of multi-layered device applications and points
out the flexibility inherent in the KTN system.

4.3 Film Characterization

Of principal concern in our work was whether the thin films would show
the compositional variations which have frustrated attempts to grow high qual-
ity bulk crystals. Microprobe analysis of lapped samples showed no detectable
Nb variation as a function of film depth. One such microprobe scan is shown
in Fig. 4.4. Within the experimental accuracy, the films are uniform in com-
position and the thin film-substrate interface is abrupt, implying a sharp
discontinuity in dielectric and optical properties.
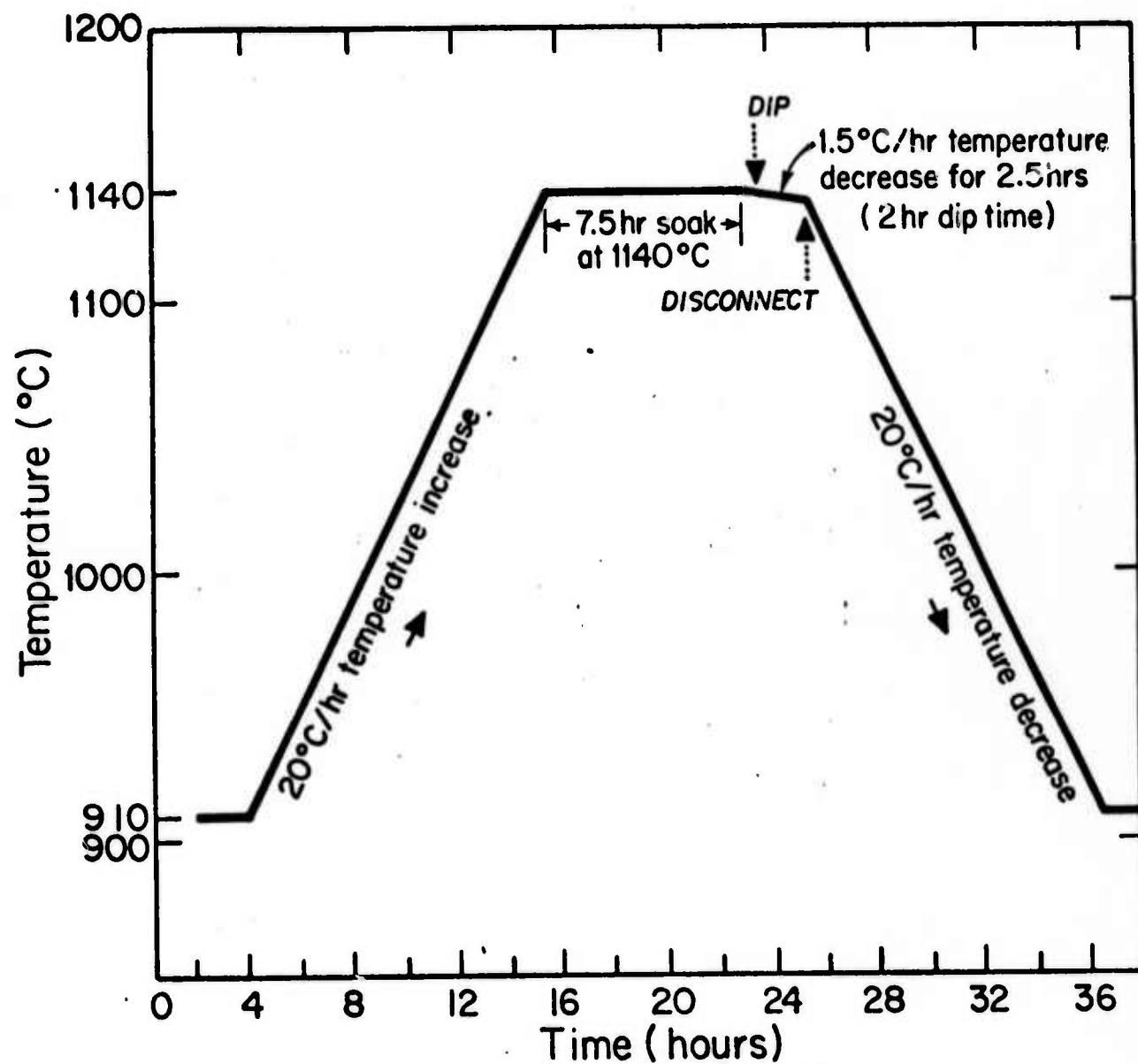
Fig. 4.2 Temperature cycle for LPE growth
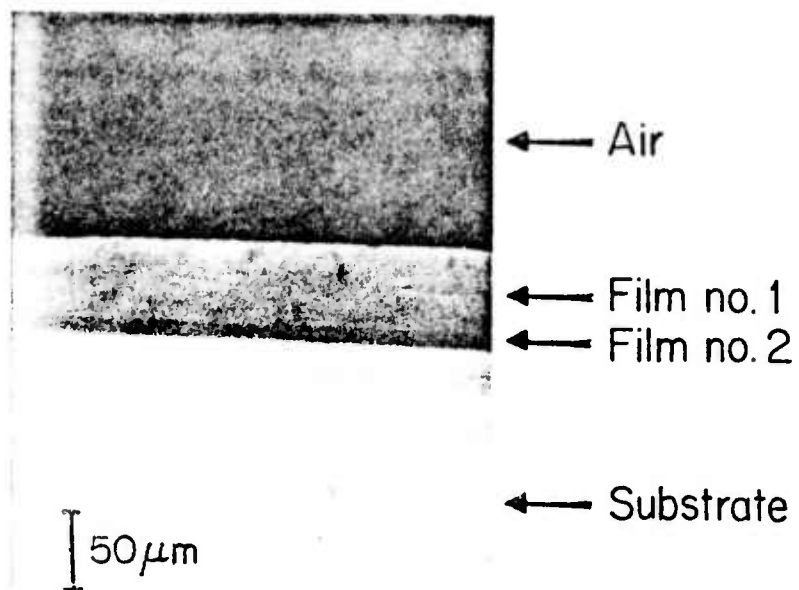
Fig. 4.3 Two epitaxial KTN films of different
composition grown on $KTaO_3$ substrate
by multiple dip process.
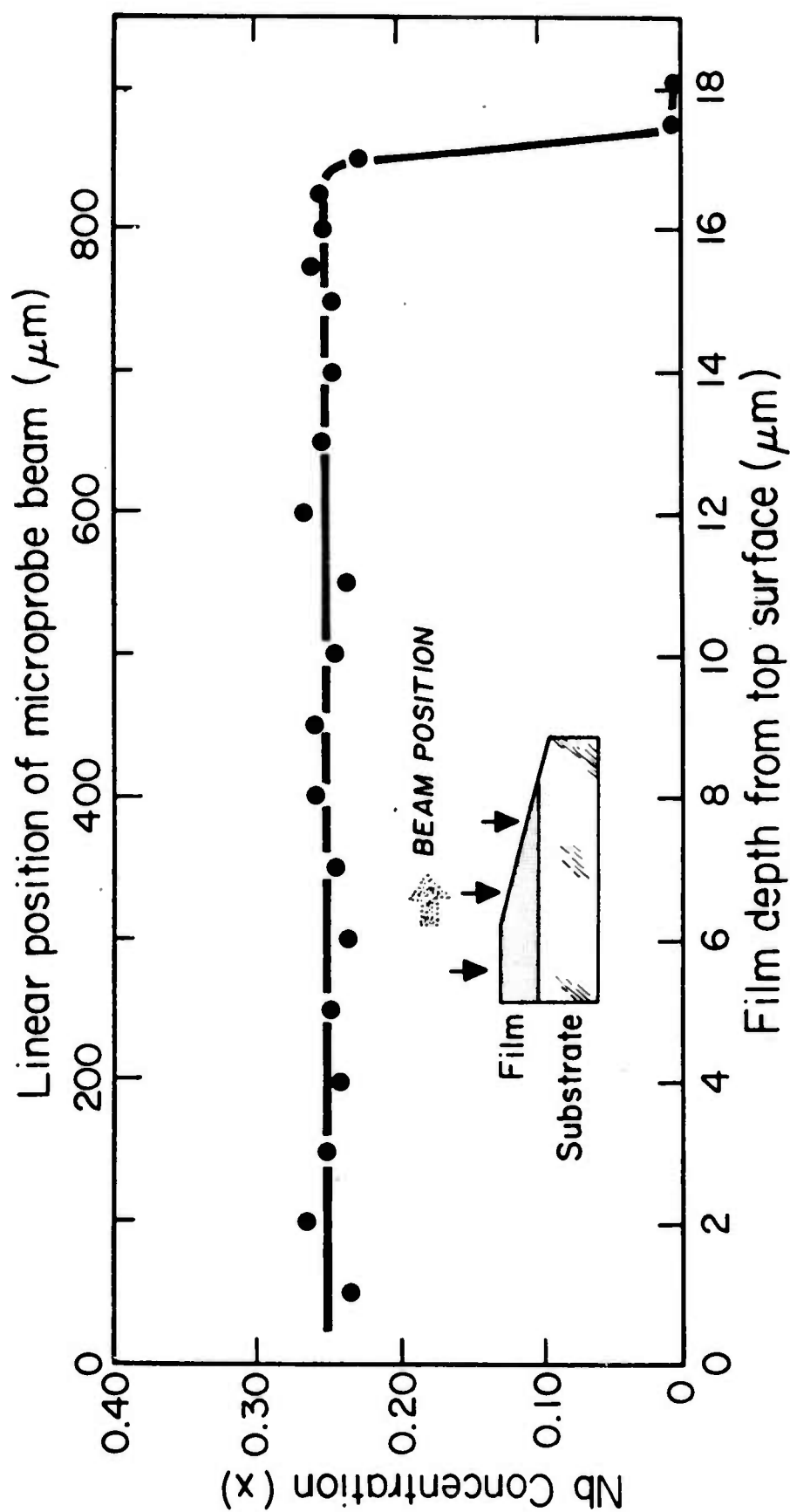
Fig. 4.4. KTN composition determined by microprobe analysis.

Film composition can also be determined from X-ray measurement of lattice constant. A typical diffraction pattern is shown in Fig. 4.5. The X-rays penetrate the film and, consequently, the resultant diffraction pattern shows a pair of (500) peaks -- produced by $K\alpha$, $K\alpha_2$ radiation from a Cu target -- for both film and substrate. From analysis of these data we find that the film has a lattice constant of 3.988 Å corresponding to the composition x = 0.34. The angular separation between the peaks for film and substrate gives an accurate measurement of lattice mismatch, which for the sample shown is 0.12%, the film having the larger lattice constant.

KTN is a ferroelectric perovskite and as the temperature is lowered undergoes the three phase transitions typical of the class: cubic to tetragonal to orthorhombic to rhombohedral. A measurement of capacitance as a function of temperature reflect these dielectric singularities accompanying each transition. Results are shown for a 26 mole % Nb film (composition determined from X-ray analysis) in Fig.4.6. Measurements of the ratio of imaginary to real part of the dielectric constant, $\varepsilon''/\varepsilon'$, were made using a capacitance bridge system available in the MIT Laboratory for Insulation Research. The loss tangent was unusually large, 0.1 to 0.2. Unless it can be reduced, dielectric losses at high frequency will be excessive and will lead to internal heating that can seriously degrade device performance.

Optical guiding experiments were performed using a rutile prism coupler. A photo showing 5 "m" lines formed by the ouput TE modes of a 35 mole % Nb film is shown in Fig. 4.7. From the synchronous angle measurements, the index difference between film and substrate was found to be 0.035. Large scattering in the film is apparent from the grainy nature of the "m" lines
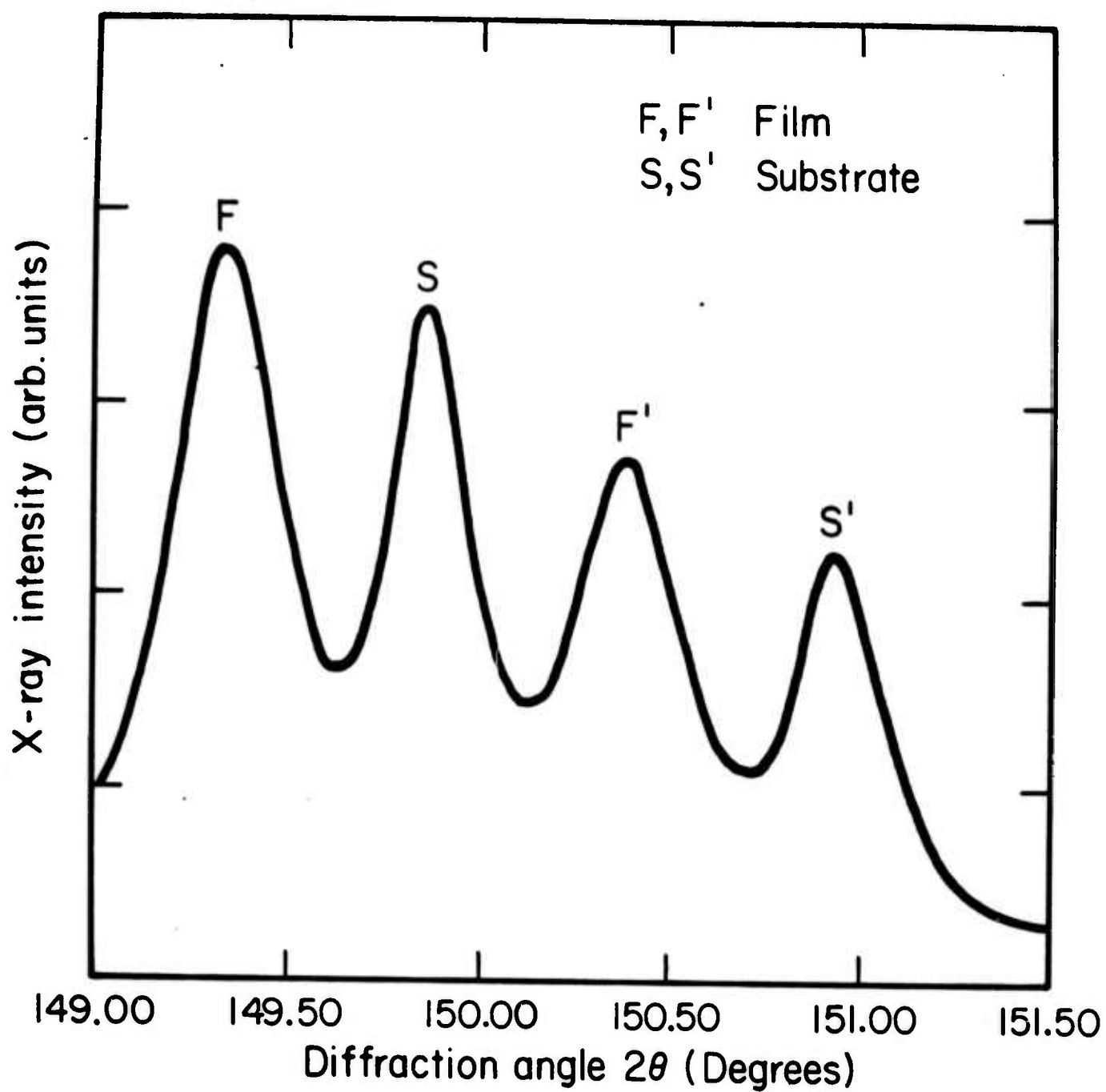
Fig. 4.5 X-ray diffraction peaks from film and
substrate.
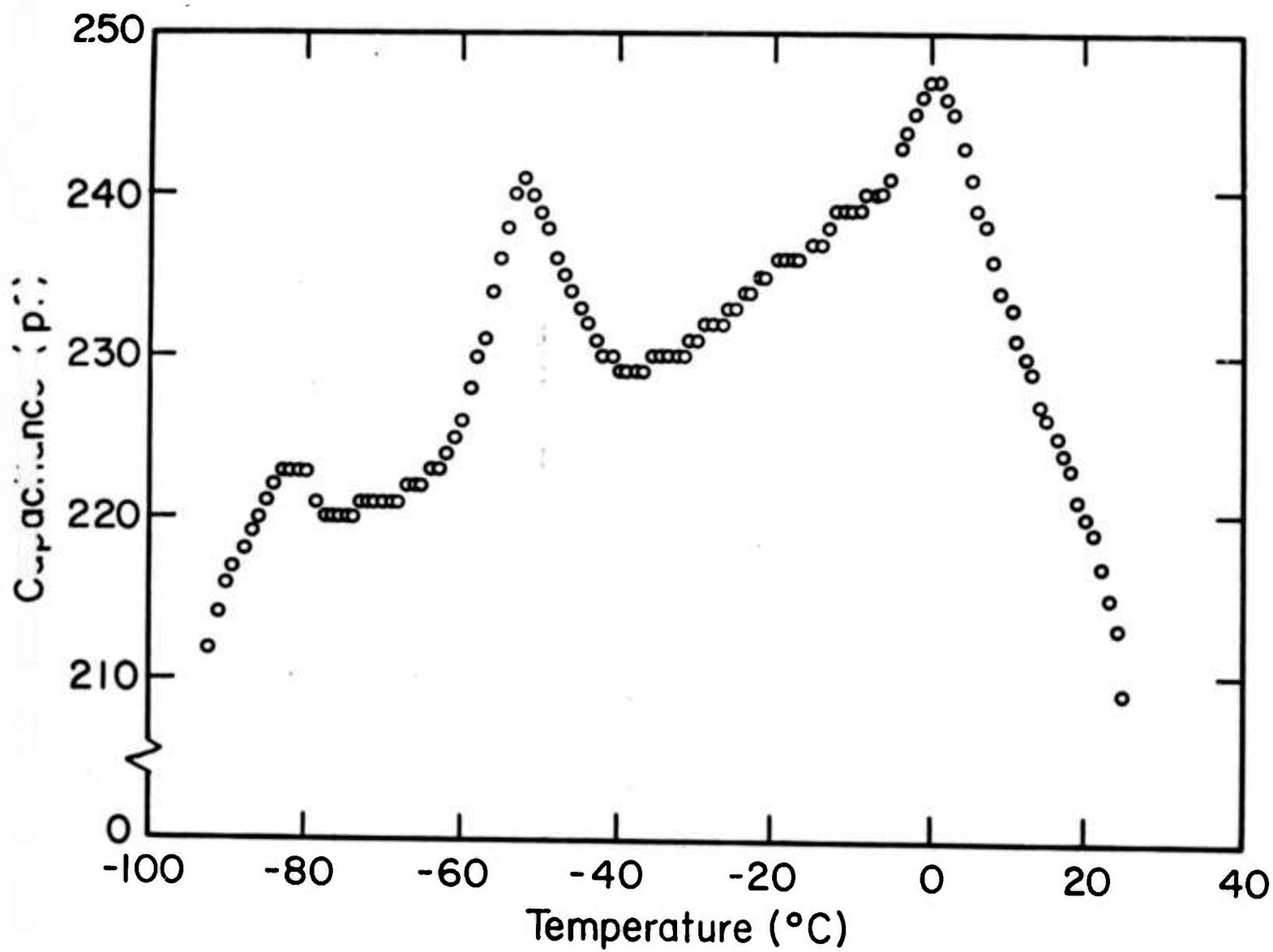
Fig. 4.6 Capacitance measurements for KTN
film, x = 0.26.
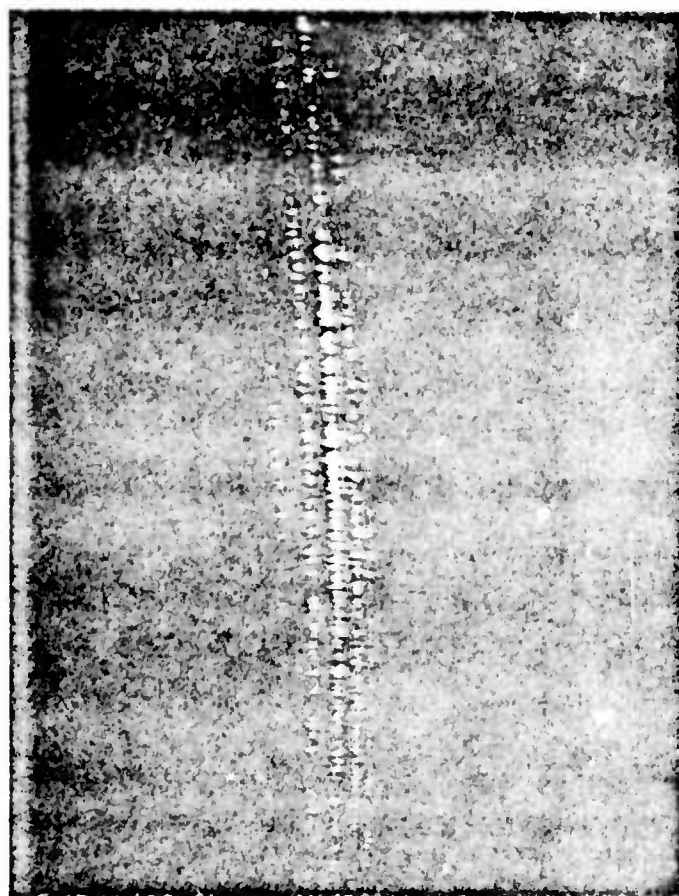
Fig. 4.7 The "m" lines observed at output prism.

plus the fact that, although only the TE_2 mode was excited at the input, all five modes occur at the output coupler. A plot of loss vs. wavelength is shown in Fig. 4.8. A $(1/\lambda)^4$ line is plotted as a reference slope for Rayleigh scattering. At 6328 Å, the loss is 8-12 db/cm depending on the mode excited. This value compares favorably with other single crystal thin films having comparable index differences.

4.4 Device Fabrication and Evaluation

A KTN thin film modulator was fabricated using the electrode geometry shown in Fig. 4.9. The interdigital electrodes had 18 fingers of length 3 mm, the finger width and spacing each being 25 microns. The electrode was fabricated by photolithographic techniques using Au-Ti metallization. When a voltage is applied across the electrodes, the guided mode experiences a periodic refractive index variation transverse to its propagation direction. After passage under the electrode system the emerging field has a spatially periodic phase front. The result is an output radiation pattern in which energy is scattered from the central beam into a series of side lobes. The output intensity of the central, i.e. undiffracted, beam is determined by the maximum phase change that the beam undergoes in traversing the electrode structure. For Raman-Nath diffraction, the output intensity goes as

$$I_0 \propto J_0^2 \, (\Delta\phi) \tag{4.1}$$

where J_0 is the zero order Bessel function and $\Delta\phi$ is the phase shift, while for Bragg deflection

$$I_0 \propto \cos^2(\Delta\phi/2) \tag{4.2}$$
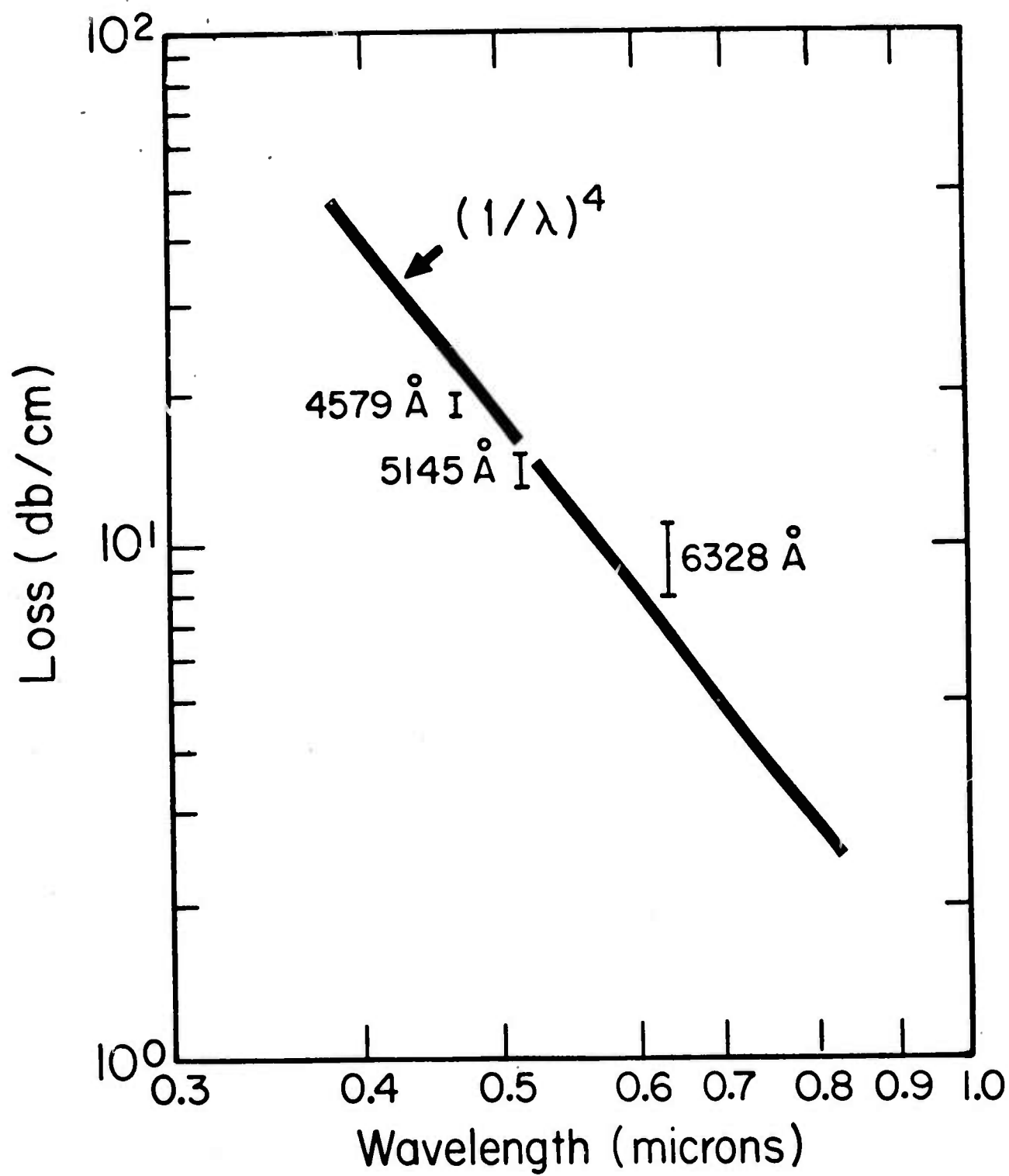
Fig. 4.8 Attenuation in KTN thin film.
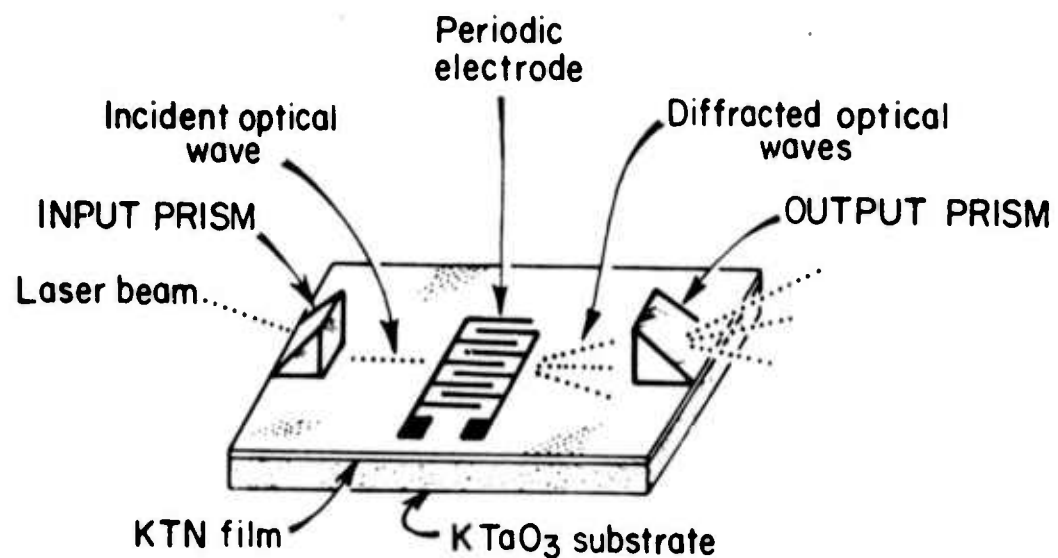
Experimental Arrangement For Evaluation of KTN Modulator

Fig. 4.9

For KTN which has a quadratic electrooptic coefficient g, dielectric constant ε, and optical index n_0, the phase change is

$$\Delta\phi = \pi g \; \varepsilon^2 E^2 n_0{}^3 \; W/\lambda_0 \qquad (4.3)$$

where W is the electrode distance traversed. For our electrode geometry, the diffraction regime is more nearly Raman-Nath than Bragg. According to the former theory, the central beam intensity should be zero when $\Delta\phi = 2.3$. For a 26 mole % Nb film with $n_0 = 2.24$, $\varepsilon = 2000 \; \varepsilon_0$, $g = g_{11} = 0.134 \; m^4/c^2$, this implies maximum intensity modulation for E = 5800 V/cm or, with fingers spaced by 25 microns, an applied voltage of $\sim$ 14 volts. Fig. 4.10 shows a plot of central beam intensity vs. voltage for a 26 mole % Nb thin film modulator. Minimum central beam intensity occurs at 15 volts in agreement with theory. Fig. 4.11 shows the low frequency behavior of the modulator. Note that because we are using the quadratic electrooptic effect the output signal varies as the square of the input.

The frequency operation of the modulator was limited to values less than 100 kHz, due most likely to excessive joule heating caused by the large dielectric loss tangent in the material. In KTN, the dielectric constant goes as

$$\varepsilon \; \alpha \; \frac{A}{T - T_0} \qquad (4.4)$$

where T_0 is the Curie Temperature. Referring to Eq. 4.3, we see that any increase in operating temperature reduces electrooptic performance. A minimum rise time of 3 μs has been observed in the central beam light intensity when pulsed modulation voltages are used.
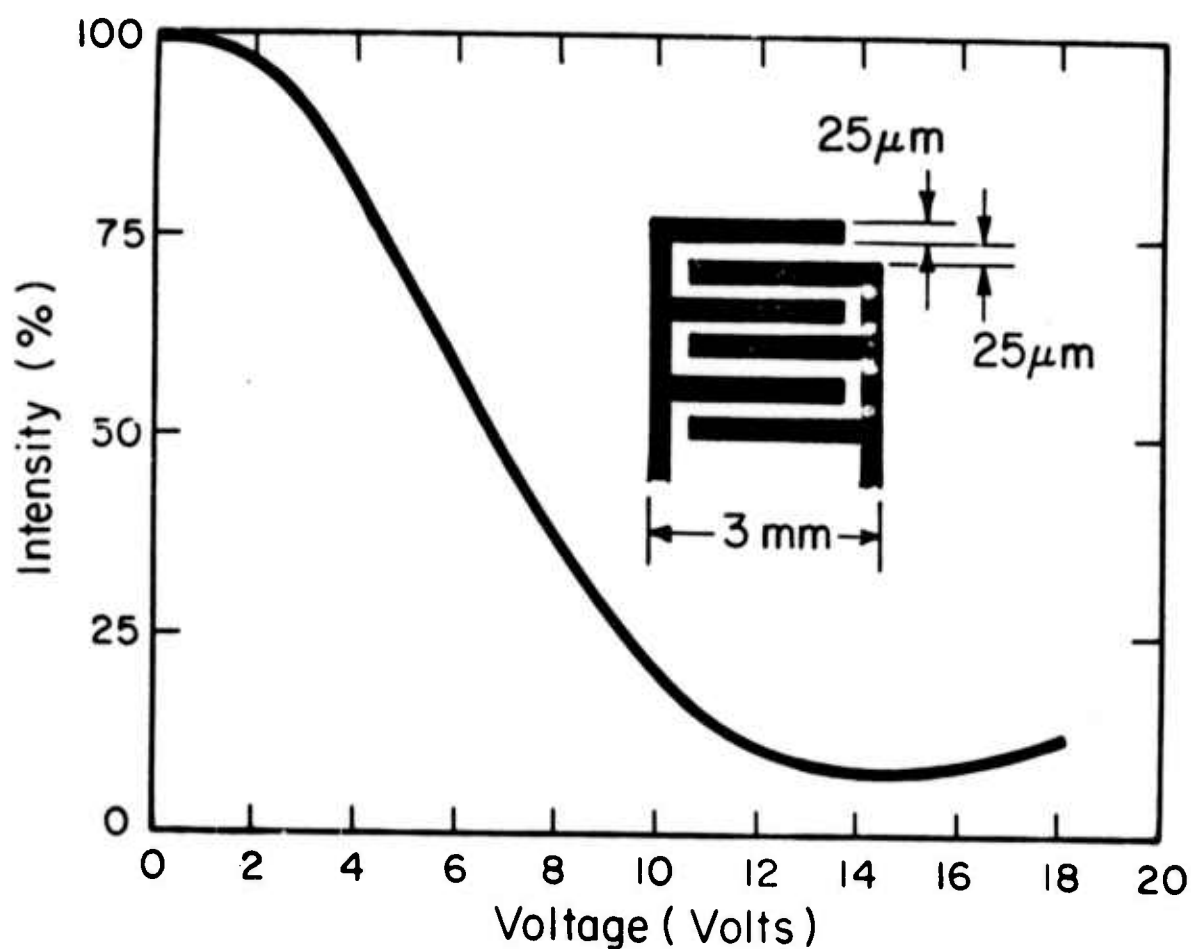
Intensity of Central Beam As A Function
of Voltage Applied To Modulator

Fig. 4.10

MODULATION   VOLTAGE =   16 V. (p-p)
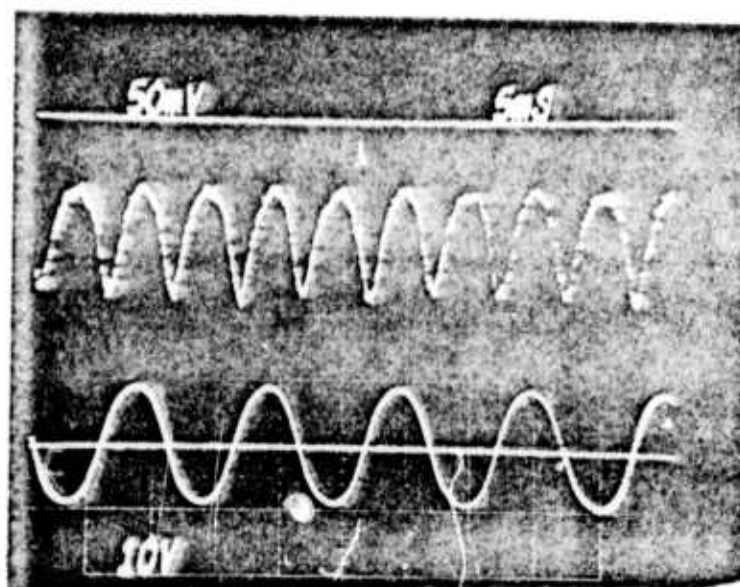
central beam
intensity

modulating
voltage

MODULATION   VOLTAGE =   32 V.(p-p)

central beam
intensity

modulating
voltage

Fig. 4.11 Low frequency performance of
electrooptical modulator.

4.5 Growth of KTN by Chemical Vapor Deposition

Early in the contract period we had hopes of growing KTN thin films by the chemical vapor deposition method (CVD) for use as optical wave guides. As the system grew and became more complex, it became obvious that a greater effort than originally assumed would be involved. Consequently, we started a second parallel effort to produce KTN thin films by liquid phase epitaxy (LPE) and this ultimately proved successful. The CVD technique however, still seems promising both for KTN thin films and similar double oxide systems. The apparatus which was developed under this contract evolved from a single zone furnace to a double zone furnace with a closely controlled thermal profile and an elaborate control system.

A CVD system for the growth of KTN in bulk and thin film form was first constructed. The system, shown in Fig. 4.12 had provision for six independent gas flows. Two chlorine flows were used for the production of $TaCl_5$ and $NbCl_5$ vapor by the controlled chlorination of Ta and Nb metal. Monitored flows were provided for the oxygen and hydrogen necessary for the reaction

$$2KCl + 2(1-x)TaCl_5 + (2x)NbCl_5 + 6H_2 + 3O_2 \rightarrow 2KTa_{1-x}Nb_xO_3 + 12HCl$$
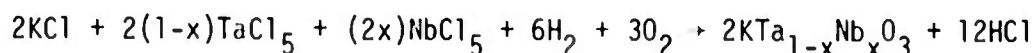
A third chlorine flow was used to create, between the chloride streams and the H_2 and O_2 flows, a sheath which prevented the reaction from occurring at the nozzle, where it could cause clogging, and allowed the reaction instead to occur downstream in the reaction zone. Finally, helium was introduced to suppress back-diffusion of the metal vapors, and to allow for purging the system during start-up and termination of the run.

The production of the TaCl and NbCl vapors was accomplished without difficulty. The Ta and Nb were chlorinated in external reactors heated to 240°C
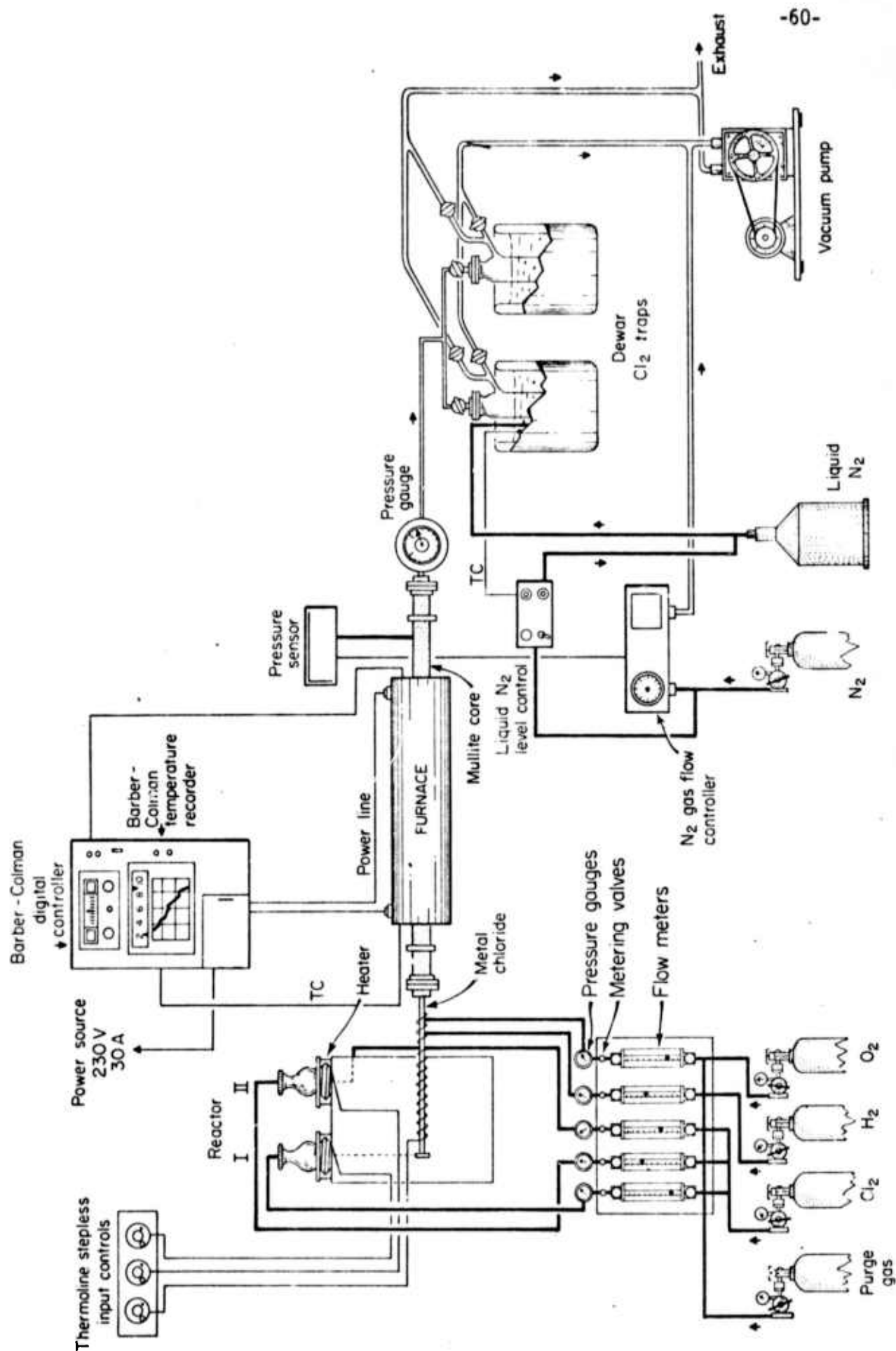
Fig. 4.12 CHEMICAL VAPOR DEPOSITION SYSTEM

and the vapors transported to the furnace in heated lines. The production
of KCl vapor proved much more difficult. After a number of false starts we
ended up with an arrangement in which liquid KCl was vaporized inside a
Knudsen cell.(Fig.4.13). The cell was a cylindrical quartz vessel 3"in length
and 1" in diameter, with a 0.25 mm diameter hole at the exit end. To obtain a con-
trolled flow the cell was positioned in the furnace at a point where the temp-
erature was slightly above the melting point of KCl (ca. 770°C). Unfortunately,
in the single zone furnace there was a substantial gradient at the point where
we had to position the Knudsen cell.

Work at this point was concerned with finding the appropriate con-
ditions for KTN growth. Nineteen runs, lasting from 1 to 8 hours, were made.
Runs 1 through 8 involved general testing of the system as well as checks on
$TaCl_5$ and $NbCl_5$ production and flow. Runs 9 through 14 were concerned with
finding a suitable scheme for the production of a controlled flow of KCl vapor.
Runs 15 and 16 were tests to see whether the pentoxides of Ta and Nb could be
grown. Runs 17 through 19 were unsuccessful attempts to grow KTN. It appeared
that if we were to be successful in growing KTN by chemical vapor deposition,
we needed greater flexibility in control of KCl flow than we had in our furnace.
A two-zone furnace would provide this needed flexibility.

An existing two-zone furnace was modified and adapted to grow KTN. The
modifications included redesign and rebuilding of the external reactors to handle
the Ta and Nb. Necessary improvements in the gas distribution system and pumping
system and replacement of parts were carried out. The work underway at that
point was concerned with modifying the existing temperature profile to create
a nearly flat thermal profile at $\sim$ 950°C over the 4" length of the Knudsen cell.
(Fig. 4.14).

The new furnace consisted of eight globars which ran the length of a 48 mm
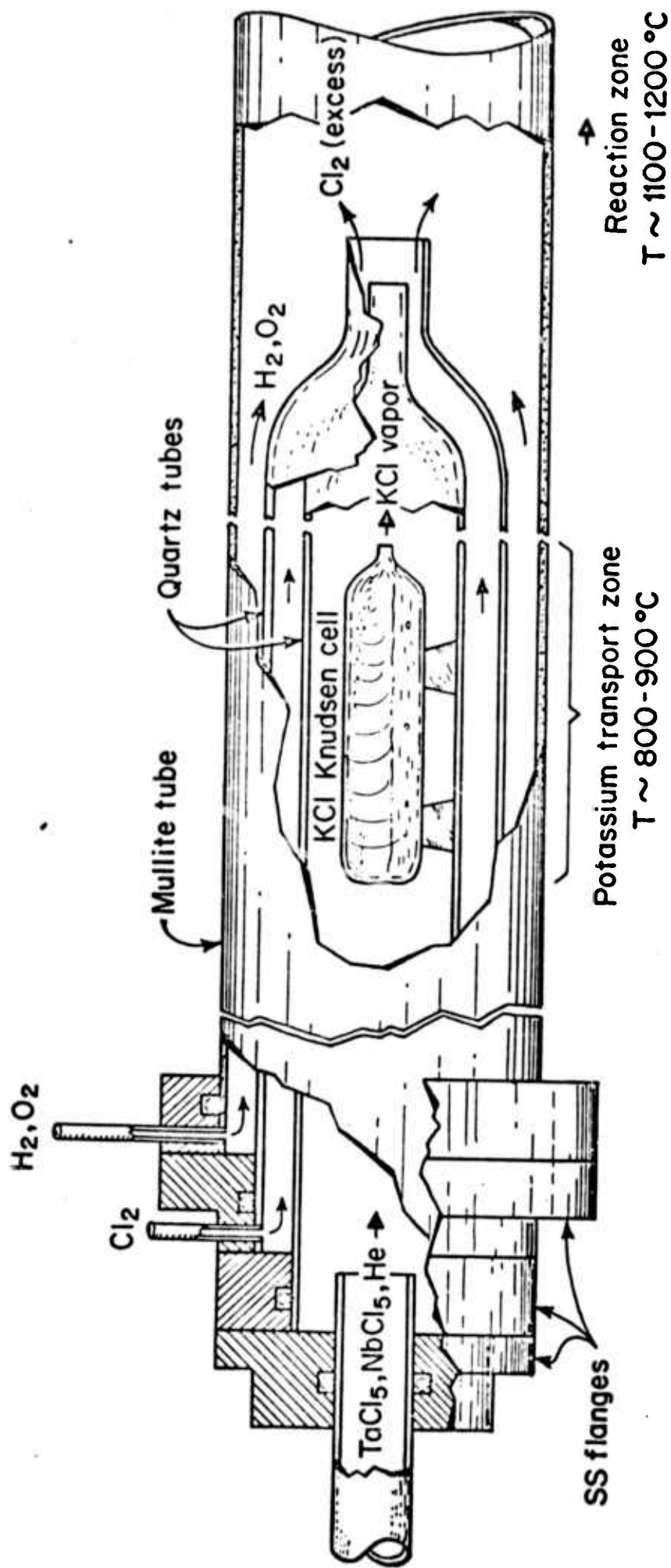
Fig. 4.13 Details of system for growth of KTN by chemical vapor deposition.
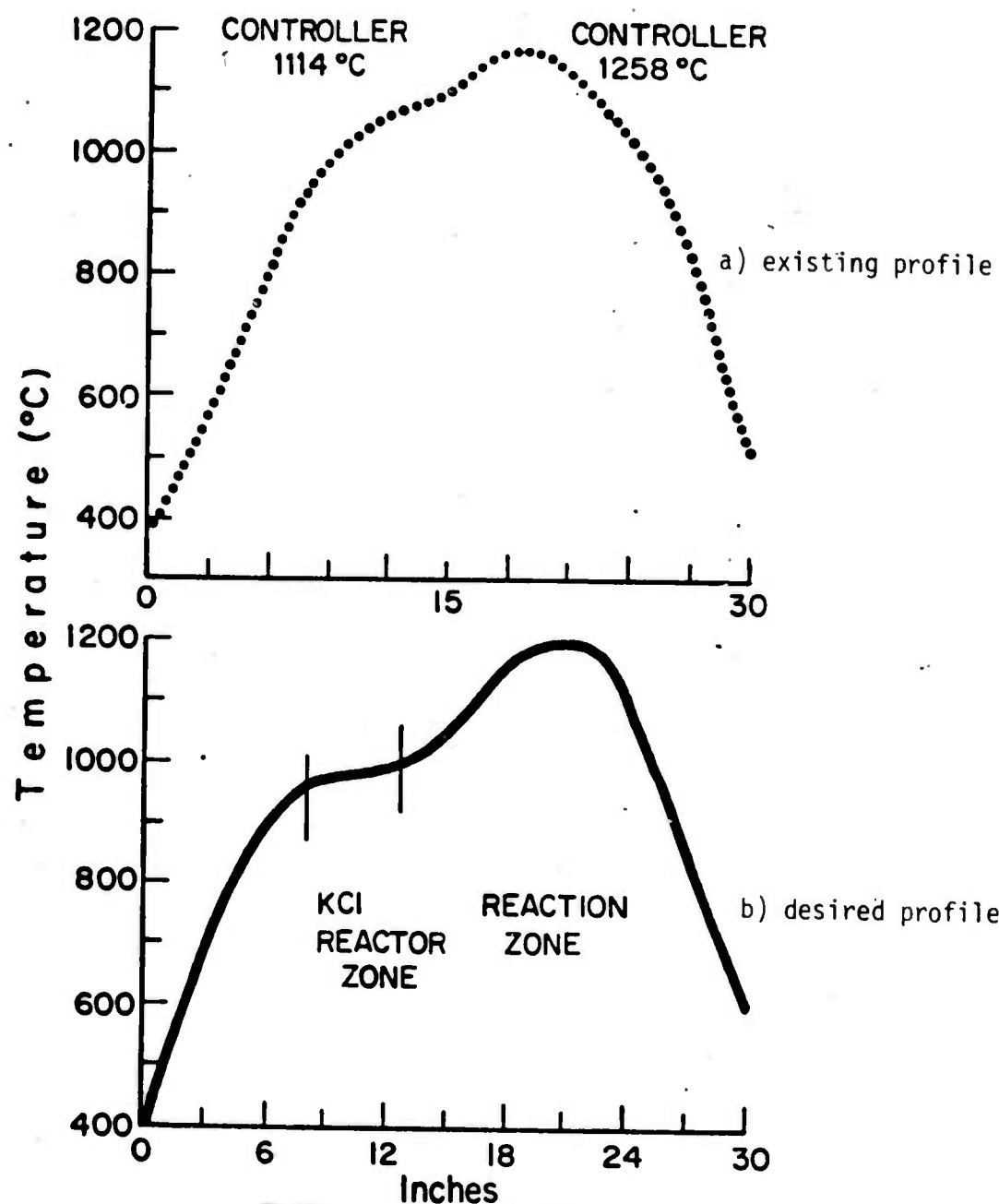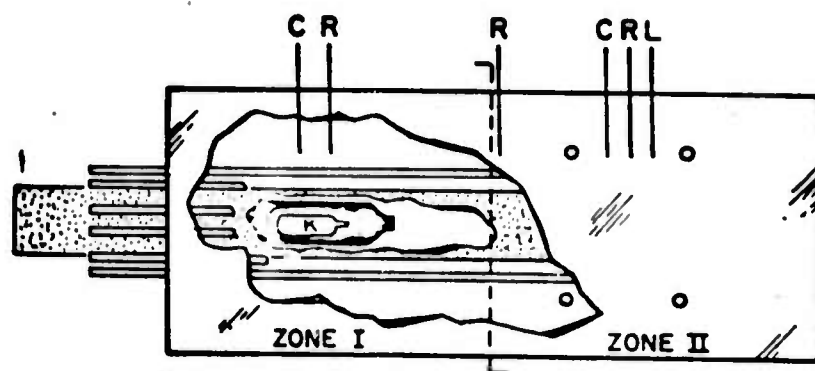
Fig. 4.14 Existing and ideal temperature profiles
for CVD furnace.

diameter gas-tight mullite reaction tube with four globars perpendicular to these in one half of the furnace. Each set of globars was separately controlled by an API Instruments controller. The furnace was thus divided into two thermal zones. Zone 1 contained the Knudsen cell which acted as a KCl reactor. The value of 950°C for the reaction tone was arrived at experimentally and corresponds to the temperature at which vapor pressure of KCl in the cell is sufficiently high to cause a gas flow large enough to react with $TaCl_5$ and $NbCl_5$. Zone 2 contained the substrates and/or seeds. It was found that $KTaO_3$ substrates reacted with Cl_2 gas and became ceramic like indicating that the amount of excess Cl_2 was a parameter that required further study.

At this point the LPE method proved an easier means of growing KTN thin film so that the CVD method was dropped and our full effort was shifted to liquid phase epitaxy.

4.6 Summary

In this two year research program we have developed a reliable LPE growth process for KTN films. Low optical loss waveguides have been produced and the integrated optics device potential of these KTN thin films has been demonstrated by the fabrication and operation of a KTN thin film modulator.

Work in this program will continue in the areas of multi-layered film growth, in a detailed analysis of the dielectric loss in the KTN films, and in new device configurations which can exploit KTN's large electrooptic effect.

V. LASER OUTPUT COUPLING

5.1 Synchronous Coupling

The dielectric cavity minilaser, described in earlier reports, can, in principle, be coupled to a dielectric waveguide via the evanescent field associated with the dielectric cavity mode. However, this scheme will work only if the refractive index of the dielectric cavity is large enough compared to the waveguide index to permit synchronous coupling between the cavity and waveguide modes. Unfortunately, the index of YLF ($n = 1.46$) is too low to permit this sort of coupling to the typical materials (e.g. oxides) which we would ordinarily want to use for thin film waveguides or modulators.

An obvious solution is to find a minilaser host with higher index. Oxide hosts fulfill this requirement and, in addition, are ordinarily superior to fluorides in their mechanical properties. For a laser host with sufficiently large index an internally reflecting laser mode can be quite accurately phase matched to an output guide (via the evanescent field) by cladding one or more of the side faces of the cavity with a dielectric film of properly chosen refractive index.

The foregoing schemes for output coupling depend on the ability to match the parallel components of wavevector in cavity and guide. When this is not directly possible, coupling can still be achieved by introducing into the coupling region a periodic grating that compensates for the wavevector mismatch. The periodicity of the grating must be chosen to ensure that the coupling between desired modes is achieved while at the same time there is no coupling from the laser to unwanted modes of excitation. The coupling strength provided by the grating is determined by the amplitude and contour of the periodicity as well as the refractive index of

the material from which the grating is fabricated. Theoretically the coupling efficiency of the scheme cannot equal that of the direct coupling scheme, because diffraction from the grating causes additional losses.

5.2 Grating Facility

We have constructed a system to expose very fine gratings in photoresist by holographic methods. The general physical arrangement is shown in Fig. 5.1. The beam from a helium-cadmium laser, which can operate at either 4416 Å or 3250 Å, is spatially filtered, expanded, and re-collimated to produce a beam $\simeq$ 1" in diameter with a uniform phase front. The beam is split by a 50-50 beam splitter and the two beams are allowed to interfere on a sample coated with photo-resist as shown in Fig. 5.1. In order that the interference fringes stay fixed with respect to the sample during exposure, it is necessary to place the entire set-up on a vibration isolation table. The system is capable of generating gratings with periods of $\simeq$ 5 μm - 0.18 μm. By immersing the sample in a bath of developer during the exposure, a technique called "simultaneous exposure and development", we have produced photoresist gratings of exceptional qualities.

The photoresist grating is next transferred to the sample by chemical etching. We have developed a new technique, whereby the sample is coated with a durable but more easily dissolvable thin film material before the grating is made and etched. The resultant grating depth will be just the thickness of the film coating, a quantity that is easily controllable.

Although a minilaser-waveguide coupler has yet to be demonstrated, we have successfully fabricated gratings in waveguides of photoresist, sputtered ZnO and single crystal KTN. When evaluated as beam-waveguide couplers, the gratings behaved as predicted by theory.

$$\Lambda = \frac{3250 \overset{\circ}{A}}{2 \sin \theta}$$
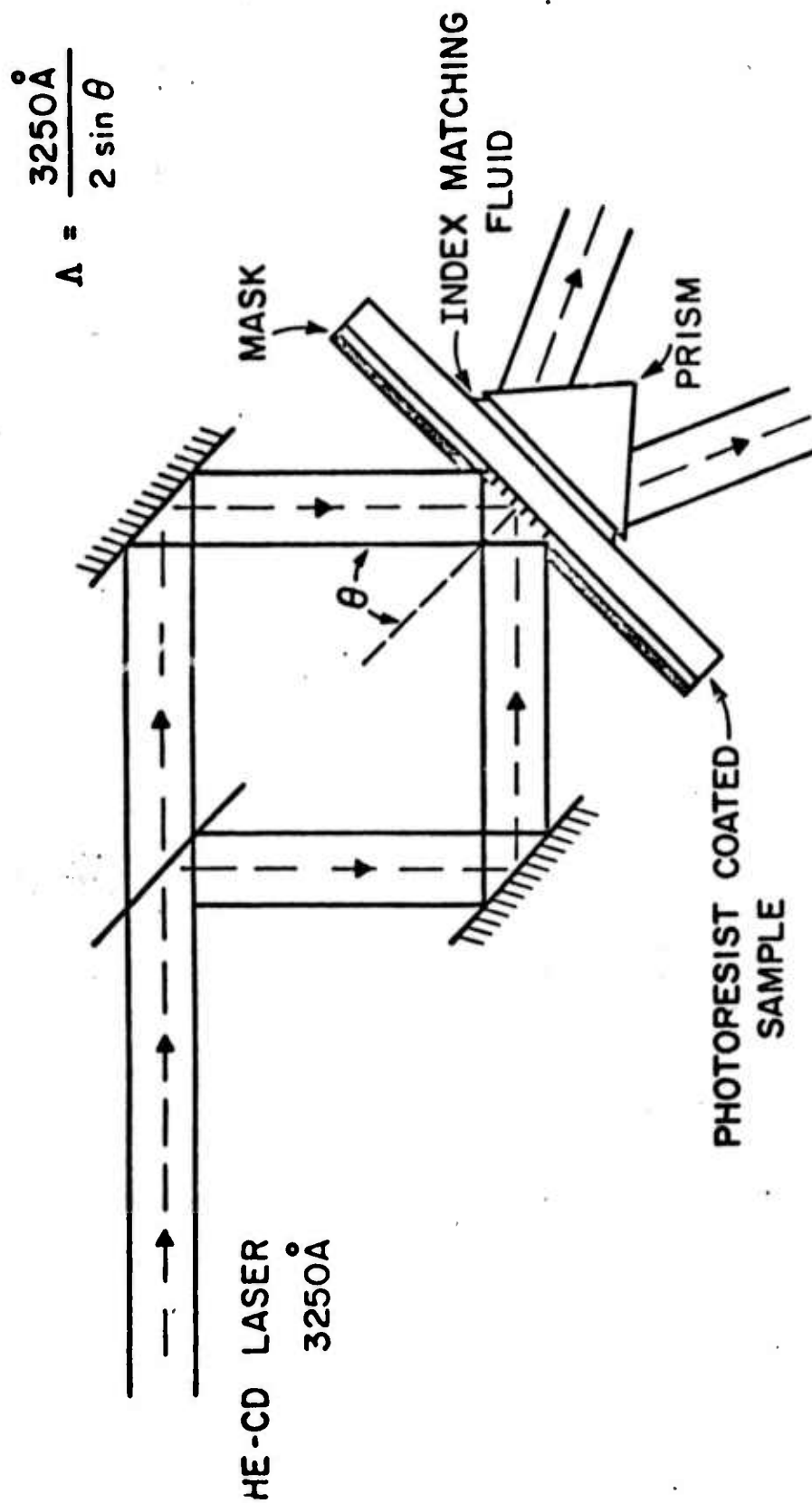
Fig. 5.1 Schematic of arrangement used for producing gratings in photoresist.

VI. PREPARATION OF FEED MATERIALS FOR
CRYSTAL GROWTH

6.1. Introduction

Sensitized rare earth minilasers requiring low activator concentrations demand extreme purity of the host/sensitizer combination. Important properties of laser materials affected by impurities are fluorescent lifetime of the active species, susceptibility of the host crystal to radiation damage, and light scattering from inclusions. To achieve the required improved purity levels, nearly all of the feed materials for crystal growth as well as virtually all of the auxiliary chemicals used in the processes must be purified, and laboratory equipment and air must be specially cleaned.

Purification and synthesis of oxide and fluoride materials as required by the minilaser program are being carried out using a variety of modern wet chemical separation techniques, zone refining and a newly developed low temperature hydrofluorination process. To obviate environmental recontamination during the chemical processing, all open operations are carried out in a Class 100 clean room. Closed equipment, including the centrifuge, carbon dioxide reactor, zone refiner, hydrofluorinators and fluoride growth furnaces are located outside of the clean room. Recontamination during use of this equipment is normally not encountered.

6.2 Clean Room

Our previous efforts to purify feeds have resulted in the development of a variety of methods for purification, but most of them have been of limited effectiveness owing to recontamination from the laboratory atmosphere.

During the early stages of the work under this contract, we completed the

installation of a Class 100 clean air chemistry laboratory designed and con-
structed by Environmental Air Control, Inc. of Hagerstown, Md. This labora-
tory is a room within a room, with an area of approximately 250 sq.ft. As shown
in Fig. 6.1, there are two front air-curtain type clean air hoods, one standard
laboratory hood, and two eight-foot laminar flow benches, all equipped with the
usual chemistry bench services. (This laboratory is used exclusively for the
preparation of the very high purity fluoride and oxide feed materials needed for
this program.) Great care is taken to maintain the integrity of the room by re-
stricting contaminant-shedding equipment to the barest minimum and by limiting access
to users only. Special clean room garments: hat, coat, gloves, and shoes are used,
not only to protect the worker, but to contain hair, lint, etc., and thereby mini-
mize recontamination of materials.

Operation of the room was recently disrupted by equipment failure caused
by premature aging of the air filter sealant, resulting in a complete loss of
filtration capacity and introduction of unfiltered air into the room. The prob-
lem has been corrected and the experience has heightened our awareness of the
frailties of clean room operation.

6.3 Chemical Techniques

All of the wet chemical procedures for preparation of purified feed
share a common scheme. The metal ion to be purified is brought into aqueous
solution. Filtration, the initial purification stage, serves to remove sub-
stances not dissolved. A series of extractive procedures is then applied to the
filtered solution. Just as all reagents entering the process stream must be of
sufficient purity to prevent recontamination of the raffinate, so too must all
implements be noncontaminating and specially cleaned. The intermediate result
is an aqueous solution of the desired metal ion, accompanied by a counter ion and
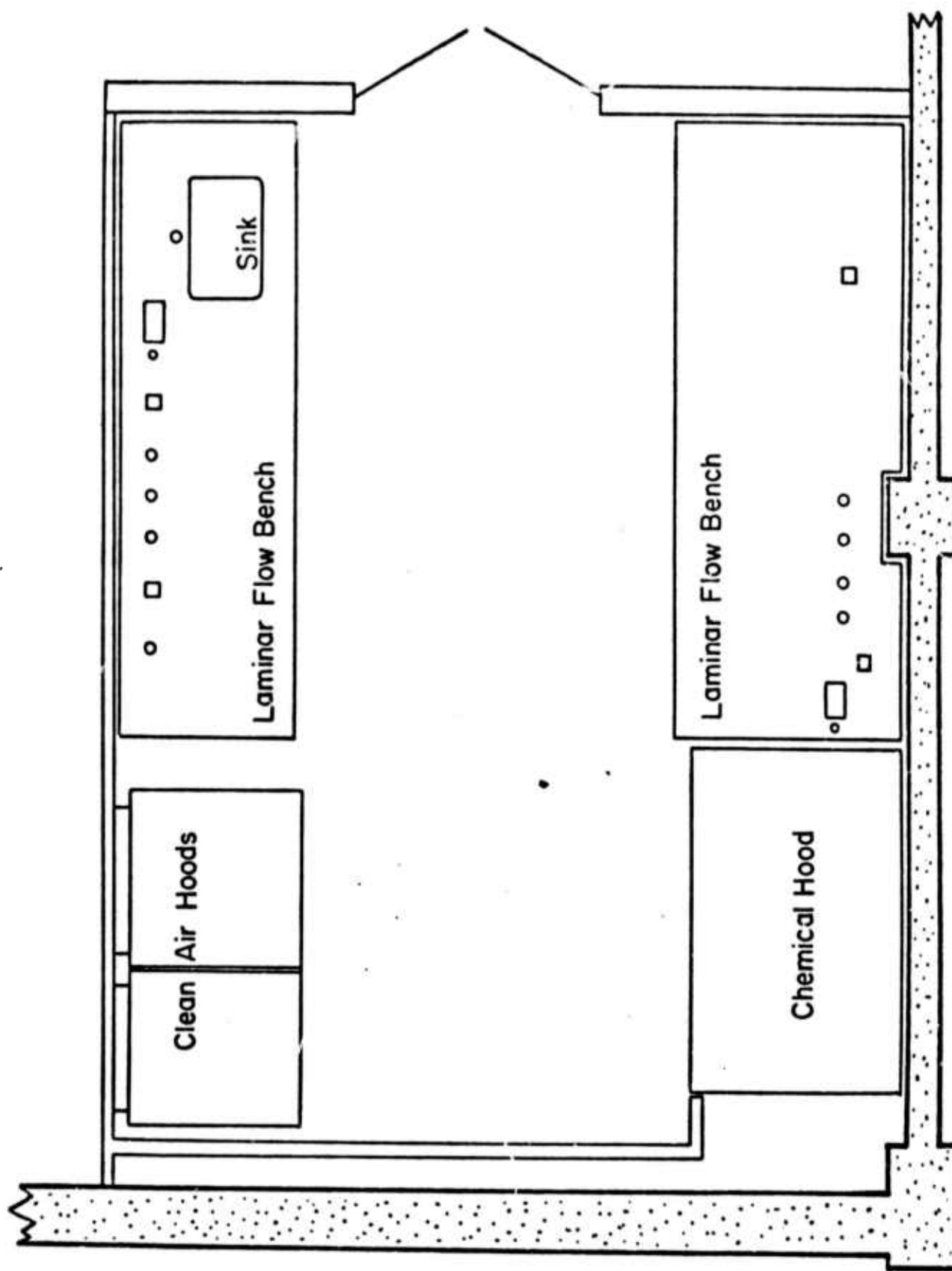
Fig. 6.1 Clean air chemistry room.

residues of extractive reagents. Recovery of the metal ion from solution is achieved by precipitation with a suitable anion (carbonate or oxalate) to form an intermediate solid compound. This compound is then converted to either oxide or fluoride crystal-growth feed by calcination or reaction with HF gas.

6.3.1 Separation and Purification: Some Comments

Although much can be written on this subject, only the basic features of chemical separation and purification will be discussed. The two qualities, separation and purification, go hand in hand. Separation means spatial separation of impurities from sought components, while purification follows from the efficiency of the separation process and is conditioned by chemical as well as physical factors. At the root of the separation is the chemical system in which two phases are in equilibrium[*]: the phase to be purified and an extractive second phase. To a greater or lesser extent species present initially in one of the phases will at equilibrium be found in both phases. This distribution is characterized by the concentration ratio

$$k_i = \frac{(S_i)_{phase\ 1}}{(S_i)_{phase\ 2}}$$

where k_i is a distribution constant and S_i is the concentration of the ith species. To achieve separation of impurity species from the material or solution being purified, the ratio of the respective k's (separation factor) must differ from unity. Individual phases in equilibrium mixture are mechanically distinct entities; thus, through the action of preferential distribution the desired spatial separation

* Kinetic separation processes are not considered here

is obtained. Purification is implemented by mechanically separating the phases. Clearly both the chemical and physical aspects of separation and purification are important, as the purity of the final product is a function of the efficiency of each of these two processes. When a single stage of separation/purification is not sufficient, the process may be repeated.

In this work only a few specialized separation methods have been applied to the synthesis of large amounts of high purity chemical for crystal growth applications. Chemical systems have been chosen for which high separation factors are combined with easy mechanical separation of the phases. Table 3 lists the various methods used, the phases involved, the mechanical process and important mechanical limitations.

6.3.2 Purification by Solvent Extraction

This term denotes a separation and purification process in which the two phases in equilibrium are an aqueous solution and an organic solvent of differing densities. Equilibrium is established through violent shaking to effect mixing and to maximize the area of the phase boundary. Mechanical separation is achieved in a separatory funnel after allowing the phases to coalesce and separate into two layers; the denser phase is drawn off through a stopcock.

Two solvent extraction systems have formed general use in our laboratory: in one, the extractant is diethylammonium diethyldithiocarbamate (DDDC) dissolved in chloroform; the other employs 8- hydroxyquinoline(oxine), also dissolved in chloroform. DDDC forms chloroform soluble chelates with a broad spectrum of metal ions. Significant exceptions are the rare earths, alkaline earths, alkali metals and aluminum, which are not extracted. Distribution ratios and separation

Table 3

SEPARATION METHODS

Method	Phases in Equilibrium	Mechanical Process	Mechanical Limitations
1. solvent extraction	purified extrinsic aqueous / organic	distribution followed by coalescence and draining of denser phase	incomplete coalescence of dispersed phase
2. zone refining	solid/melt	directional crystallization of shaped charge	trapping of liquid phase by recrystallizing solid
3. precipitation	solid/solution	filtration	trapping of solution within solid phase, liquid hold up

are therefore extremely favorable, allowing purification with respect to extractable species to the ppb level.

In practice, about 10 ml of a 2% solution of DDDC dissolved in chloroform is equilibrated with about 1 liter of the aqueous solution to be purified. The presence of extracted metal ions in the chloroform phase is indicated by a yellow to brown coloration. The extraction-mechanical separation stages are repeated until the chloroform phase remains colorless. The pH of the aqueous solution is an important parameter because the distribution coefficients of many metals are pH dependent. Therefore, extractions are conducted over a range of pH's from about 1 to the maximum realizable in the given system.

For metals that cannot be extracted by DDDC we have found oxine to be a useful chelating extractant. For example, Al can be extracted at pH 4 in the presence of large amounts of rare earths, alkaline earths and alkalis. For the oxine system there is a strong pH dependence of the distribution coefficient and separation factors.

6.3.3 Centrifugal Filtration

It is important after precipitating a compound from solution to separate it as completely as possible from the solid phase. The separation is done by collecting the precipitate on an acid washed PTFE filter disc in a plastic Büchner funnel. Care is taken not to suck the filter cake dry. Rather, separation of the aqueous phase is accomplished by centrifuging the filter funnel basket in an IEC type K centrifuge equipped with a four place head with 600 cc cups. The plastic bottles designed for these cups are cut below the shoulder and serve as containers for the funnel basket which is supported on an inverted plastic beaker which has a vent hole in its bottom. Saran wrap secured with a rubber band is used to cover the container. This assembly must be dynamically balanced with a similar unit.

Thus two funnels full of precipitate are simultaneously centrifuged dry. The precipitate is then washed several times while on the funnel, using centrifugal action. A considerably better separation of precipitate from the supernatant liquid is achieved using the centrifugal method rather than conventional vacuum filtration.

6.3.4 Homogenous Precipitation

Homogenous precipitation is a technique in which one of the species partaking in the precipitation reaction is generated in situ by slow chemical reaction. The character of a precipitate formed by this method differs in several important ways from one formed directly by simply mixing two solutions. Crystallinity, crystal habit (dendritic or prismatic), particle size and formation of undesired solid phases are a function of the rate of precipitation of the local concentrations of reactants, of reactant concentration gradients, and of the solubility of the precipitate.

The rare earth carbonates are fairly insoluble and are precipitated at a pH where the hydroxide is stable but not as stable as the carbonate. When formed by simply mixing solutions of rare earth ions with ammonium bicarbonate, kinetic factors play a significant role leading to contamination of the precipitated rare earth carbonate with hydroxycarbonates. The latter phase is undesirable, as it imparts a sticky character to the carbonate, making it difficult to filter, wash and dry. This contaminant also appears to affect the reactivity of the carbonate with HF gas and we believe may be responsible for incomplete hydrofluorination.

Absence of hydroxycarbonate phases, improved crystallinity, prismatic crystal habit, and large particle size resulting from slow precipitation at low supersaturation, allows the product to pack more densely, minimizes inclusions of liquid phase and

provides a rare earth carbonate with desirable physical and chemical properties.

6.3.5 Synthesis of Carbonates under CO_2 Pressure

Feed for melt growth of oxide crystals must be either an oxide or a compund that can be decomposed thermally in situ to form an oxide. The choice of such compounds is small and is even further restricted by the requirement of high purity. Hydroxides and hydrous oxides, while easily precipitated from purified aqueous solution, are almost always extremely difficult to wash free of the foreign ions left in solution by the precipitation reaction. These solids are sticky and usually form quite hard large lumps when dried, making further use difficult.

Salts of low molecular weight organic acids in particular are good candidates for decomposition to acids but their synthesis entails purification of the organic acid and decomposition to the oxide is complicated by formation of CO and elemental carbon which can attack a platinum crucible. Predecomposition to the oxide in a separate furnace using quartz vessel during active CO evolution (300-500°C) and platinum thereafter is usually required.

Metal carbonates, on the other hand, undergo thermal decomposition to the corresponding oxide with little difficulty:

$$MCO_3 \rightarrow MO + CO_{2(g)}$$
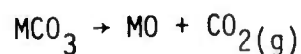
and may be used directly as feed for melt growth of oxide crystals.

All of the carbonates are precipitated from purified aqueous solution and must be well crystallized and uncontaminated with hydroxides so that the solid can be easily filtered, washed and dried to a free flowing uncontaminated solid.

Methods have been developed for synthesizing and recrystallizing metal carbonates from solutions saturated with CO_2 at pressures up to 250 psig. The solubility of many carbonates in water is greatly increased when the solution is saturated with CO_2. Two contributing effects are reduction of the $CO_3^=$ ion concentration via reaction with dissolved CO_2,

$$CO_3^= + H_2O + CO_2 \rightarrow 2HCO_3^-,$$
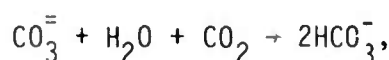
and formation by metal ions of soluble bicarbonate complexes,

$$MCO_3 + H_2O + CO_2 \rightarrow M(HCO_3)_2$$
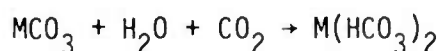
$$(M = Mg, Ca, Ba, Ni, etc.).$$

The actual complex bicarbonate species predominating will differ from metal to metal. In the case of Mg and Li, their carbonates are appreciably soluble in water under CO_2 pressure; further, the solutions are metastable at ambient CO_2 pressure and temperature, allowing purification by solvent extraction. Gentle heating, preferably using a bain-marie, decomposes the bicarbonate solution precipitating the metal carbonate. These compounds are obtained as very well crystallized single phase materials.

Other carbonates, notably those of Y and Er, although only slightly soluble under CO_2 pressure, separate as well formed sub mm size crystallites when precipitated from a homogenous solution pressurized with CO_2. Details of the working procedures we have developed will be given in later paragraphs that deal with specific compounds.

The pressure reactor used is of all stainless construction and is sealed with rubber "O" rings. The full volume is close to 6 liters, but the available glassware limits the working volume to a little over 2.5 liters.

6.3.6 Zone Refining

A zone-refiner shown in Fig. 6.2, designed in this laboratory is available for purification of air-sensitive materials which must be melted either in vacuum or a high purity inert atmosphere. The equipment is RF powered, employing a graphite or tantalum susceptor and a single flat concentrator type work coil. A molten zone of 1"to 1.5"long can be maintained. Either 12" or 18" long vitreous carbon boats contain the charge; the longer boat is preferred to optimize segregation of impurities.

We have demonstrated that rare earth fluorides may be purified with respect to other rare contaminants. This result is of special significance in that, for the compounds investigated, zone-refining has yielded material purer than one can obtain commercially. The zone-refining operation is easily set up and runs unattended. Even after many purification stages the yield remains high.

The results of extensive zone-refining of $LiErF_4$ will be discussed in a later section dealing with preparation and purification of Er compounds.

6.3.7 Low Temperature Hydrofluorination

A low temperature process for synthesis of anhydrous rare earth fluorides from the carbonates has been developed. Rare earth input is in the form of well crystallized carbonate synthesized by homogenous precipitation. Conversion to fluoride is carried out in a Teflon reactor with HF gas at 300°C. The major advantages of this method over the commonly used techniques for fluoride synthesis are:

1. The major wet HF load is exerted on an inert Teflon reactor rather than on a corrodable metal system or on an inert but quite expensive platinum reactor.
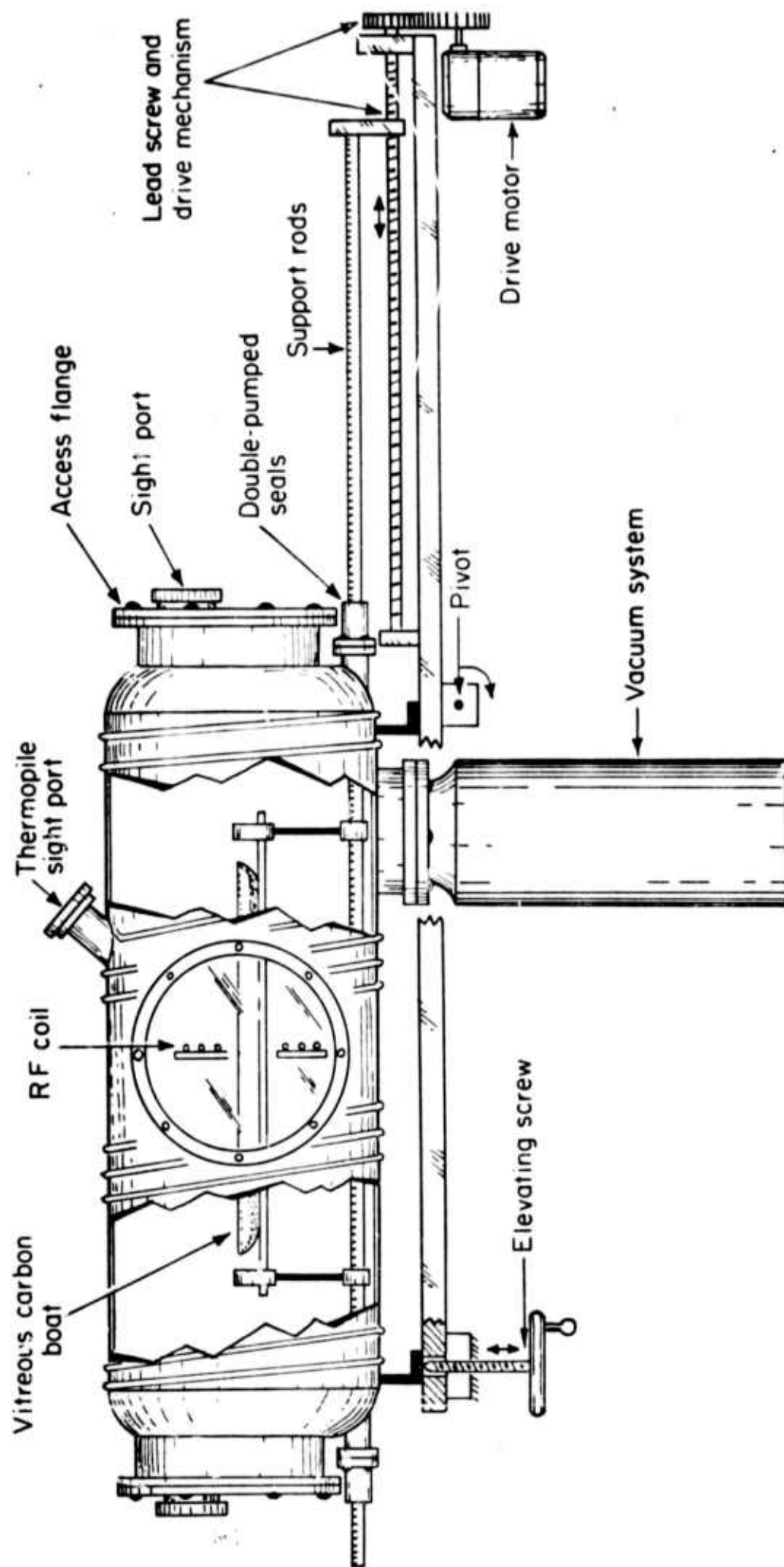
Fig. 6.2 HIGH TEMPERATURE FLUORIDE ZONE REFINER

2. Preparation of a highly purified rare earth carbonate is easier than preparing the oxide of corresponding purity for use as the fluoride precursor.

3. Continued hydrofluorination further to reduce the oxygen content of the rare earth fluoride may be easier compared to other processes.

4. A crystalline product free of oxyfluoride or oxide phases is obtained at 300°C.

6.4 Chemicals and Reagents: Sources and Purification

6.4.1 Urea

Reagent grade urea is commercially available as a fairly pure product. Chemical tests have indicated that copper is probably the major transition metal contaminant, while sodium is reported by the manufacturer to be the major metallic impurity. In the case of one supplier, J.T. Baker Chemical Company, changes in the manufacturing process to produce a prilled rather than a crystallized product resulted in serious contamination with copper. This contaminated urea had a distinct blue-violet color in both solid and solution and in some cases a pale green water-insoluble residue (probably a copper carbonate) was present. Under normal conditions such an impure material would have been rejected, but availability of a better product from another manufacturer was not certain. This uncertainty has now been resolved, at least for the present, in that satisfactory lots from other manufacturers have been found.

The purification procedure discussed below has been developed to handle copper contaminated urea, but is not unnecessarily complicated for application to a purer starting material.

About 3 liters of saturated solution of urea is prepared at 50-60°C and about 1 g of DDDC is dissolved in this solution. The bulk of the copper precipitates and is removed by filtration along with any initially insoluble copper compounds. The warm solution is then extracted with DDDC in chloroform at neutral and basic pH's and cooled in an ice bath to crystallize the urea and effect separation of Na. When the copper and other transition metal contamination in the starting material is very small, as is usually the case, the bothersome filtration of the warm urea solution may be eliminated.

The solid is then collected on a medium porosity Teflon filter in a plastic Büchner funnel and centrifuged dry. Washing of the precipitate is not practical, owing to the high solubility of urea. When needed, the urea is dissolved in water at room temperature and tested by extraction at pH2 and also at pH7; pH adjustments are made with ammonia.

Solutions of urea may also be effectively purified by ion exchange using a mixed bed-strong acid-strong base exchanger. Preliminary experiments have shown the feasibility of the method, but conditions for preparation of large amounts of purified urea solution have not yet been completely defined. It is anticipated that the convenient ion exchange method will replace the more tedious extraction/crystallization method now used.

6.4.2 DDDC

Although available commercially from several suppliers, delays in delivery combined with the need for further purification have made it necessary to synthesize DDDC in the laboratory.

It is not known whether the impurities are organic or inorganic, but in any event they remain in the chloroform phase when extraction is carried out, discoloring

it and causing difficulty in deciding when a series of extractions should be term-
inated.

Carbon disulfide and diethylamine react exothermally to produce DDDC. The re-
action may be carried out by slowly adding a solution of CS_2 in hexane to a cooled
stirred solution of $(C_2H_5)_2NH$ in hexane. The product may be recrystallized from warm
hexane but care should be taken not to saturate the solution above the melting point
of DDDC; otherwise, the first phase to separate on cooling will be a liquid.

6.4.3 8 - hydroxyquinoline (oxine)

This reagent is recrystallized from a water-ethanol mixture to yield fine white
needles which dissolve in chloroform forming a colorless solution.

6.4.4 Water

The traditional ways of purifying water, distillation or ion exchange, are in-
sufficient. It is now recognized that despite elaborate mixing to prevent it, carry
over of spray and liquid creep from the boiling pot limits the purity of water ob-
tainable by ordinary distillation. (The impurity distribution ratios between liquid
and vapor phases are highly favorable, but imperfect mechanical separation of the
phases is a limiting factor. Sub-boiling distillation which avoids these problems,
represents a major advance in the state of the art of purification by distillation.)
Although ion exchange is extremely efficient in removing ionic impurities from water,
many impurities occur as submicron size insoluble products that pass through the
column unaffected. However, when combined with a submicron membrane filter water
purity in excess of eight 9's is routinely obtained. The ion exchange system used
in our laboratory is fed with distilled water from the building supply, passed through
a mixed bed ion exchanger, an organic removing sorption system and finally through a

submicron membrane filter. To maintain quality of the stored water, it is continuously circulated through the purification system. Water for use is drawn into a polyethylene bottle and brought into the clean room.

In having to share the water supply with other users, there lies a potential source of contamination; therefore, water quality is frequently tested by solvent extraction.

6.4.5 Oxalic Acid

Reagent grade oxalic acid must be purified by solvent extraction with DDDC in chloroform. Small amounts of iron and copper are the major transition metal impurities. There is no indication from direct chemical tests or from tests on an oxalate process oxide feed that further purification should be applied to this substance.

6.4.6 Other Acids and Ammonia

Reagent grade hydrochloric and nitric acids and aqueous ammonia are all of sufficient purity to be used without further purification.

6.4.7 Carbon Dioxide

Carbon dioxide is drawn directly from a cylinder of commercial gas for use in the pressure reactor.

6.4.8 Ammonium Carbonate

Reagent grade ammonium carbonate contains traces of non-extractable iron and copper. These may be removed by co-precipitation with a suitable metal carbonate. For synthesis of $CaCO_3$, for example, a nearly saturated solution of ammonium carbonate is treated with purified calcium carbonate until a permanent precipitate just forms.

The precipitate is then dissolved in HCl and tested for transition metal contamination by color and by extraction with DDDC in chloroform. The extractive precipitations are repeated until impurities are no longer detectable. Usually two to four stages are required.

6.4.9 Formic Acid

Reagent grade formic acid is heavily contaminated with iron that is not removed by extraction with DDDC in chloroform. Efforts are currently being made to purify this substance by distillation.

6.5 Chemicals: Sources of Material to Be Processed Into Crystal Growth Feed

6.5.1 Rare Earth Products

These are obtained as oxides or fluorides from Research Chemicals, Inc., Phoenix, Arizona. The stated purity, 99.99%, 99.999%, etc., refers to the rare earth purity only. Typically the major impurities are Fe, Cu, Ca and Al.

6.5.2 Calcium and Magnesium

Reagent grade chemicals are the source of these metals. Purities vary from lot to lot; again Fe and Cu are the major transition metal contaminants, but sometimes a considerable amount of Ag can be found in Ca salts.

6.5.3 Tantalum Pentoxide

For growth of $KTaO_3$, Ta_2O_5 is normally purchased from Kawecki, Inc. In general this material has proven satisfactory. During the course of this work, discoloration and precipitation of a second phase in the $KTaO_3$ crystals as well as vanadium bearing deposits at the mouth of the oxide crystal growing furnace were obtained when a new

lot of Ta_2O_5 feed was used. A second lot from the same supplier as well as a lot from Johnson Mathey showed similar behavior.

Vanadium in the furnace deposits was identified by x-ray fluorescence. Impurities in the crystal have not yet been identified.

Fortunately, during crystal growth the impurities segregate in favor of the solid, resulting in a crystal with the top half contaminated and the bottom half clear and usable.

6.5.4 Germanium Dioxide

Germanium dioxide is obtained from Eagle Pitcher as electronic grade and is used without further purification.

6.5.5 Potassium Carbonate

Reagent grade potassium carbonate is used without further purification.

6.5.6 Nickel

Nickel metal was obtained from Leico Industries in the form of a bar. The stated purity was 99.999%.

6.6 Synthesis of Crystal Growth Feed Materials

6.6.1 Introduction

The purity of feed for oxide crystals has been rather more problematic than for the fluorides because trace transition metals are more easily incorporated into the oxides than into the fluorides. Before the clean chemistry laboratory was built, synthesis of high purity feed was nearly impossible due to environmental recontami-

nation. This is no longer a problem and considerable progress has been made in the synthesis of high purity materials.

The methods of synthesis discussed will in some cases differ from what was previously written in the interim reports. The newer procedures reported here are simpler, have fewer steps, are easier to implement, and yield products with better physical properties and higher purity.

6.6.2 Y and Er Compounds

These rare earth elements are components of both oxide and fluoride laser hosts. The initial purification stages are the same for both end products.

Commercial rare earth oxide having the desired rare earth purity is dissolved by adding hydrochloric acid to a vigorously stirred water suspension of the oxide. If the reaction is carried out carefully, a residue of small red particles will remain after virtually all of the oxide has been dissolved. These were shown by X-ray fluorescence analysis in a scanning electron microscope to contain Fe or a mixture of Fe and rare earth.

The solution is diluted to about 2 M in Y^{3+}, filtered and extracted at pH1 and then at pH4 with DDDC in chloroform. The upper pH is bounded by hydrolysis of the rare earth ion. In adjusting the pH, aqueous ammonia is added until a permanent precipitate of rare earth hydroxide is formed. This precipitate which acts as a scavenger collecting some impurities is removed by filtration. Extractions are repeated at each pH until the chloroform phase remains colorless.

Following the DDDC extractions the rare earth chloride solution at pH4 is extracted with 8-hydroxy-quinoline in chloroform. Aluminum is the primary target of this procedure.

Analysis of combined extracts, including the hydroxide precipitate, by X-ray fluorescence shows Fe, Cu and possibly Zn and Pb (not always detected, may have been an artifact) to be the major impurities. Traces of aluminum are also indicated. This purified chloride solution is then used for rare earth input to the oxide or fluoride yielding process.

For preparation of Y and Er oxides the purified chloride is diluted to about 0.5 M in Y^{3+} or Er^{3+} and precipitated with a saturated solution of purified oxalic acid. This oxalate is collected and washed by centrifugal filtration. Rare earth oxalates cannot be used directly as crystal growth feed. Thermal decomposition of the oxalate to the oxide is accompanied by evolution of CO and CO_2, and formation of some elemental carbon. To avoid attack on Pt by CO and C, the decomposition is carried out in a Vycor crucible. Calcination at 1100°C on a Pt crucible results in oxidation of residual carbon and considerable grain growth of the respective oxides. This method can also be used for synthesis of all the other rare earth oxides.

In the fluoride process reported below, a rare earth carbonate intermediate is produced which could be used directly without pre-decomposition to the oxide as crystal growth feed. But for reasons of chronology we are only beginning to use this method as a route to oxide feed.

Y and Er fluorides are prepared from the respective carbonates by low temperature hydrofluorination (300°C) in a Teflon reactor. Starting with purified urea and the purified RE chloride solution at pH4, well crystallized yttrium and erbium carbonates are synthesized by homogenous precipitation under CO_2 pressure. The overall reaction is

$$6H_2O + 3(NH_2)_2 CO + 2 YCl_3 \rightarrow Y_2(CO_3) + 6NH_4Cl$$
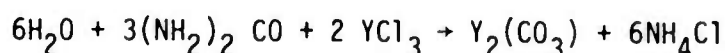
The reaction conditions are: 0.5 M RE, 1.5 M urea (double the stoichiometric amount),

12-15 atm CO_2 pressure, 85-90°C, unstirred. The reaction mixture is allowed to cool to room temperature under CO_2 pressure. Collection and washing of the precipitate is done with the aid of the centrifuge. Yttrium and erbium carbonates prepared by this process were dense and showed no trace of stickiness. The crystallites were of the order of 0.02 mm in size, were transparent, and gave a sharp well-defined X-ray powder pattern in excellent agreement with published data.

Regarded as significant is the formation of these carbonates from 0.5 molar solution which means that yield and throughput need not be sacrificed to obtain a well crystallized product. In previous work on homogenous precipitation of $Y_2(CO_3)$ 0.0002 to 0.001 molar solutions were used at ambient CO_2 pressure*.

Synthesis of the fluoride is achieved by reacting the carbonate with flowing HF at 300°C for about 4-5 hours, followed by drying in flowing Ar at 300°C for about 12 hours.

The X-ray powder patterns are well defined, in excellent agreement with those of single crystal material, and show no evidence of oxyfluoride phases.

For crystal growth the carbonate-process feed can be used directly. The yield of usable $LiREF_4$ will be limited by the onset of two-phase fluoride-oxyfluoride crystallization**, but this is of secondary importance when a small crystal of the highest possible purity is desired.

6.6.3 Lithium Erbium Fluoride: Purification by Zone-Refining

Zone refining has been applied to the purification of rare earth fluorides princi-

---

* K. Nakashima, et al. Bull. Chem. Soc. Jap., 46, 152, (1973)

** For a more complete discussion see the report, "Development of Multiply Sensitized Ho:YLF as a Laser Material" by E.P. Chicklis, R.C. Folweiler, C.S. Naiman, D.R. Gabbe, A. Linz and H.P. Jenssen; ECOM-73-0066-F, October 1974.

pally to effect removal of trace rare earth contaminants.

Spectroscopic studies of $LiREF_4$ compounds have indicated that trace rare earths can be significant impurities. As an indicator of the purity we measured the $^4I_{13/2}$ lifetime. In the initial material before zone-refining the $^4I_{13/2}$ lifetime was something like 0.6 milliseconds. Repeated zone-refining of $LiErF_4$ resulted in a monotonic increase in lifetime of the $^4I_{13/2}$ state from 2.3 msec after 5 passes to 8.5 msec after 28 passes. Fluorescence measurements also indicate removal of Ho and Tm as the zone-refining progresses. The rare earth purity achieved is greater than that of the commercial 99.999% material.

6.6.4 Magnesium Carbonate

Reagent grade magnesium carbonate is dissolved in purified water under about 12-15 atm CO_2 pressure at room temperature. The resulting metastable solution contains about 40 g. fl. of $MgCO_3 \cdot 3H_2O$. Transition metal impurities, notably iron, are somewhat soluble in aqueous CO_2 as well, but tend to be released in the excess undissolved magnesium carbonate which is removed by centrifugation in 1 liter polyethylene bottles. The clear magnesium bicarbonate solution is then filtered through a medium porosity glass frit and extracted at the prevailing pH with DDDC in chloroform. During extraction a small amount of $MgCO_3 \cdot 3H_2O$ forms and is removed by filtration. The purified magnesium bicarbonate solution is then decomposed by gentle beating using a bain-marie. Precipitation is terminated before it is complete. Millimeter long needles and rosettes of single phase $MgCO_3 \cdot 3H_2O$ precipitate. This is collected on a plastic Büchner funnel, weighed and dried by centrifugation.

A troublesome property of magnesium carbonate is its low bulk density which makes tedious obtaining an adequate crucible fill for an oxide crystal growth run.

In spite of the size of the crystals precipitated from a magnesium bicarbonate solution, their shape precludes dense packing. Pre-decomposition to the oxide at 1100°C does not result in appreciable densification.

6.6.5 Magnesium Oxide

A process has been developed for synthesis of a moderately high bulk density magnesium oxide from the formate. Purified magnesium carbonate prepared as outlined above is reacted with $\sim$ 80% formic acid. A metastable solution of magnesium formate is obtained which crystallizes slowly to yield 1/2 mm size prisms. A second crop of magnesium formate prisms may be obtained by evaporating the filtrate from the first crop. Heating at 400°C in Vycor crucible to decompose the formate, followed by cal-cining at 1100°C in a Pt crucible has yielded magnesium oxide with a considerably higher bulk density than the carbonate, and about twice the bulk density of reagent grade MgO.

6.6.6 Calcium Carbonate

Calcium chloride dihydrate dissolved in water at the rate of about 450 g/l is purified by filtration and solvent extraction at pH1, 7, and finally 10 $\sim$ 11, with DDDC dissolved in chloroform. The solution is then diluted with an equal amount of water and precipitated with a saturated solution of ammonium carbonate. Collection on a Büchner funnel, followed by centrifugal washing and drying is done in the usual way. Finally, the $CaCl_2$ is dried in a heated vacuum deaerator at 70°C and $\sim$ 11 torr (water pump).

This $CaCl_2$, which is used directly as crystal growth feed, is assayed by decomposing a sample at 1100°C and weighing as the oxide.

6.6.7 Nickel Carbonate

High purity nickel carbonate was synthesized from commercial high purity
nickel metal. A nitrate solution prepared by dissolving the metal in reagent grade
nitric acid was made basic with an amount of ammonia equivalent to the formation of
$Ni(OH)_2$. Reaction of this solution with CO_2 under pressure produced crystalline nickel
carbonate in moderate yield. Almost all of the nickel remaining in solution was in
the form of nickel-ammonia complex ions, while a small fraction was in the form of
nickel-bicarbonate species. Nickel ions are completely soluble in ammonium carbonate
as nickel-ammonia complexes. Pressurization with CO_2 decreases the pH and the dis-
solved NH_3 concentration, allowing precipitation of $NiCO_3$.

6.7 Fluoride Crystal Growth

Crystal growth of fluorides by the top-seeded solution method has been de-
scribed in detail elsewhere*. For the minilaser program the crucible size has been
scaled down from 150 to 25 ml and the melt size from 130 to 25 to 30 g. This re-
duction in the mass of feed required for a given run makes economical application of
extensive chemical purification to all of the fluoride materials used.

6.8 Summary

Drawing upon known chemistry we have developed procedures for synthesis of

---

* See the following references: 1) E.P. Chicklis, R.C. Folweiler, C.S. Naiman, et al.,
  "0.85 Micron Solid State Laser Evaluation", Tech. Report AFAL-TR-73-94, April 1973;
  2) E.P. Chicklis, R.C. Folweiler, C.S. Naiman, A. Linz, H.P. Jenssen and D.R. Gabbe,
  "Development of Multiply Sensitized Ho:YLF as a Laser Material", Research and
  Development Technical Report TR, ECOM-0015-F, January 1973, Sanders Associates, Inc.,
  Nashua, New Hampshire.

high purity oxides and fluorides as required by the minilaser program. Notable results are:

   a) significant purification, with respect to trace rare earth impurities, of rare earth fluorides by zone refining;

   b) development of a homogenous precipitation process for bulk synthesis of well crystallized, single phase rare earth carbonates;

   c) development of a low temperature hydrofluorination technique for synthesis of well crystallized anhydrous rare earth fluorides;

   d) development and implementation of chemical and manipulative techniques for bulk synthesis of ultra pure crystal-growth feed.

VII. <u>PUBLICATIONS AND TALKS</u>

1. "Single Mode 2.06 μm Miniature Laser", D. Castleberry, H.P. Jenssen and A. Linz; presented at the Integrated Optics Conference, New Orleans, January 1974.

2. "Growth and Characterization of Silicon Doped $GaAs_xSb_{1-x}$ Luminescent Diodes", S.K. Brierley and C.G. Fonstad, Jr.; presented at the 1974 IEEE Specialist Conference on the Technology of Electroluminescent Diodes, November 20-21, 1974, Atlanta, Georgia.

3. "Analysis of the Optical Spectrum of Tm^{3+} in $LiYF_4$", H.P. Jenssen, A. Linz, R.P. Leavitt, C.A. Morrison and D.E. Wortman; Phys. Rev. B $\underline{11}$, 92 (1975).

4. "Efficient Silicon Doped $GaAs_xSb_{1-x}$ Luminescent Diodes Emitting to 1.06 μm", S.K. Brierley and C.G. Fonstad, Jr.; to be published in Applied Physics Letters.

5. "Epitaxially Grown Single Crystal KTN for Thin Film Optical Modulators", R.E. Fontana, D.J. Epstein, A. Linz; presented at the 1975 CLEA Conference, Washington, D.C.

6. D.E. Castleberry and A. Linz, "Measurement of the Refractive Indices of $LiYF_4$"; to appear in Applied Optics, September 1975.

SECURITY CLASSIFICATION OF THIS PAGE (When Data Entered)

REPORT DOCUMENTATION PAGE		READ INSTRUCTIONS BEFORE COMPLETING FORM
1. REPORT NUMBER	2. GOVT ACCESSION NO.	3. RECIPIENT'S CATALOG NUMBER
4. TITLE (and Subtitle) Research in Materials		5. TYPE OF REPORT & PERIOD COVERED Final Technical 1 June 1973 - 31 May 1975
		6. PERFORMING ORG. REPORT NUMBER
7. AUTHOR(s) D.J. Epstein, C.G. Fonstad, Jr., H.P. Jenssen, A. Linz		8. CONTRACT OR GRANT NUMBER(s) DAHC 15-73-C-0317
9. PERFORMING ORGANIZATION NAME AND ADDRESS Massachusetts Institute of Technology Center for Materials Science and Engineering Cambridge, Mass. 02139		10. PROGRAM ELEMENT, PROJECT, TASK AREA & WORK UNIT NUMBERS 3D10
11. CONTROLLING OFFICE NAME AND ADDRESS Defense Supply Service-Washington Room ID 245-The Pentagon Washington, D.C. 20310		12. REPORT DATE 31 May 1975
		13. NUMBER OF PAGES 93
14. MONITORING AGENCY NAME & ADDRESS(If different from Controlling Office) ONR Resident Representative Massachusetts Institute of Technology Room E19-629 Cambridge, Mass. 02139		15. SECURITY CLASS. (of this report) Unclassified
		15a. DECLASSIFICATION/DOWNGRADING SCHEDULE

16. DISTRIBUTION STATEMENT (of this Report)

Unlimited

17. DISTRIBUTION STATEMENT (of the abstract entered in Block 20, if different from Report)

Unlimited

18. SUPPLEMENTARY NOTES

19. KEY WORDS (Continue on reverse side if necessary and identify by block number)

Integrated optics, hybrid optics, optically pumped lasers, rare earth lasers, miniaturized lasers, light emitting diodes, optical waveguides, optical modulators, crystal growth, liquid phase epitaxy, chemical vapor deposition, fluoride laser hosts, $LiYF_4$ (YLF), holmium laser, sensitized lasers, gallium arsenide, gallium arsenide antimonide, heterostructure diodes, (continued next page)

20. ABSTRACT (Continue on reverse side if necessary and identify by block number)

Major objectives of the research program were:(1) development of rare earth doped fluoride and oxide materials suitable for miniaturized, optically pumped lasers; (2) development of LED pumps for these lasers; (3) growth and evaluation of KTN thin films suitable for optical modulators. Although the research was materials based it was carried out in a context that recognized the interplay between materials development and device design.
We have obtained cw laser operation, at 77°K, of a Ho:αβYLF minilaser
(continued on reverse)

DD FORM 1473 1 JAN 73   EDITION OF 1 NOV 65 IS OBSOLETE
S/N 0102-014-6601 |

19) (CONTINUED)

potassium tantalate niobate (KTN), electrooptics,chemical purification techniques, solvent extraction, high purity crystals.

20) operating in an internal reflection mode 0.1 mm^3 dielectric cavity. Based on theoretical and experimental studies of energy transfer and upconversion processes a fluoride composition has been designed which should enable us to fabricate an LED pumped cw minilaser operating at room temperature.

We have fabricated GaAs:Si LEDs, matched to the 0.96 µm pump band of Yb^{3+}, which meet design objectives. A material system which should produce LEDs with narrower spectral emission is Ga(As,Sb):Si. Growth parameters for this system have been determined and some test LEDs have been built.

KTN films capable of guiding light have been grown by liquid phase epitaxy and have been used in fabricating an optical modulator having a drive voltage of about 8 volts for full modulation.

Special techniques for the synthesis of ultrapure feed materials for crystal growth have been developed.

END OF CONTRACT REPORT

Period: June 1, 1973 -- May 31, 1975

Title: Research in Materials Sciences

Project Title: Superconducting Transition Metal Alloys

Contract Number: DAHC 15-73-C-0316

ARPA Order Number: 2469

Program Code Number: 3D10

Name of Contractor: Massachusetts Institute of Technology
                       Cambridge, Mass.   02139

Principal Investigator: N.J. Grant (617) 253-5638

Project Scientists or Engineers: R.M. Rose (617) 253-3230

                                    M. L. A. MacVicar (617) 253-6261

                                    J.L. Bostock (617) 253-7607

Effective Date of Contract: June 1, 1973

Contract Expiration Date: May 31, 1975

Amount of Contract: $770,233

Amount of Project: $223,834

Sponsored By

Advanced Research Projects Agency

ARPA Order No. 2469

i

TABLE OF CONTENTS

VI. SUMMARY

This project has two main objectives: to unravel the complex problem of superconductivity of high T_c A15 materials by tunneling experiments and to develop materials for practical superconducting microwave cavities. The blueprint for this research is as follows: the digital hardware and software for processing of tunnel data is to be improved and expanded in capability; tunneling experiments on the surfaces of A15 compounds prepared in a planned manner will be performed; the feasibility of using various artificial barriers on the A15 substrates will be determined; and, relative microwave losses at X-band for a variety of materials and surface treatments will be determined by using a cavity with a removable back-plate. In this report we describe our progress towards these goals achieved in the first two years of this research.

(a) To extract the basic parameters for A15 superconductivity by tunneling techniques:

In the initial stages of the contract we were able to obtain good super-conductive tunneling into $Nb_3(AlGe)$ ribbon substrates and sputtered films. Although these A15 samples offer good flat surfaces for barrier formation and thus a high probability for successful tunneling, they were inhomogeneous and surface limited resulting in effective tunneling T_c's less than approximately 7K.

Arc melted $Nb_3(AlGe)$ buttons, fractured to reveal interior surfaces and subsequently mechanically or chemically polished, were also used as junction substrates. All of these A15 samples contained at least a small

percentage of second phase material and exhibited a fair amount of porosity. Their tunnel junctions were characterized by high leakage currents and large normal current backgrounds. The first derivative data which is reminiscent of deformed Nb tunneling data, is, therefore, extremely difficult to interpret. One or two of these junctions did, on the other hand, have reasonably good derivative curves consistent with energy gaps ~ 2mV. One arc melted Nb_3Al sample with an observable Al-depleted surface layer also exhibited a clean first derivative. The corresponding gap-ratio ($2\Delta/kT_c$) is ~ 3.2 which is very BCS-like. In the arc melted samples there is a definite improvement of tunneling characteristics with increasing perfection of the sample surface.

Tunneling into Nb_3Sn has also been achieved. The Nb_3Sn samples are obtained by diffusion of Sn into single crystals of Nb. Natural oxide barriers are then fabricated by oxypolishing the surface of these cylinders and subsequently immersing the specimens in an atmosphere of pure oxygen for 20 to 30 hours. Junctions fabricated in this manner are not only often of good quality but yield data which is reproducible from junction to junction. The barriers are also quite stable and able to withstand repeated recycling to room temperature. Typical energy gap values appear to be on the order of 3.6 mV which gives a gap ratio ~ 5.2. If our interpretation of the data is correct, this is the strongest coupled material that has ever been observed. Recently with the improvement of our tunneling characteristics we have been able to see the image of the lead counter-electrode phonon spectrum in the derivative curves; it is accompanied by other apparent phonon structure which we believe is due to the A15 substrate.

The tunneling data deconvolution software which extracts the phonon spectra and electronic density of states of unknown junction components has been implemented and debugged. These computer programs enable us to look at any combination of tunneling electrodes, even those with strong coupled superconductors on both sides of the barrier. (In the latter case, the phonon spectrum of one side must be known.) The programming has been used successfully to extract the phonon spectrum of Nb from both single crystal and deformed Nb junctions with three different counter-electrodes: Au, In, and Pb.

One implication of the above is that we can look, with greater precision than we thought possible, at more kinds of junctions than we thought possible. The initial success at tunnel junction fabrication on various kinds of A15 substrates and the improving tunnel characteristics with improved substrate surfaces indicate that the goal of this research is definitely feasible, and we continue to tackle the substrate surface problem with optimism.

(b) To develop appropriate artificial barriers for
A15 tunnel junction substrates:

A systematic study of the electronic behavior of arc-evaporated amorphous carbon films was completed. Rates of evaporation from 2 $\overset{\circ}{A}$/sec to 150 $\overset{\circ}{A}$/sec, vacuum pressures varying over three decades, and thicknesses of $\sim$50 $\overset{\circ}{A}$ to over 1000 $\overset{\circ}{A}$ were investigated. Resistivity was typically 1Ω-cm for films deposited at rates >10$\overset{\circ}{A}$/sec in 10^{-5} T vacuum at >100 $\overset{\circ}{A}$ thickness. A slower rate yielded markedly different, non-predictable resistivity values.

Electron microscope studies showed all as-grown films to be amorphous on a scale of $2\overset{\circ}{A}$. Temperature dependence of the resistivity was investigated over the range 4.2°K to 500°K; generally, log ρ followed a $T^{-\frac{1}{4}}$ behavior. Activation energies of the carbon film gap values at liquid helium temperatures were estimated as 3 to 5 meV. This range of values is sufficient as a barrier height betwen superconducting electrodes applied to the carbon films to form S-C-S' tunneling sandwich configurations.

Extensive investigation of electron-beam fabricated amorphous carbon films were also undertaken. In particular a general set of criteria for depositing usable carbon film barriers has been established in terms of deposition rate, film resistivity, and film color. These criteria seem generally applicable to both arc-evaporated and electron-beam fabricated carbon films. Superconductive tunneling was observed from a variety of different junctions with electron-beam evaporated amorphous carbon barriers: tin, indium, lead-impregnated porous glass, bulk $Nb_3(AlGe)$.

The implications of this study are that as long as sufficient care is taken in the carbon barrier fabrication (and, of course, that intermetallic compounds or diffusion layers do not form), these films can be used as insulating layers in junctions where the substrate oxidizes poorly or has conducting oxides. The major cases in point are V and the V-alloys, especially the A15 V-compounds V_3Si and V_3Au. Once the problems encountered in perfecting a representative surface in these materials have been overcome, carbon barriers will be needed to fabricate superconductive tunnel junctions.

(c) To develop improved surfaces, materials, and
surface treatments for superconducting microwave devices:

By using a Mo$_{.75}$Re$_{.25}$ alloy endplate on a Nb microwave cavity (TE$_{011}$ mode, resonant at 11.2 GHz), an upper bound for the residual surface resistance of this alloy was shown to be 2.8 μ-Ω and a lower bound for the breakdown field, 102 G. No particular effort was devoted to optimization of the surface quality of this backplate. Since the corresponding surface resistances at lower frequencies would therefore be well within the range required for practical devices, and the surface condition appeared to be much less critical than that of Nb, two cavities entirely of Mo-25Re were constructed. Preliminary tests were encouraging (residual unloaded Q's of 5 x 10^7 -1 X 10^9) but subsequent treating and testing suggest that alloy segregation (probably due to impurity contamination) and slowly-forming surface oxides may be degrading Q.

The Mo-Re cavities were delivered to us in June of 1974 and January of 1975 so that we are still in the preliminary stages of preparing and testing them. Thus, since the problems we are encountering are the main thrust of this aspect of our proposed research, we are neither surprised nor discouraged that, at this time, they are non-trivial. There are not, we believe, any long term implications in our present situation.

I.   INTRODUCTION

The original premise of this research is the vital importance of a funda-
mental understanding of transition metal superconductivity with a parti-
cular emphasis on compounds with the A15 crystal structure. The two
central goals are to determine the basic parameters governing the high
temperature superconductivity of A15 materials and to develop improved
surfaces, materials, and surface treatments which will make superconduct-
ing microwave cavities practicable.

Although many theories have been proposed, no one today understands why
A15 compounds form the class of highest transition temperature supercon-
ductors. Considering the impact that raising the maximum T_c to $\geqslant 25K*$
would have on the technology of generation, conversion, transmission, and
utilization of energy, it is important to find out the essential ingredients
for making high T_c materials. Many of the basic microscopic parameters of
the A15 compounds have yet to be determined: the pairing potential, the
density of states, the phonon spectrum, the energy gap, and any anisotropies
or anomalies in these parameters particularly as they relate to the
metallurgical history of the sample. Obtaining this data is necessary
before any effective use of the existing theoretical predictions for
increased T_c materials can be made.

The method of electron tunneling is a particularly powerful way of

---

*In the liquid neon range.

obtaining such information as long as the inherent surface and metal-
lurgical problems characteristic of these materials can be solved.
Sufficiently high quality tunneling data will enable us to extract
directly the electron-coupled phonon spectrum and all the other
microscopic parameters which are necessary for a description of A15
superconductivity in terms of strong coupling theory.

The other central goal of this research is to develop the technology
for the manufacture of practical superconducting microwave cavities and
similar devices. The application of superconductivity to microwave
technology (in particular, the S, L, and X bands) has demonstrated that
very large quantities of power may be handled with unprecedented effi-
ciency; in the X-band, quality factors in excess of 10^{11} have been
attained with frequency stability exceeding that of the best quartz
crystal systems. The only area where the potential advantages have been
extensively explored and calculated however, is in high energy physics,
where the use of superconducting microwave cavities affords a number of
striking technical advantages over the corresponding conventional devices,
most of them associated with the huge quality factors attainable (10^{11}
or more) and high rf fields (well above 1 kOe). The extreme stability
of such cavities has also made possible, for example, the development
of superconducting-cavity-stabilized microwave oscillators with remarkable
properties. There are undoubtedly many other potenial applications such
as high field rf plasma containment devices, but all such must await the
development of a reliable, economical fabrication technology, which can
consistently produce superior cavities whose properties will not degrade

with time or exposure to relatively benign atmospheres.

In the present research the experimental obstacles to obtaining detailed information on the surface and bulk properties of both the A15 compounds and other transition metal alloys are basically identical: one must prepare a smooth, clean surface, whose properties are representative of the interior of the superconductor, and on top of the surface, the thin oxide film which forms must be continuous, homogeneous, smooth and (at cryogenic temperatures) a reasonable insulator. On the other hand, the potential end results of the research are also non-trivial:

(1) substantial advancement of our understanding of superconductivity of the A15 compounds and the origins of high transition temperatures in these materials;

(2) new understanding of the nature of the surfaces of transition metal alloys and compounds;

(3) new and better methods for the manufacture of superconducting microwave devices.

In this report we discuss at some length the three different aspects of our research to date. The first section contains a description and analysis of the tunneling data we have obtained from various A15-substrate junctions (mainly having natural oxide barriers). The methods of surface preparation and barrier fabrication are extensively reviewed here. Nb_3Sn samples, made by diffusing Sn into a Nb single crystal are the most promising in terms of observing the phonon structures of both the A15 compound and the junction counter-electrode in the first derivative tunneling

curves. In this section we also report briefly on the progress made with the numerical analysis techniques for extracting phonon information from superconductive tunnel data. (This has been done in conjunction with another project, sponsored by ONR.)

The second section details our approach toward determining the connection between final tunneling barrier quality and the fabrication parameters of thin amorphous carbon films (e.g., deposition rate, thickness, pressure, and substrate species). The electronic behavior of arc-evaporated carbon films indicates that these films, acting as insulative layers in tunnel junctions, should have sufficient activations energies to make them useful barrier materials. The behavior of electron-beam deposited films as the barrier element in a metal-carbon-metal sandwich configuration for various substrate species is described in detail. General criteria for the successful fabrication of carbon barriers in tunnel junctions are discussed. These criteria establish rather narrow parameter limits outside of which some very undesirable effects from the point of view of superconductive tunneling come into play.

In the third and final section the progress we have made on the feasibility of using Mo-25Re in superconducting microwave devices is outlined. The initial trials using a Mo-Re back-plate on a solid Nb cavity which indicated that even without extensive preparation of the Mo-Re surface, this bcc alloy might well meet or surpass the standards required in X-band cavity work are reviewed. A complete discussion of the fabrication and testing parameters for two removable backplate cavities made entirely of Mo-Re is presented and the results of the characterization of our surfaces is

given. We believe that our present problems revolve about the continuous formation of oxides on the cavity surfaces as a function of sequential annealing for the various trails.

II. Tunneling into A15 Compounds

Attempts at tunneling into A15 compounds have thus far met with little
real success, due not only to metal processing difficulties, as in other
transition metal series, but to the capriciousness of the oxide barrier
fabrication. Beyond the requirement that the tunnel barrier must be
continuous, uniform, and insulating, an additional problem arises for
superconductors of extremely short coherence length: the interface
region (the transition region from barrier to bulk material) now constitutes
a significant fraction of the region sampled by the tunneling electrons,
even for interfaces which would ordinarily be considered quite sharp. In
fact, the surfaces of A15 compounds as prepared by current methods are
not sharp in any sense of the word, and, these alloys are known to have
very short coherence lengths.[1] Hence, extreme caution must be taken
in interpreting data from A15 junctions because it might reflect a surface
limited condition unless means are devised to ensure truly representative
properties near the surface.

Our approach to the actual tunneling into the A15 substrates is two-fold:
a careful procedural development of different barrier fabrication processes
on flat ribbons and sputtered films and (concurrently) an investigation
of the suitability of various bulk samples as junction substrates includ-
ing arc cast, annealed A15 button surfaces and diffusion layers of A15's
on Nb single crystals. Early in this investigation we obtained good
superconductive tunneling into the ribbon and film substrates with oxide
tunnel barriers fabricated either thermally or by a glow discharge
technique.[2] These junctions had a number of disadvantages: poor shelf

and cycling life, very low yield, and measured energy gap values well
below what would be expected from the measured bulk transition tempera-
ture, i.e., $\Delta(0) \sim .2 - .4 \, k_B T_c$. These problems were not unanticipated,
and the two main problems were easily isolated: the fabrication of sound,
stable tunneling barriers; and assuring that the layer of A15 substrate
within a coherence distance of the barrier is representative of the bulk
material. Structures related to both of these problems were readily
observed in the junction I-V characteristic and its derivatives.[2] Further
attempts to make these substrate surfaces more representative of the bulk
resulted in decidedly poorer tunneling characteristics for both types of
oxide barrier junctions.[3]

Subsequent investigations of the bulk A15 substrates indicated far more
encouraging results at the early stages of junction fabrication. First,
it appeared possible to remove the naturally occurring depleted surface
layers; then, although naturally occurring oxides were fragile and unable
to withstand either thermal or voltage cycling, various means of assisting
oxide growth resulted in increased durability; and, as the substrate
surface perfection increased, the tunneling data improved correspondingly.
For the latter reason we have concentrated our most recent efforts on the
bulk substrates: $Nb_3(AlGe)$ and Nb_3Sn.* We have made a systematic and
extensive exploration of the various means of natural oxidation of
their surfaces; e.g., thermal, glow discharge in oxygen partial pressures,

_____

*The Nb_3Sn substrates are generated by equilibration of a Nb single
crystal in a saturated Sn atmosphere.[4]

atmospheric, anodization, acid etching, and oxypolishing (or anodic stripping). Many of the above technqiues have resulted in identifiable superconducting tunnel characteristics, some even exhibiting phonon structure.

Although nearly ideal junctions will have to be obtained before phonon structure in the first derivative tunneling can be numerically processed, we are developing, in parallel, our phonon deconvolution programming. The results of this research may enable us to set-up guidelines and pro-cedures for judging the extent to which the tunneling in A15's reflects true bulk properties or only partially removed, disturbed surface layers.

(i) Previously Reported Research

Early in the course of these investigations[5] commercial-type Nb_3(AlGe) ribbons and rf sputtered films were chosen as substrate material since the existence and accessibility of flat surfaces in these geometries make them especially suitable for tunneling. The ribbons were fabricated by a process developed in this laboratory[6] and the films were sputtered from compacted and unreacted ribbon material.* X-ray diffraction and metallo-graphic studies showed more than 90% of each sample possessed the A15 structure. Whereas the transition temperature of the films was always <7K, the ribbon substrates had midpoint transitions of 17.5K which increased to 19K on low temperature annealing (725C for 90 hours in

---

*These films were supplied by the IBM Thomas J. Watson Research Center

less than 10^{-5} Torr).

Of the nearly 70 junctions tested only 2 showed nearly ideal first derivative traces and only 9 yielded typical (identifiable) superconductive tunnel data. These include both carbon barrier and oxide barrier junctions. On the whole there was little difference in the quality of the two kinds of junctions. In all of the successful samples the substrate was first cleaned with a chemical etch* to remove the outside layers of the ribbon and, consequently, any depleted or cold worked layers at the sample surface (and remaining cupronickel tubing contaminants on the ribbons). This was followed by glow discharge cleaning.** Barrier layers included oxide layers formed either by anodization in a glow discharge system without exposure to atmosphere (the sample is held at a few hundred volts above the cathode in 5×10^{-2} Torr O_2)[7] or by placing the samples in a free flow of oxygen at 150C (called a thermal oxide), and amorphous carbon barriers prepared either by arc evaporating $150\overset{\circ}{A}$ of carbon onto cleaned ribbon substrates or by electron beam depositing carbon films on both the $Nb_3(AlGe)$ ribbons and films.[1,5]

The results were not uniformly good: only two of these junctions had clear sharp gap structure and near ideal derivatives and even these had high excess currents. The rest showed either hysteresis or microshorts, overwhelming background currents, barrier-related structure, and/or

---

*10:20:30 parts (HF, HNO_3, lactic acid).

**The sample was maintained at a negative potential difference greater than 1000V in 30×10^{-3} Torr of Argon.

inconsistent gap structure superimposed on the desired characteristic.
In addition, all the junctions had fragile barriers that could not stand
up to either temperature recycling or sustained bias.[2,5] Our best
results were obtained with unannealed ribbon mounted as the anode in the
argon discharge and on which a thermal oxide barrier was subsequently
formed. The first derivative plot of one of these two junctions is shown
in Fig. (1). [The temperature of 2.6 K of the lower trace is only
approximate since the sample cooled by an additional 150 mK while the
derivative was being scanned.[2]] The value of 2Δ for $Nb_3(AlGe)$ obtained
from this junction is 0.7 meV at 4.2 K and 1.2 meV at 2.6 K. If the
energy gap followed the empirically desired temperature dependence,[8]
we would obtain $T_c = 4.6$ K and $2\Delta(0) \simeq 1.3$ meV. This yields a gap
ratio $(2\Delta/kT_c)$ of 3.3; i.e., these materials appear very BCS-like.
Interestingly enough the tunneling data from these and the other 7
successful junctions helped us to identify certain inhomogeneity problems
in the manufacture of the commercial ribbon substrates,[2,5] which later
enabled us to improve our arc cast $Nb_3(AlGe)$ samples; and, of course,
indicated clearly that our ribbon and film substrates were still surface
limited.

Further work on improving the substrate surfaces to make them more
representative of the bulk resulted in even poorer tunnel barriers,
especially the oxide types. Having established, however, at least guidelines
for the fabrication parameters of A15 tunnel junctions and realizing that
the ribbon substrates, in particular, would always be surface limited
because of the conflicting needs of commercial tapes[6] and tunnel substrate

Sample AB

$$\frac{d\,I}{d\,V} \text{ vs. } V$$

T = 4.2°K

T = 2.6°K
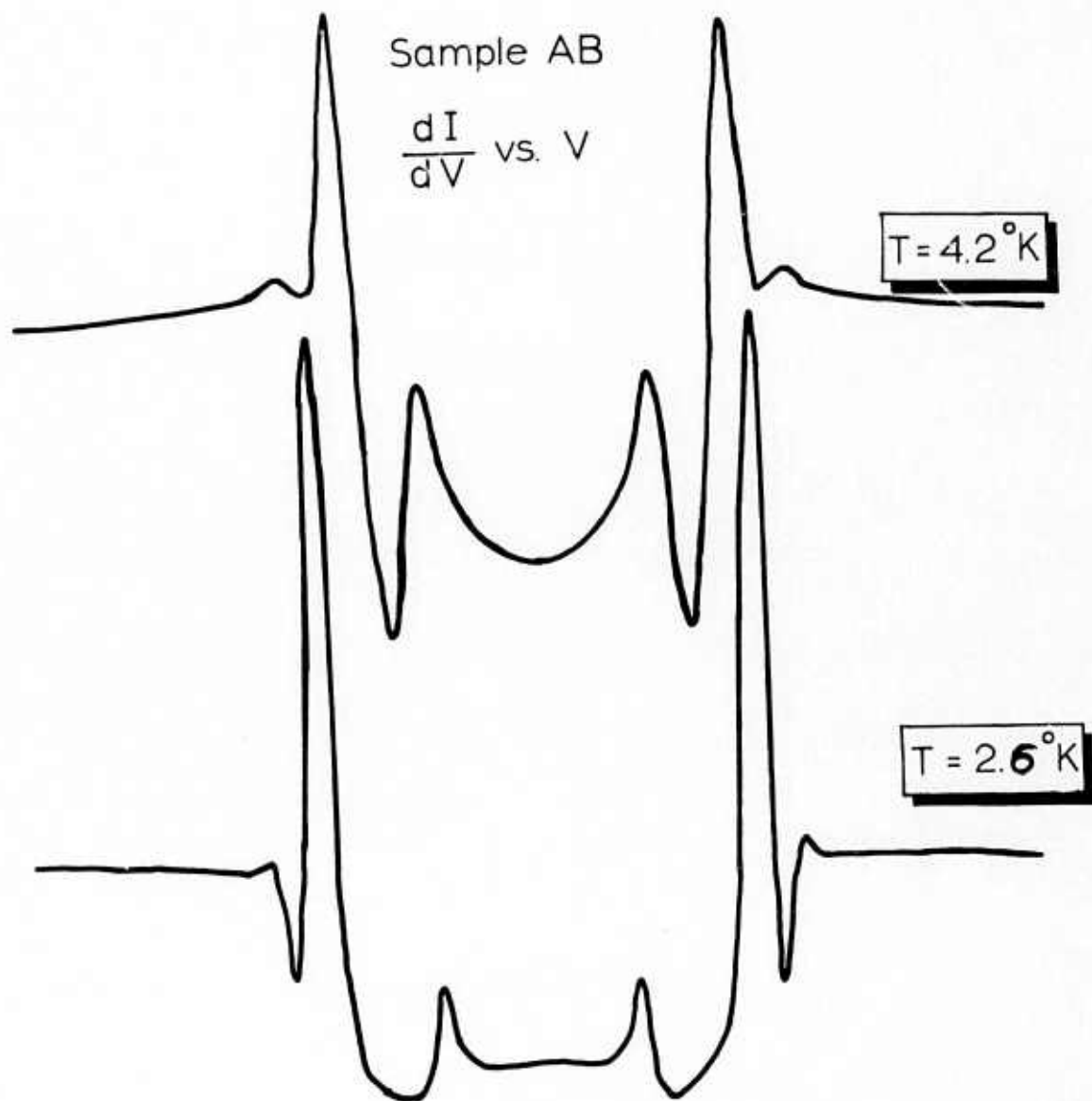
FIGURE 1. CONDUCTANCE CHARACTERISTICS OF RIBBON SUBSTRATE, THERMAL OXIDE BARRIER $Nb_3(AlGe)$ $-Pb_7Bi_3$. JUNCTION RESISTANCE AT 4.2 K WAS 270 Ω.

material, the emphasis of this research was placed on obtaining good
bulk substrate junctions.

(ii) Current Research

At the very beginning of the research effort on A15 materials, we attempted
to make V_3Au tunnel junctions using arc melted V-Au buttons.[3] Although
the buttons were, themselves, homogeneous and better than 90% A15, the
problems of deformed surface layers, exterior surfaces not characteristic
of the bulk, enormous surface roughness due to their brittle nature, and
the inability of the V-alloy systems to oxidize even primitively caused
us to focus our attention on preparing bulk substrates using the Nb-based
A15 alloys. The combined problems of attempting to perfect the A15 sur-
faces (with respect to both A15 composition and exposing smooth interior
planes for the tunnel barrier) at the same time as the methods for fabri-
cating artificial barriers on A15 substrates were being developed would
result in too many possible causes for tunnel junction failure. On the
other hand, besides the fact that the highest known T_c A15 compounds are
Nb-based [Nb_3Ge, Nb_3Ga, $Nb_3(AlGe)$, Nb_3Al, and Nb_3Sn], it is well known
that Nb and its alloys oxidize well. Thus, by switching to Nb-based
arc melted A15's we were able to concentrate on the problem of perfecting
substrate surfaces, and in a parallel effort worry about developing the
art of artificial barrier fabrication (section III of this report).
In addition, other research (ONR and AROD supported) in this laboratory
was, and is, centered on understanding the superconductivity of Nb itself,

in the single crystal, polycrystalline, and deformed or cold worked states. The changes which occur in the Nb tunnel junction data as a function of surface deformation should certainly be helpful in determining to what extent our A15 data represents disturbed surface layer tunneling as opposed to true bulk tunneling

Three different bulk substrate materials have been investigated: $Nb_3(AlGe)$ and Nb_3Al which are fabricated using conventional arc melting techniques[9,10] and Nb_3Sn prepared by diffusion of Sn atoms into a Nb substrate.[4] The $Nb_3(AlGe)$ and Nb_3Al samples are fabricated by arc melting stiochiometric powders of the appropriate starting materials (to which an extra 2% by weight of Al has been added) after they have been compacted in a steel die at 36,000 psi. The pressed powders are then melted and mixed such that the sample is turned at least six times while in the melter until the weight loss of the starting preparation corresponds to the desired composition of the final ingot (typically 4 grams in weight). Because of the preferential Al evaporation at these temperatures, it is assumed that the total weight loss is due to Al depletion. We have found that the more mixing and melting that can be achieved with decreasing Al evaporation, the more perfect the samples. The ingots are then subject to a homogenization anneal for 2 hours at 1840 $\pm$ 30C; and the buttons are then quenched to room temperature. The faster this quenching, the less second phase (σ-phase) material present in the final samples. For the $Nb_3(AlGe)$ samples a second low temperature anneal at 725-750 C (10^{-5} torr) increased the mid-point T_c from 17.5-18.5 to a maximum of 18.8 K; for Nb_3Al, to approximately 18 K.

After the anneal, the sample is ground down and cleaved under plane strain conditions to obtain clean, minimally deformed interior surfaces on which to fabricate a tunnel junction.* Finally, the resulting buttons are etched with 10:5:3 (HNO_3, HF, lactic acid) solution for 1/2 minute or anodized in ammonia to determine what phases are present.

Polishing, controlled etching, and electropolishing showed a small amount of second phase (5-10%) in all arc cast samples via the preferential etching and pitting of their surfaces. The etch pit patterns are reminiscent of dislocation site arrays often seen in other transition metal alloys.** In Fig. 2 are shown two typical photomicrographs of the Nb_3(AlGe) samples used in this study. The top picture corresponds to some of our earlier samples which had high porosity and a certain amount of non-A15 phase material; over time (Fig. 2b) we have reduced the porosity but not the 5-10% second phase in these samples (this is probably non-equilibrium Nb or Nb_2Al). Although not shown, the early samples also had wide, clear A15 regions toward the edges of the buttons. We have, therefore, managed to better homogenize our samples by making more uniform

---

*In this procedure the starting ingot is ground to have parallel surfaces. The grinding starts with 600 grit SiC paper through 30μ, 3μ, 1μ, ¼μ diamond pastes, down to 0.6 and 0.06 alumina. (Total time is about 30 minutes.) The surface is then cleaned and rinsed in acetone and the sample cooled to 77K. After placing in a vise, the ingot is struck with a "chisel" perpendicular to the flat surfaces. The surfaces thus exposed are, we hope, more representative of the bulk.

**The question remains, is there a complicated dislocation substructure inherent in the brittle A15 material or are we inducing such a condition by our fracture technique?

FIGURE 2.
PHOTOMICROGRAPHS
OF NB₃(ALGE) ARC
CAST SAMPLES
(X500) SHOWING
POROSITY (BLACK)
AND LOW TEMPERA-
TURE SEGREGATES.

A. TOP:
TYPICAL
BUTTON SURF-
FACE OF EARLY
WORK.

B. BOTTOM:
TYPICAL
SURFACES OF
MORE RECENT
SAMPLES.

the Al depletion. This is also reinforced by the fact that there is less segregation of the phases in the later samples.

Figure 3 is a photomicrograph of the equivalent Nb_3Al samples. (It is only recently that we have fabricated any usable Nb_3Al substrates.) These buttons are 95% A15 phase with the sigma phase segregated in small volumes in the sample. This indicates that the coring, occuring during arc melting, has not been completely eliminated upon high temperature annealing. It should also be noted that these samples show a much higher porosity than the $Nb_3(AlGe)$ probably because the Ge suppresses the Al activity in the latter compound. However, the Ge samples tend to have much larger cavities ($\sim 1\mu$) than the Al and they are not so uniformly distributed across the sample surface, which is also true of the second phase component. It is, perhaps, these facts which explain why the tunneling into Nb_3Al is so superior to that in the $Nb_3(AlGe)$.

Several methods have been used to fabricate junction barriers on the bulk substrates, the particular one in any case depending on the nature of the surfaces: surface etching followed by glow discharge oxidation, controlled-chemical etching of barriers, oxypolishing (or anodic stripping) of the sample substrate; and finally, artificial barriers which includes flash evaporation of thin Al layers followed by complete layer oxidation, or use of semiconductor layers. All of these methods have resulted in identifiable superconducting tunnel characteristics. In combination, moreover, they have been even more successful. In the following we choose only to discuss the particular method which seemed best for a given substrate. So, for example, Al_2O_3 layers on $Nb_3(AlGe)$ resulted

FIGURE 3.
PHOTOMICROGRAPH OF ARC MELTED Nb_3Al (X500) SHOWING POROSITY (BLACK) AND SMALL AMOUNTS OF SEGREGATED σ PHASE.

in 0.3Ω junctions (but whose tunnel characteristics were no better than junctions with oxide barriers) will not be reported. Junctions were then completed by depositing a $10^{-6}\mu$ Pb film* on the barrier and attaching Au leads to the sandwich configuration with Ag paint. The tunneling area was typically $1/4 \times 4$ mm. As a final step the junction was coated with formvar to preserve it.

To date the most successful** barriers on samples obtained by sintering elemental powders have been formed by mechanically and/or chemically polishing*** the button surfaces before subjecting them to a glow discharge oxidation in 50μ of oxygen at ≈ 750 V for 15-30 minutes. Junctions made on "exterior" fractured surfaces were unstable with respect to temperature cycling and time, and often yielded data not inconsistent with a normal layer on the A15 surface despite the fact that the bulk T_c was 18 K or higher. Some few junctions had characteristics in which distinct structure belonging to Pb could be identified. Junctions made on "internal" A15 surfaces were far more stable and in a few cases exhibited ordinary tunneling structures: sum and difference peaks, multiparticle peaks, etc. We are encouraged by these results since, as previously discussed, these surfaces are characterized by etch pits,

---

*Earlier we used Pb-Bi stripes which can be difficult to fabricate.[11] We subsequently found that the counter electrode deposition is even more important than we thought[12] so we converted to Pb thin films which are both stable and easily controlled.

**That is, giving the largest non-shorted, non-linear characteristic junction yields.

***In a 1:4:5 (HF, HNO_3, H_2SO_4) electropolishing solution.

bubbles, and second phase contamination. This lack of uniformity and smoothness precludes, we feel, the fabrication of good tunnel junctions because the thickness of the barrier layer is then, in turn, non-uniform which will give rise to shorts and microbridges, both phenomena often observed in our samples.

A tunnel derivative characteristic of our best $Nb_3(AlGe)$ junctions is given in Fig. 4; it clearly represents S-I-S' tunneling although its shape is far from ideal. Other experiments on deformed Nb, in this laboratory* are the basis of our speculations on the positions of the A15 multiparticle peaks and the gap edge structure. Figure 5 shows the first derivative of an annealed polycrystalline Nb foil, which has, of course, ideal shape.[13] Figure 6 shows the change in tunneling characteristic when the foil is swaged and rolled to give a true strain of 9.3.** Both of the first derivaties shown in Fig. 6 seem to be typical of these highly deformed surfaces.[13] The comparison between Figs. 4 and 6 is obvious and leads us to believe that we still are tunneling into a highly deformed A15 surface. Other characteristics obtained on the Nb foils which map the change in sample conductance as a function of deformation from zero strain to 9.3 will be used to check our surface conditions as we continue to improve our $Nb_3(AlGe)$ samples.

For purposes of comparison we have also included a tunneling characteristic for Nb_3Al in Fig. 7. It has an ideal conductance shape with both gap

---
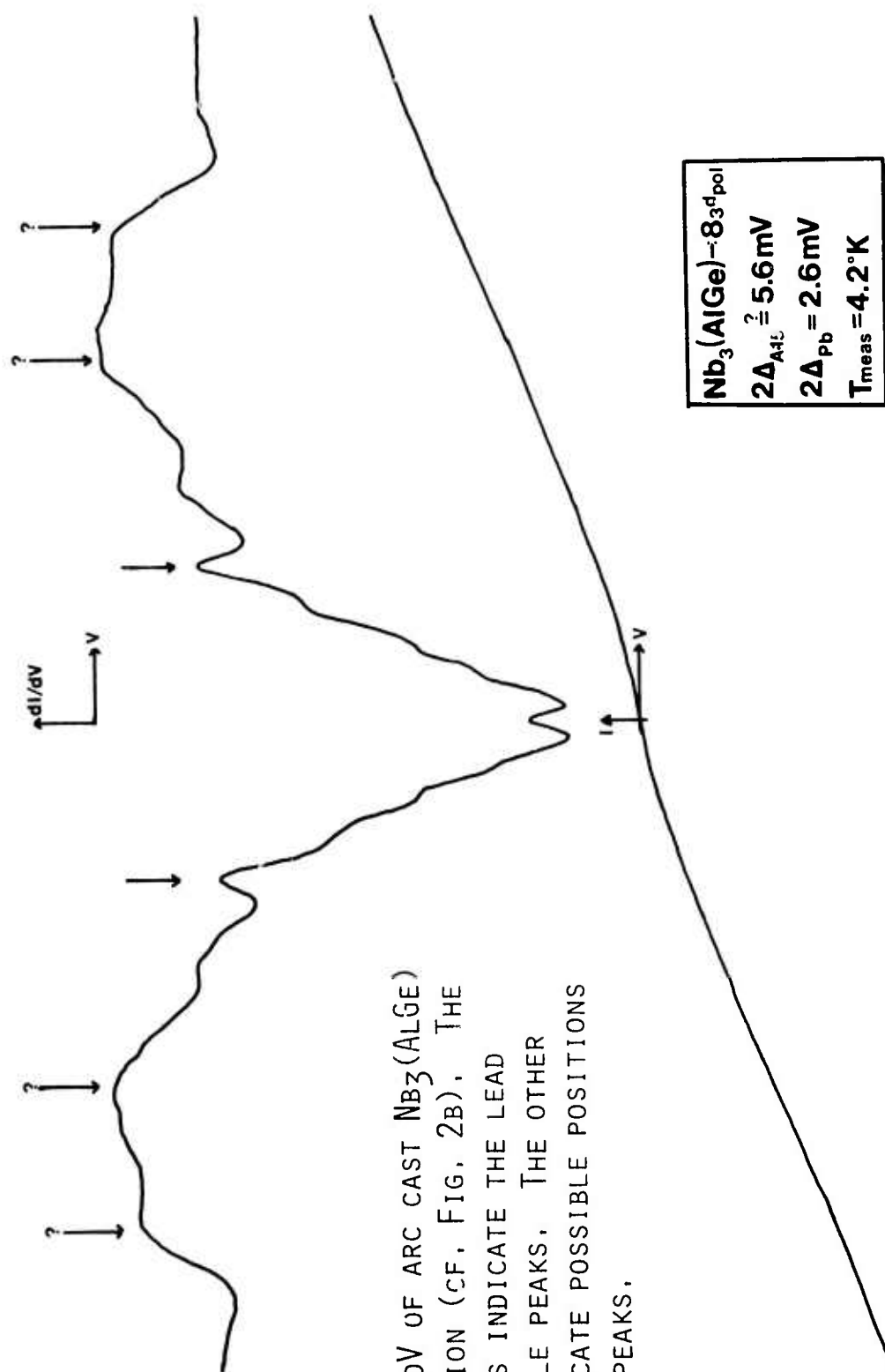
FIGURE 4.
I-V AND dI/dV OF ARC CAST Nb3(AlGe)
OXIDE JUNCTION (CF. FIG. 2B). THE
PLAIN ARROWS INDICATE THE LEAD
MULTIPARTICLE PEAKS. THE OTHER
ARROWS INDICATE POSSIBLE POSITIONS
OF SUM GAP PEAKS.

Nb₃(AlGe)−8₃ᵈₚₒₗ
$2\Delta_{AlC} \stackrel{?}{=} 5.6mV$
$2\Delta_{Pb} = 2.6mV$
$T_{meas} = 4.2°K$

FIGURE 5.
THE NEARLY IDEAL
FIRST DERIVATIVE
CURVE FOR AN
ANNEALED POLYCRYSTAL-
LINE NB-IN SAMPLE.
THE INSET CURVE IS A
MAGNIFICATION OF THE
LOW AMPLITUDE IMME-
DIATELY BELOW IT.
ARROWS INDICATE THE
MULTIPARTICLE PEAKS
FOR BOTH NB AND IN.

Nb polycrystal
Unstrained
$2\Delta_{Nb} = 2.95mV$
$2\Delta_{In} = 1.05mV$
$T_{meas} = .9°K$
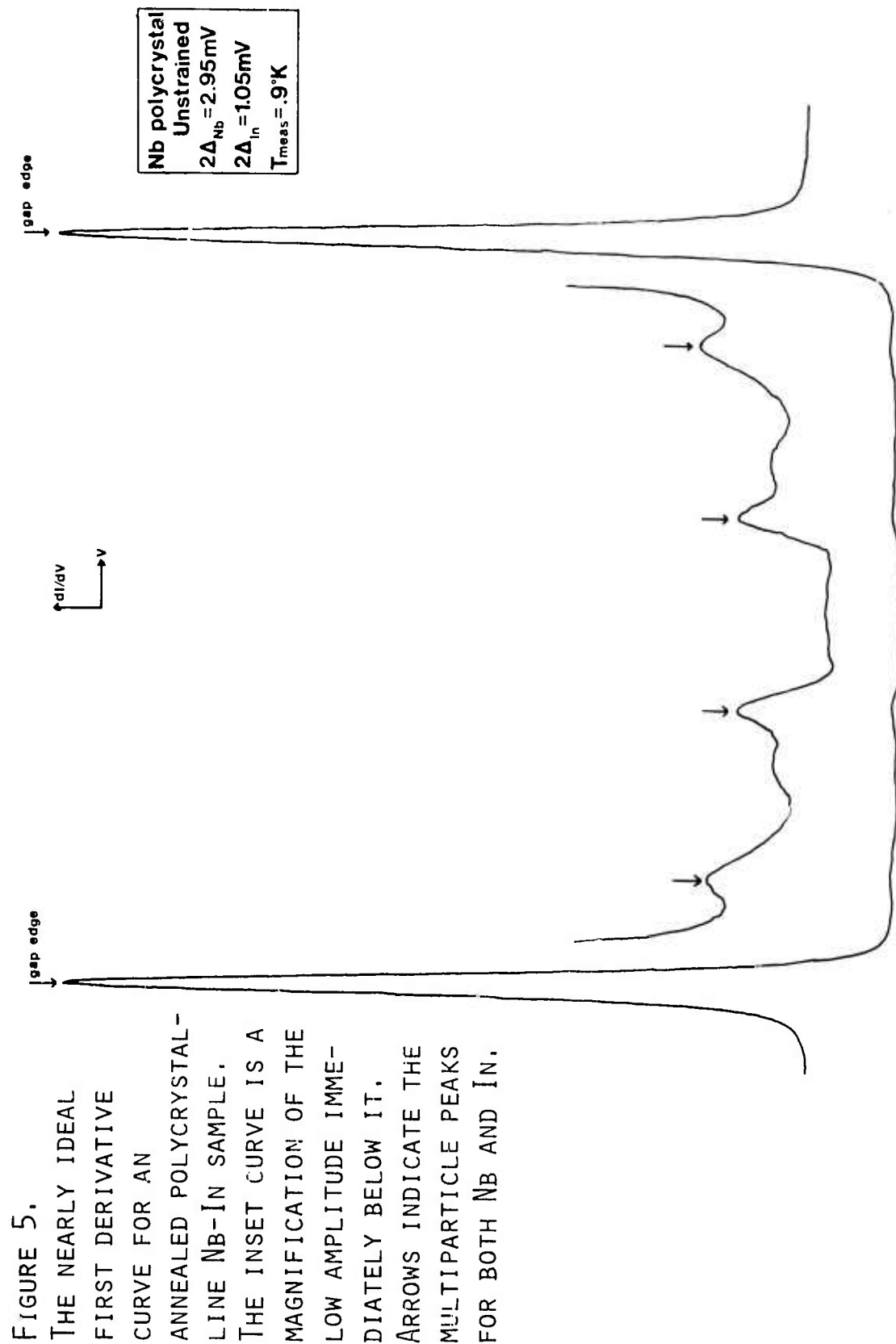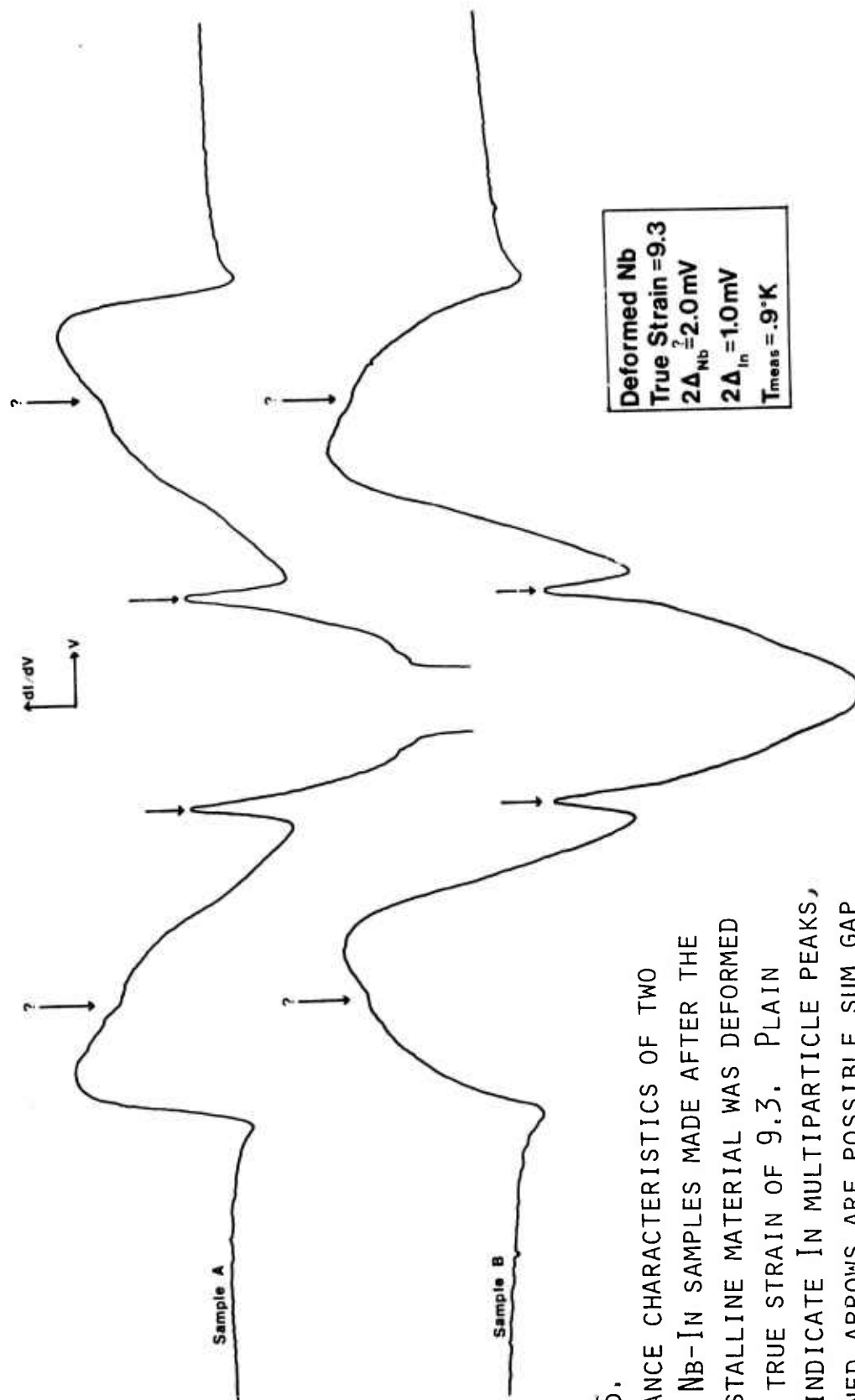
FIGURE 6.
CONDUCTANCE CHARACTERISTICS OF TWO
TYPICAL NB-IN SAMPLES MADE AFTER THE
POLYCRYSTALLINE MATERIAL WAS DEFORMED
UNDER A TRUE STRAIN OF 9.3. PLAIN
ARROWS INDICATE IN MULTIPARTICLE PEAKS,
QUESTIONED ARROWS ARE POSSIBLE SUM GAP
PEAKS.
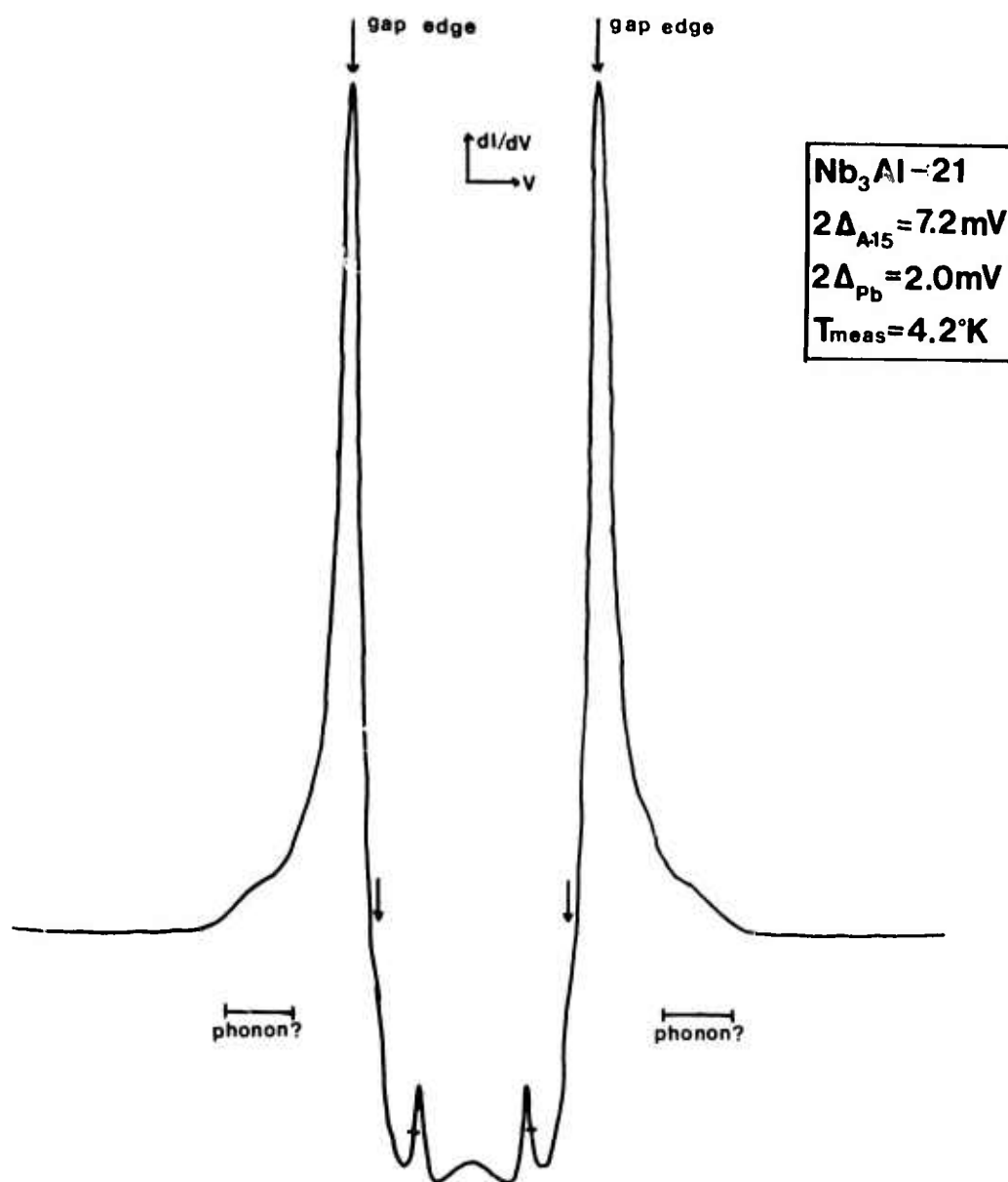
FIGURE 7.
FIRST DERIVATIVE CURVE OF ARC
MELTED Nb₃Al JUNCTION (SEE
FIG. 3) WITH Pb COUNTERELEC-
TRODE. ARROWS INDICATE
POSSIBLE A15 MULTIPARTICLE
PEAKS; THE BAR DENOTES THE
CUSP ON THE DIFFERENCE PEAK.

edge and difference peak. As can be seen, however, the low value of the A15 gap indicates that we are observing BCS-like behavior (i.e., $2\Delta/kT_c \sim 3.3$). Our previous experience with thin films and ribbons indicates that this tunneling also represents a surface limited condition so that, in fact, the effective T_c of the A15 <u>in</u> the tunnel junction is less than the bulk $T_c \sim 16$-17K. Experiments to determine this are in progress. On the other hand, the absence of the Pb multiparticle peak indicates that a good uniform tunnel barrier has been formed. Whether the latter is <u>due</u> to the lack of substrate surface perfection remains to be seen.

Recently a new technique[4] for preparing high quality, high T_c Nb_3Sn diffusion layers has been perfected by Siemens Laboratory for use in high Q superconducting microwave cavities. They report it results in very smooth homogeneous bulk-like A15 material, the smoothness depending on the surface roughness of the underlying Nb sample into which Sn atoms are diffused. We have adapted their procedures to obtain our Nb_3Sn substrates. We have not had time, however, to optimize our fabrication procedures. In order to obtain a clean smooth Nb starting surface, 1/8" Nb single crystal rods were grown in our ultra-high vacuum electron beam floating zone apparatus. This rod is then sealed in a quartz ampule with a saturated Sn atmosphere at 1000C for 20 hours. During this time Sn atoms diffuse into the niobium and then react to produce a Nb_3Sn layer several microns thick (up to $\sim 4\mu$). The reacted cylinders are then removed from the ampule and oxypolished up to 5 times (to 100V each time) to remove the outer non-stoichiometric surface layers of the

sample. After polishing they are rinsed in water and methanol and
dried in an evacuated desiccator. The T_c of such samples is 16.5K;
optimizing the fabrication parameters in the growth technique should
result in $T_c \gtrsim 18K$.

If the counter-electrode is deposited on these samples immediately after
oxypolishing the barriers obtained are unstable and noisy, if not shorted.
By backfilling the desiccator with an atmosphere of oxygen and allowing
the samples to oxidize for 20-30 hours, good stable junctions have been
obtained. To date we have tested 15 junctions: 8 were shorted, 2 had
strange structure as seen in the $Nb_3(AlGe)$ junctions, and 5 resulted
in the so-called Werthamer junctions.[14] Although the latter are thought
to be symptomatic of very thin non-uniform barriers layers, they are
interpretable and reproducible not only from junction to junction but
when the same junction is tested over a period of days. Junction resis-
tances range from 10 to 500 Ω. Unfortunately, the junctions still have
large background and leakage currents which obscure the structure at the
sum-gap bias so that the sum peak cannot be unequivocally identified,
and therefore, there is no conclusive evidence that our interpretation
of the observed tunneling structure is correct.

The first derivative curve of a typical junction is shown in Fig. 8.
The Pb double particle peak (dpp) appears at $\sim$1.4 mV with associated
multiparticle peak structure (mpp) at bias values of Δ_{Pb}/n where $n = 1,2,3,...$
Similarly, there is a peak at $\sim$3.6mV and corresponding structure at 3.6/n.
We have tentatively interpreted these features as the dpp and mpp of the
Nb_3Sn. This can only be verified if we can improve our junctions so that
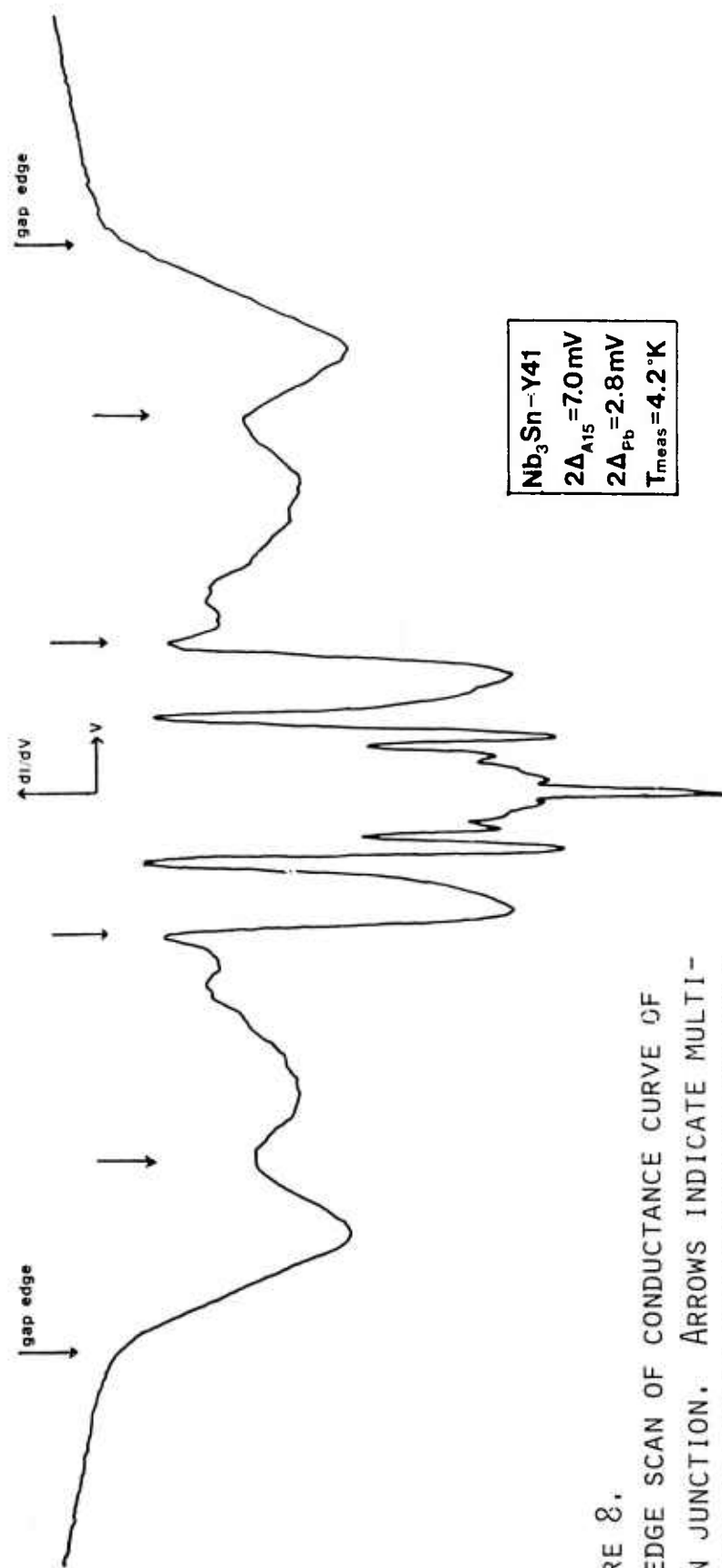
FIGURE 8.

GAP EDGE SCAN OF CONDUCTANCE CURVE OF
Nb$_3$Sn JUNCTION. ARROWS INDICATE MULTI-
PARTICLE PEAKS OF THE COUNTERELECTRODES.
ARROWS DENOTED AS "GAP EDGE" INDICATE THE
CALCULATED POSITIONS OF THE SUPPRESSED SUM GAP PEAKS.

the gap edge is visible on the derivative. With reference to the deformed niobium work and previous investigations in this laboratory on single crystal Nb-In junctions, the change in slope indicated by the "gap-edge arrow" in the figure should locate the sum gap peak. If this is correct, then $2\Delta/kT_c$ for these samples is 5.2 indicating extremely strong coupled superconductivity in these materials. Clearly, our next step will be to try to eliminate the background current so that the sum-peak can be observed, thus putting our interpretation on a firm basis.

In Fig.(9) a conductance scan of another of the Nb_3Sn junctions shows the characteristic phonon structure that should be present in superconducting Pb junctions. The first two peaks (measuring from the zero bias) have the proper position for Pb, the last structure may be one peak of the Nb_3Sn phonon spectrum. The relative ease with which these reacted layer substrates produce good junctions is extremely encouraging. We are attempting, at the present time, to improve the substrate surfaces in combination with exploring various other means to fabricate the oxide barriers on these surfaces.

DATA ANALYSIS*

Electron tunneling has come to be recognized as one of the most important techniques for studying the properties of metals in both the superconducting and normal metal states. In a tunnel junction if one (or both) of the metals is in the superconducting state at least four important properties

---

*This work was completed in conjunction with other ONR-supported research.
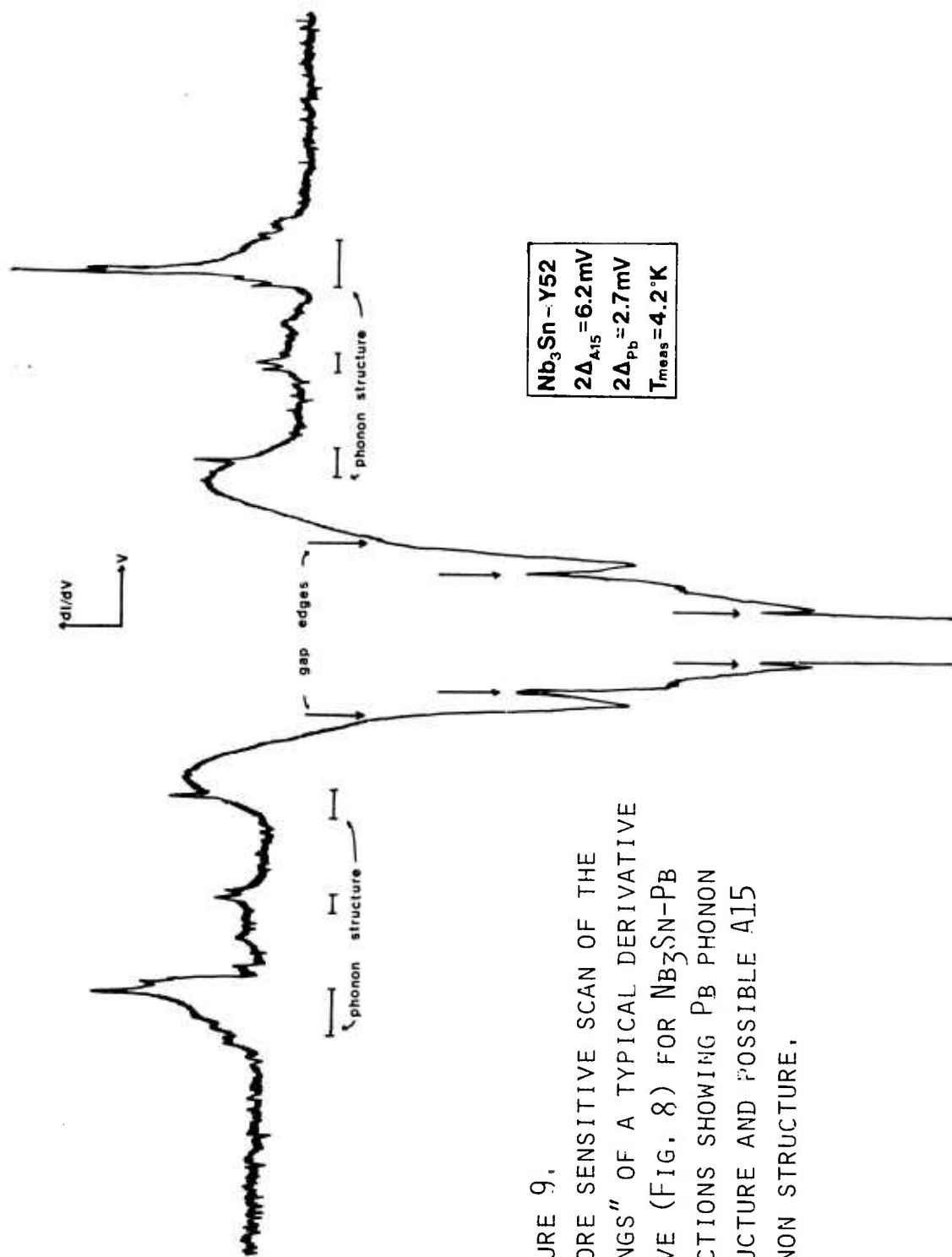
FIGURE 9.
A MORE SENSITIVE SCAN OF THE
"WINGS" OF A TYPICAL DERIVATIVE
CURVE (FIG. 8) FOR Nb_3Sn-Pb
JUNCTIONS SHOWING Pb PHONON
STRUCTURE AND POSSIBLE $A15$
PHONON STRUCTURE.

of the metal(s) can be determined from the first derivative characteris-
tic*:   the elctronic density of superconducting states N(E), the electron
coupled phonon spectrum $\alpha^2 F(\omega)$ [which is proportional to the phonon density
of states $F(\omega)$], the electron-phonon coupling constant λ, and the BCS
superconducting gap value Δ_o. Until recently, such experiments have
been limited to using a normal metal (or a BCS superconductor) as the
counterelectrode in tunnel junctions because of numerical difficulties
in interpreting data obtained from junctions having mixed strong coupling
superconductors as counterelectrodes. However, it is known that the
quality of the tunnel junction depends on the counterelectrode materials[12]
and, in particular, the best transition metal junctions are obtained
using other strong coupling superconductors as counterelectrodes. Although
the initial research in developing a method of data analysis for such
junctions, reported below, refers specifically to Nb, the potential
applications in tunneling experiments with A15's are obvious.

The difficulty in unraveling the tunneling data can be understood from
the following two considerations. First, the experimentally measured
current is**

$$I(V) \sim \int_{-\infty}^{\infty} N_1(E)\ N_2(E - eV)\ dE$$

---

*The conductance curve, dI/dV - V.

**The concepts involved in superconductive tunneling and a detailed
explanation of data deconvolution are given in both entries of Ref. (15)
and also in Refs. (16) and (17).

where V is the bias voltage and $N_i(E)$ is the density of states of a
given side of the junction as a function of the energy E. This means
that the first derivative, which contains the most accurate phonon infor-
mation is:

$$\frac{dI}{dV} \sim \frac{d}{dV} \int_{\Delta_1}^{V-\Delta_2} N_1(E) \, N_2(E - eV) \, dE$$

where Δ_i is the energy gap value of a given side of the junction. The
first job of the data analysis is thus to find the density of states,
say N_2, given N_1 of the known counterelectrode and the experimental $\frac{dI}{dV}$
data. (The gap values Δ_1 and Δ_2 can be read directly off the derivative
curve.[12]) The second task of the analysis is to relate this electronic
density of states to the phonon properties of the material.[15,16,17]
This is done by solving the Eliashberg equations for the superconducting
state.* However, these are integral equations expressing the complex
gap function $\Delta(E)$ in terms of a kernel which is itself dependent on the
gap function.

There are, clearly, a myriad of solutions to these equations and the
particular solution for a given material can be determined only when
appropriate boundary conditions are imposed on the solutions. In

---

*These are given on the next page: μ^* is the dimensionless Coulomb
pseudo-potential and the electron-phonon coupling constant

$$\lambda = 2 \int_0^{\omega_0} \left[\frac{\alpha^2 F(Eq)}{Eq} \right] \, dEq \quad .$$

Equations To Be Programmed

$$\phi(E) = \int_{\Delta_0}^{\omega_c} dE' \left[\text{Re} \frac{\Delta(E')}{\sqrt{E'^2 - [\Delta(E') \cdot \Delta(E')]}} \right] \{K_+(E',E) - \mu^*\}$$

$$\sum(E) = [1 - Z(E)]\, E = \int_{\Delta_0}^{\infty} dE' \left[\text{Re} \frac{E'}{\sqrt{E'^2 - [\Delta(E') \cdot \Delta(E')]}} \right] \{K_-(E',E)\}$$

where

$$K_{\pm}(E,E') = \sum_{pol.} \int_0^{\infty} dE_q\, [\alpha^2 F(E_q)]_{pol.} \left\{ \frac{1}{E'+E_q-i\delta+E} \pm \frac{1}{E'+E_q-i\delta-E} \right\}$$

$$Z(E) = 1 - \frac{\sum}{E} = 1 - \frac{1}{E} \int_{\Delta_0}^{\infty} dE'\, N(E')\, K_-(E',E)$$

$$N(E) = \text{Re} \frac{|E|}{\sqrt{E^2 - [\Delta(E) \cdot \Delta(E)]}}$$

$$\Delta(E) = \phi(E)/Z(E) = \Delta_R(E) + i\,\Delta_I(E)$$

such that $\Delta(E) \cdot \Delta(E)$ is a complex number,

$$\Delta(E) \cdot \Delta^*(E) = \Delta^2(E) = \Delta_R^2 + \Delta_I^2,$$

$$\Delta_R(E=\Delta_0) = \Delta_0\,(BCS-value)$$

$$\Delta_I(E=\Delta_0) = 0.$$

tunneling experiments it is possible to determine exactly the density of states of the material and the value of the gap edge $\Delta(\Delta_o) = \Delta_o$ directly from the experimental data. The final analysis stage associated with these experiments amounts to using these two constraints to determine the complex functions described by the Eliashberg equations (on a digital computer) and to obtain the electron-coupled phonon spectrum, $\alpha^2 F$, upon which these functions depend.

In essence the analysis can be divided into 3 separate parts or "STAGES". The first, Stage I, is a raw data processing step. It takes the lock-in amplifier output along with the DC bias as input data and determines the smoothed normalized conductance of the tunnel junction at a constant bias interval. STAGE II is concerned with the deconvolution of this conductance data to reflect only the density of states of the junction electrode being investigated; i.e., the normalized conductance and the density of states of the "known counterelectrode" are used to produce the electronic density of states of the unknown electrode as output. This output is used only for reference purposes in STAGE III. This final stage of the analysis consists of numerically solving the Eliashberg equation for $\Delta(E)$, $\alpha^2 F(\omega)$, λ, and μ^*. This is done by assuming various functional forms for $\alpha^2 F(\omega)$ and $\Delta(E)$ and interactively solving all of the equations to obtain self-consistency. After self-consistency for a given set of "guesses" Δ and $\alpha^2 F$ has been obtained, a density of states $[N(E)]$ is calculated from this solution. This calculated function is then compared

to the output of STAGE II, the so-called "experimental" density of states. The set of "guesses" for $\Delta(E)$ and $\alpha^2 F(\omega)$ which gives the "experimental" N(E) is the true solution to the Eliashberg equations for the particular metal in question.*

The initial programming for data analysis that we received[16] was capable of extracting electron-coupled phonon spectra from S-I-N junctions and, with some loss in precision, from strong coupled superconductor-BCS superconductor junctions. Major changes have been made in two of the 3 program stages. (1) The first modification is a program introduction comprised of all the software necessary to convert the output of the conventional tunneling electronics into absolute data characteristics. (2) The second stage has been extensively revised to allow the analysis of S-I-S' junctions with strong coupled superconductors on both sides of the barrier. The numerical accuracy of this stage has also been improved by more than an order of magnitude. The constraint of having only one unknown material in the junction remains, however.

Only minor modifications were necessary in STAGE III. After revising this program with improved numerical routines, the total double interactive procedures and convergence checks which were disabled susequent to the initial investigation of the Pb phonon spectrum were reimplemented. STAGE III is, thus, capable of deconvoluting phonon spectra to a self-consistency of better than one part in 10^4. Other, minor computer

---

*The sequence of guesses is NOT random but determined by a linear feedback routine which is based on how the calculated and experimental N(E)'s differ.[15,16,17]

routines necessary for preparing input to the main program (especially STAGE II) were also written and tested. The net result of these modifications is, we feel, an inversion routine which has greater accuracy and flexibility than the original programming, is more specific in the raw data handling techniques, and finally has a far wider range of applications than previously possible.

Single crystal Nb data has been used to determine the viability of the double deconvolution software.[17] First, we extracted the phonon spectra from Al-In and Al-Pb film junctions assuming Al is a BCS counterelectrode. The In results, determined from tunneling data taken at 1 K, compare extraordinarily well with spectra determined at .3 K. The Pb spectrum (also at 1 K) was far better than previously determined spectra from Al-Pb junctions, but not as good as those determined from Pb-Pb tunneling data. Three types of Nb junctions were analyzed: Nb-Au (Au is normal), Nb-In (In is an intermediate coupled material), and Nb-Pb (Pb is a strong coupled element). The spectra from all three types (11 junctions total) agree in all significant respects. A typical characteristic is shown in Fig. 10, Not only did the same shape result from all the spectra investigated, but this shape agrees with the phonon spectrum determined from neutron scattering.[18] This spectrum is shown in Fig. 11.

---

*The characteristic of these calculated spectra which differs most from the neutron scattering results involves the height of the longitudinal peak. As shown in the neutron scattering phonon spectrum, the longitudinal peak is always $\approx$ twice as high as the transverse peak. The best tunneling phonon spectrum ever obtained (Pb) has only equal height peaks,[16,17] This is thought to be due to the energy dependence of the electron coupling function $\alpha^2(\omega)$. Other conjectures are discussed in Ref. (17), pp. 127,143.
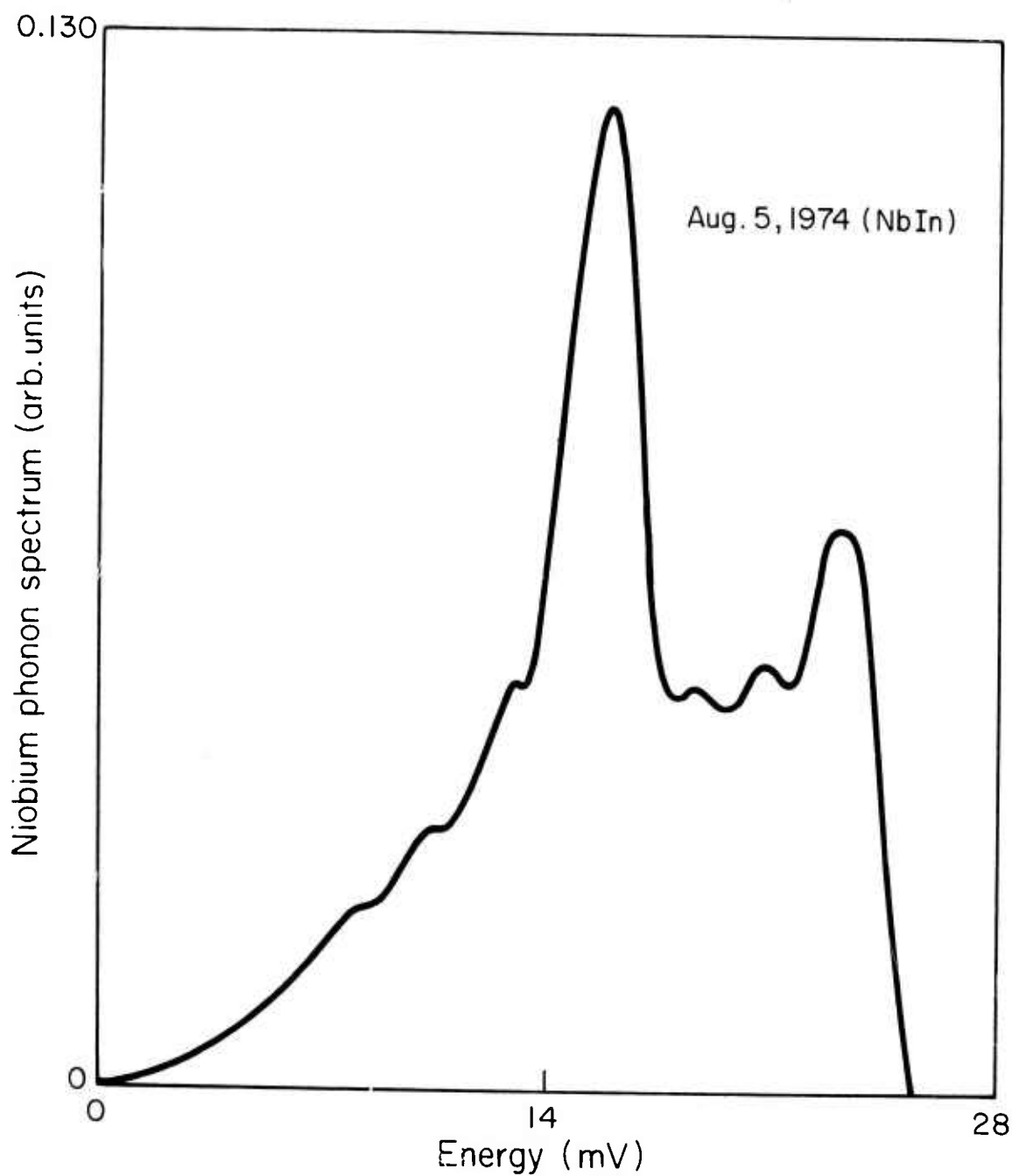
FIGURE 10. NB PHONON SPECTRUM DECONVOLUTED FROM A SINGLE
CRYSTAL NB-IN JUNCTION: RESISTIVITY RATIO OF
$N_B = 483$; $\mu^* = -.11$; $\lambda = .4$.

R.I.Sharp
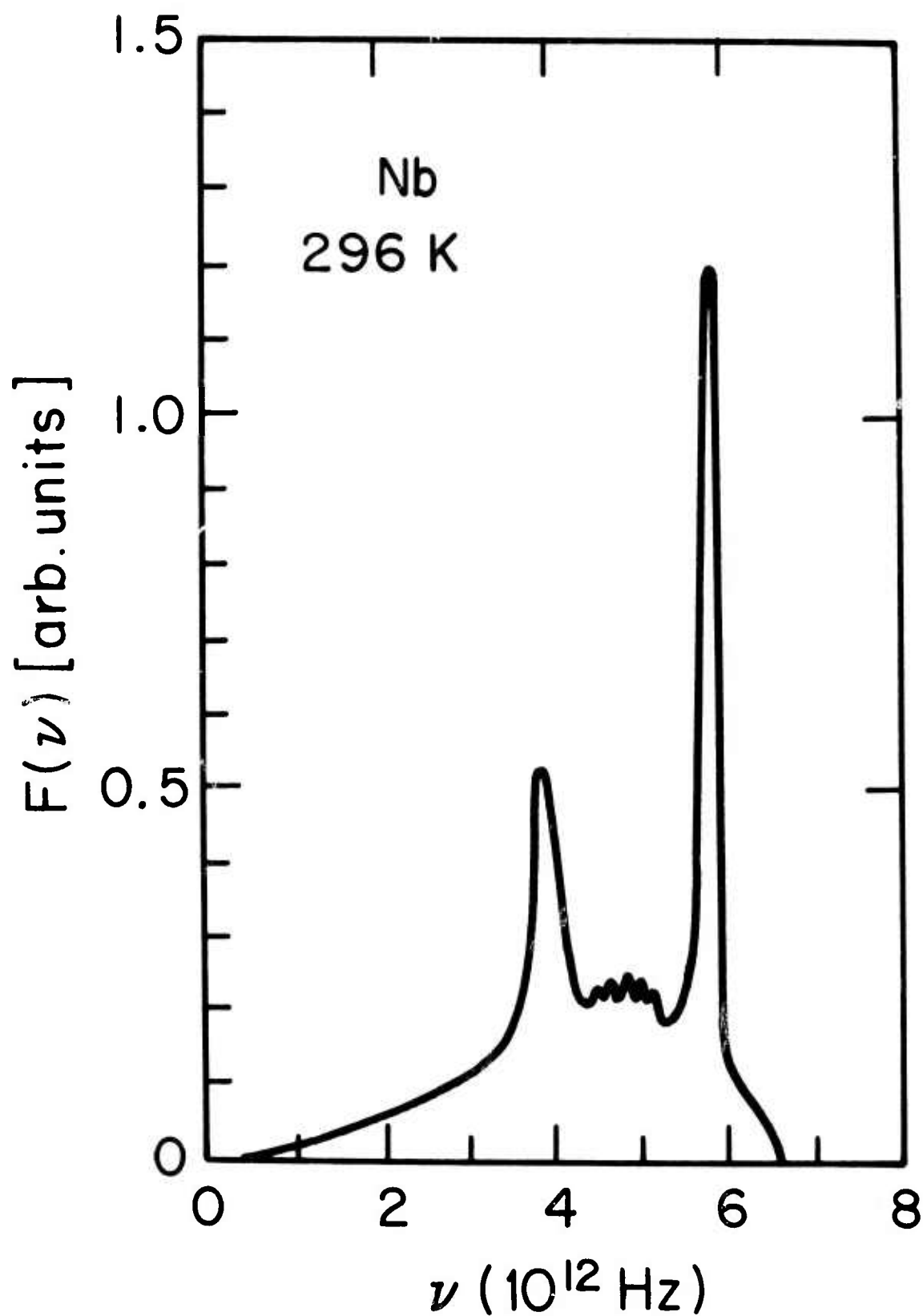
FIGURE 11. NB PHONON SPECTRUM AS CALCULATED FROM INELASTIC NEUTRON SCATTERING: R.I. SHARP, J. PHYS. C(SOL. ST.) 2 (L969) 421 AND 431.

In order to determine whether the deconvolution routines resulted in different α^2F's when the surfaces of the tunneling substrate were known to be dirty, impure, or deformed, we purposefully "contaminated" the single crystal Nb cylinders. In one case, holding all other fabrication parameters constant, the growth rate of the single crystal was doubled. The resulting crystal had visible rings around the crystal cylinder which probably are due to the uneven growth and segregation of the impurities in the melt into impurity bands. The α^2F function generated from this junction is shown in Fig. (12a). The first two peaks can be seen to have grown at the expense of the longitudinal peak at the end of the spectrum. A second Nb junction was made by strongly etching the surface of the single crystal with acid before the oxidation forming the barrier (all other fabrication parameters were held constant). The results obtained from that junction are shown in Fig. (12b). The main change from the junctions representative of the pure single crystal is seen in the splitting of the longitudinal peak and the increased shoulder structure between the peaks. These results do not agree with the neutron work and indicate that the computed α^2F is very sensitive to the conditions of the surface of the Nb single crystal. As a matter of interest it should also be noted that the first derivative scans from gap edge to gap edge were not that different for the three samples described; only their phonon characteristics were distinctly different.

There is, on the other hand, a disturbing discrepancy in the values of λ and μ^* computed from the single crystal Nb data: parameter values from different junctions did not compare well,[17] nor did any set of these values agree with theoretically accepted values. The most alarming

FIGURE 12. THE ELECTRON COUPLED PHONON SPECTRUM OF SINGLE CRYSTAL NB-I-IN JUNCTIONS:
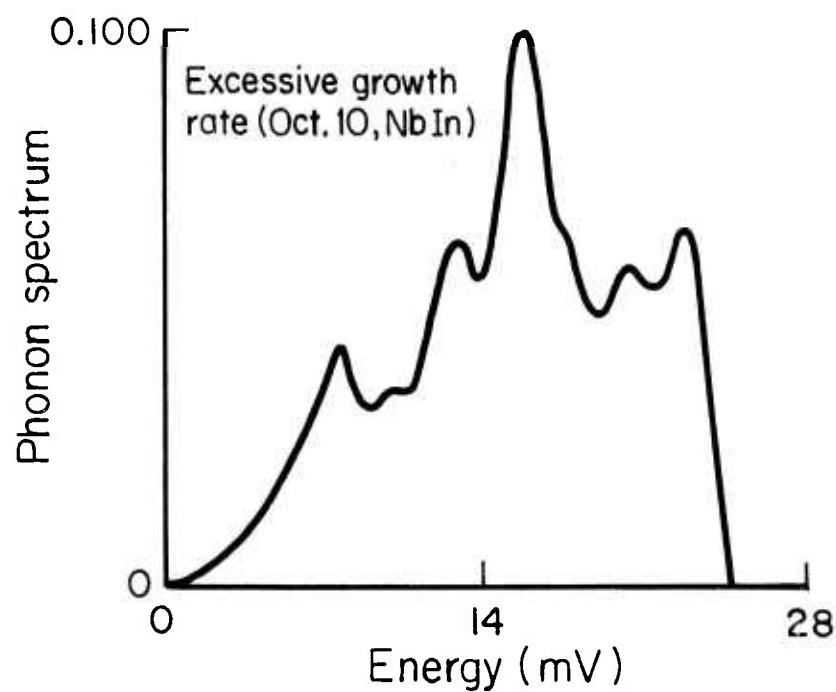
(A) NORMAL CRYSTAL GROWN RATE DOUBLED;
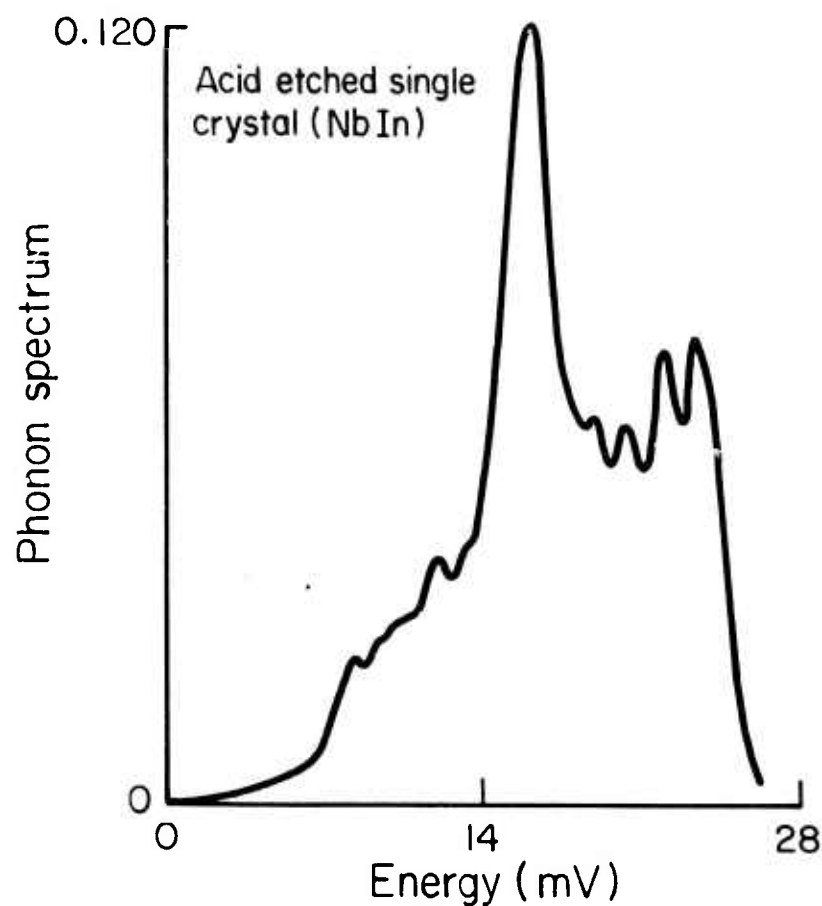
(B) NORMALLY GROWN CRYSTAL SUBJECT TO AN ACID ETCH BEFORE BARRIER FORMATION.

result is that all calculated values of μ^* are negative. In fact, a negative value of μ^* has no physical meaning within the Eliashberg theory of strong coupling superconductors since it represents the effective value of the Coulomb repulsions between the electrons. Such a value could mean, of course, that there exists some other positive electron interactions besides the electron-phonon interaction which has not been taken into account for transition metal compounds. (Or, perhaps, it is also possible that this effect is due to the very complicated Fermi surface and high density of d-electrons in Nb.)

On the other hand, the $\alpha^2 F$ spectrum obtained when μ^* is negative carries all the essential features of the neutron scattering data so that this possibility seems unlikely. And, most other studies NOT carried out on simple, isotropic s-p band materials have resulted in anomalously low (and even negative) values of μ^*. It is not, however, obvious what the difficulties are*; they might be experimental in nature, be an artifact of the numerical calculations, or be of a fundamental nature.

A number of "model" phonon spectra, based on both our work and the neutron scattering results, were devised for Nb in order to determine: exactly how the self-consistency routines would handle the convergence toward this spectrum, precisely what values of μ^* and λ would be characteristic of Nb given the ideal phonon shape, and whether the programming would discriminate against generating a negative μ^*. Although there is no preference in the programming for either positive or negative μ^*, the convergence for

---

*A detailed discussion of the possibilities can be found in Ref (17), pp 127-143.

negative values is far slower. Ideal Nb spectra can be generated with positive μ^* but then the values of λ are absurdly high.

As an external (rough!) check on the validity of such spectra, T_c was calculated using the commonly accepted approximations inherent in strong coupled superconductivity (and, thus, our programming):[19]*

$$T_c = \frac{<\omega>}{1.2} \exp \left[\frac{-(.04)(1 + \lambda)}{\lambda - \mu^* (1 + \frac{<\omega>}{\omega_0} \lambda)} \right] \quad .$$

Values of the parameters generated by our actual experimental data produced good agreement with the measured T_c values. The ideal phonon spectrum results were factors of 3/2 and more, higher than measured T_c's. A careful consideration of the basis of this equation, however, has convinced us that for a material with a very broad phonon spectrum, especially with phonon structure below 10 mV, accurate values of T_c can be produced only by a full self-consistent solution of the finite temperature Eliashberg equations.

---

*The first moment of the phonon spectrum $<\omega>$, is also generated by STAGE III.

(iii) Direction of Future Work

We plan to continue to improve the quality of our arc melted samples surfaces and to experiment with different methods for producing tough, durable oxides on these substrates. We will also continue to use a variety of other substrate sources such as films and reacted Nb cylinders The object is, of course, to obtain internally consistent, high quality tunneling data which can be used with the deconvolution software to extract the phonon spectra and strong coupling parameters characteristic of bulk A15's.

We have recently obtained the Nb_3Sn single crystal from the RCA Laboratory in New Jersey. When we feel we have optimized our barrier oxidation techniques we will use the data from this crystal in a comparison with our reacted Nb_3Sn cylinders to determine the quality of our surface layers and to determine differences in their phonon spectra.

We have already begun to investigate the possibility of developing a reacted Nb_3Al cylinder by encapsulating a Nb single crystal and Al vapor in a constant volume Nb shell. Since this method is based on the same principles as those involved in reacting Nb with Sn vapor, we believe we can produce bulk-like surfaces of ordered Nb-Al A15 with a surface composition varying between 19 and 28 atomic percent. At present, liquid metal corrosion of the Nb container limits the treatment time possible for reacting the sample, better temperature control in the process is needed, and the geometry must be redesigned so there is a uniform diffusion of Al into the Nb single crystal.

Since it is highly probable that the deconvolution of the A15 materials
will be done with 4 K tunneling data, we are presently programming the
finite temperature Eliashberg equations of superconductivity. At the
same time we are attempting, experimentally, to fabricate and deconvolute
superconducting In-Pb junctions to determine the ultimate capabilities
of the double deconvolution routines for zero temperature. This is
necessary because there is no way of knowing if the phonon spectra of Pb and
some particular A15 compound entirely overlap, as do the spectra of Pb
and In (whereas that of Pb and Nb, e.g., do not). In addition, we are
continuing our study of the effects of "model spectra" in the equations
of superconductivity which appears to be necessary if the recently obtained
experimental results on La, single crystal and deformed Nb, and Nb_3Sn are
to be explained.

III. Artificial Barriers for Superconductive Tunneling

Fabrication of satisfactory tunneling barriers on A15 metal substrates is central to the success of a detailed tunneling investigation of the microscopic superconducting parameters associated with high transition temperature materials. Although the development of suitable barrier fabrication technology is difficult for almost any substrate material, the A15's present a particularly severe challenge. Our approach has been two-fold in its emphasis. We have systematically pursued the more conventional avenues of surface oxidation, and at the same time we have made a significant laboratory commitment to the development of non-substrate oxide (or artificial) tunneling barriers. Such barriers can sometimes be made more rugged, thicker, and more insulative than the natural oxides of a particular material[1] (e.g., rhenium). Examples of kinds of artificial barriers that have been used by researchers are barium stearate layers,[2] thin films of semiconducting materials,[3] and very thin layers of completely oxidized aluminum.[4]

We have focused on amorphous carbon as a promising barrier candidate.[5] Unlike many semiconductor compounds and certain simple elements, carbon is metallurgically well behaved on most substrates of interest. Past experience in our own laboratory[1,5,6] and subsequent efforts in other laboratories[7,8] has shown that 100-300Å layers of amorphous carbon can form usable junction barriers on simple substrate metals such as Cu, Sn and Pb films, on a smooth-surfaced recalcitrant oxidizers such as rhenium single crystals, and on exotic materials such as Nb_2Se.

The goals of our current carbon work are: to determine the effects of film aging, resistivity, fabrication method, substrate cooling during deposition, thickness, and substrate species on observed barrier performance; to determine an optimal approach for barrier fabrication on A15 substrates of interest by establishing the capabilities of carbon barriers on substrates of various personalities, and to apply the technique of amorphous carbon barriers to A15 materials themselves. We have fabricated both arc-evaporated and electron-beam deposited carbon films as cryogenic tunnel barrier layers. In the case of arc-evaporated carbon films extensive investigation of the relation of fabrication to observed electronic properties of isolated carbon films was also made. The study included high temperature annealing treatments and microstructural examination.

(i) Previously Reported Results

Seventy-five isolated films of arc-evaporated carbon were fabricated on room temperature glass substrates at rates varying from 2 $Å/sec$ to 150 $Å/sec$ and pressures varying from 5×10^{-3} Torr to 5×10^{-5} Torr.[9] Final thicknesses of the films ranged from 50 $Å$ to 1600 $Å$. Resistivity along the length of the films was investigated over the temperature range of 4.2 to 500 K.

Resistivity was independent of deposition rate for films of thicknesses greater than 100 $Å$ and deposited at rates in excess of 10 $Å/sec$. Typically, resistivity was observed to be about .4 to 4 Ω-cm and could be fabricated with 83% reproducibility for this resistivity range in a moderate vacuum of 5×10^{-5} Torr. Deposition rates slower than 10 $Å/sec$ resulted in a wide

variation in film resistivities, ranging over six orders of magnitude (10^1 Ω-cm to 10^7 Ω-cm). Poorer vacuum increased the observed range of variance (10^{-1} Ω-cm to 10^7 Ω-cm). For a given deposition rate, an order of magnitude increase in vacuum pressure yielded approximately an order of magnitude increase in film resistivity.

For heating temperatures up to 500 K, hysteresis was observed in resistivity-vs-temperature curves for the first few room temperature to room temperature heating/cooling cycles; then it disappeared. Room temperature resistivity dropped approximately a factor of 10 after the first heating/cooling cycle. There is some suggestion in the literature that the hysteresis is the result of a microstructural temperature dependence in the ratio of diamond-like regions to graphite-like regions comprising the film.[10] Since we did not see hysteresis effects for heating/cooling cycles involving cryogenic temperature and room temperature, this suggestion does not seem applicable. We believe that the higher temperature hysteresis effects are more likely due to changes in the background level of conduction-contributing impurities and defects in the carbon films.

Furthermore, the microstructural information we obtained on our samples by TEM showed them to be extraordinarily amorphous: the "as grown" films were structurally disordered (i.e. amorphous) on a scale of 2 $\overset{\circ}{A}$ resolution. Further, the films remained disordered after a heating/cooling cycle. Resistivity, although influenced by impurities as evidenced by the pressure dependence noted, showed no apparent microstructural sensitivity over the temperature range investigated.

(ii) Current Research

An additional twenty-eight carbon films have recently been fabricated by
arc-evaporation. These films were sandwiched as tunneling barrier layers
between substrate electrodes of In, Al, Au, and Sn thin films and both
Nb_3(AlGe) bulk films with counterelectrodes of In, Al, Sn, and PbBi thin
films.[11] Data measured <u>along</u> the <u>isolated</u> carbon films discussed above
agrees well with measurements done <u>through</u> the <u>sandwiched</u> carbon films.
For example, the same wide range of resistivities was also observed through
sandwiched carbon layers as along isolated carbon films. The value of
10 Å/sec in deposition rate again appeared as a critical value; the most
promising barriers occurred when the deposition rate was of this magnitude.
Slower rates gave higher resistivities, sometimes even greater than our
tunneling data instrumentation could handle.

Unlike the case of isolated carbon films, the reproducibility of resistivity
values of sandwiched carbon films deposited at 10 Å/sec was poor.* The
general behavior of these resistivities was to vary inversely with deposition
rate. However, the observed behavior of arc-evaporated carbon films cannot
be predicted well enough or the arc-evaporation deposition techniques
sufficiently controlled to provide the kind of everyday, dependable fabrica-
tion technique needed in reasonably large-scale and difficult tunneling
experiments such as we are pursuing on A15 superconductors. Therefore,
electron-beam deposition, because of its capacity for tighter control of

---

*The arc-evaporation gun design was probably the cause of this;
control of barrier layer thicknesses was erratic.

deposition rate and vacuum pressure, by reducing the heat which causes system outgassing, looked like a better technique.

Thirty-eight sandwich samples of electron-beam deposited carbon films were fabricated in $\overset{\sim}{<}2.5 \times 10^{-5}$ Torr vacuum; eleven junctions exhibited indentifiable tunneling characteristics of a quality suitable for a detailed superconducting tunneling investigation.[11] Superconducting tunneling structure was unambiguous in the cases of substrate electrodes of indium and tin films (see Fig. 13) and bulk lead-impregnated porous glass (see Fig. 14). Table I summarizes information on these eleven junctions.

Tin substrate junctions were prepared with both arc-evaporated and electron-beam deposited carbon film barriers. Only those junctions fabricated by the electron-beam technique were successful. Figure 13 shows an I-V characteristic for a Sn-C-Sn junction of carbon thickness 100 $\mathring{A}$ deposited at 11.1 $\mathring{A}$/sec. The sum gap, $2\Delta_{Sn}$, is readily visible at a bias of 1.21 mV. The background curvature in the characteristic is commonly seen when junction barrier heights are less than those of natural oxides. Engineering of the barrier height, and thus controlling the degree of curvature-dependent excess current so it does not interfere with phonon deconvolution, is essential.

Activation energies in the carbon were crudely estimated from tangents to $\ln \rho$ vs $\frac{1}{T}$ data on comparably prepared, isolated arc-evaporated films.[9] Typically, these values are 50 mV at room temperature and 3 mV at 5 K, indicating an ill-defined activation energy for such films. $\ln \rho$ vs $T^{-\frac{1}{4}}$ was observed to be linear; in keeping with the amorphous nature of the films.

TABLE 1

SUCCESSFUL ELECTRON-BEAM CARBON BARRIERS

Substrate	Counter-Electrode	Carbon Deposition Rate Angstroms/sec	Carbon Thickness Angstroms	Room Temp Junction Resistivity Ohm-cm	Liquid Helium Junction Resistivity Ohm-cm
Indium	Indium	0.9	52	6.25×10^4	1.90×10^7
Tin	Tin	5.4	130	$<10^2$	3.38×10^8
Tin	Tin	5.4	130	$<10^2$	4.79×10^9
Tin	Aluminum	5.4	130	$<10^2$	3.65×10^8
Tin	Aluminum	5.4	130	$<10^2$	3.38×10^8
Indium	Tin	11.3	270	$<10^2$	2.75×10^9
Tin	Tin	11.1	100	$<10^2$	4.04×10^5
Tin	Tin	11.1	100	$<10^2$	1.38×10^6
Tin	Tin	11.1	100	$<10^2$	5.39×10^6
Tin	Indium	11.1	100	$<10^2$	1.74×10^6
Lead-Impregnated Porous Glass	Aluminum	6.4	95	2.32×10^7	1.22×10^8
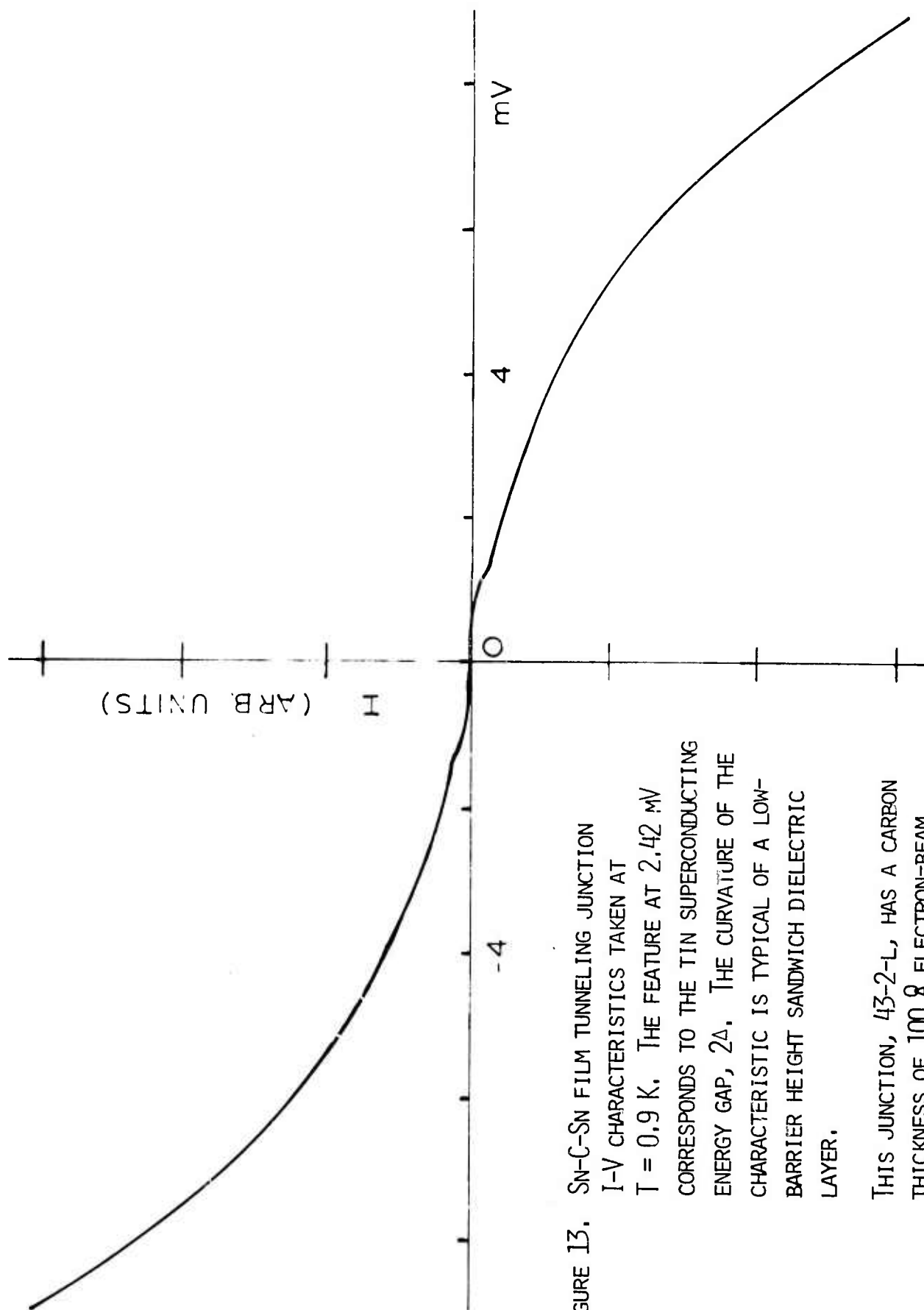
FIGURE 13. SN-C-SN FILM TUNNELING JUNCTION I-V CHARACTERISTICS TAKEN AT T = 0.9 K. THE FEATURE AT 2.42 MV CORRESPONDS TO THE TIN SUPERCONDUCTING ENERGY GAP, 2Δ. THE CURVATURE OF THE CHARACTERISTIC IS TYPICAL OF A LOW-BARRIER HEIGHT SANDWICH DIELECTRIC LAYER.

THIS JUNCTION, 43-2-L, HAS A CARBON THICKNESS OF 100 Å ELECTRON-BEAM DEPOSITED AT 11.1 Å.SEC.
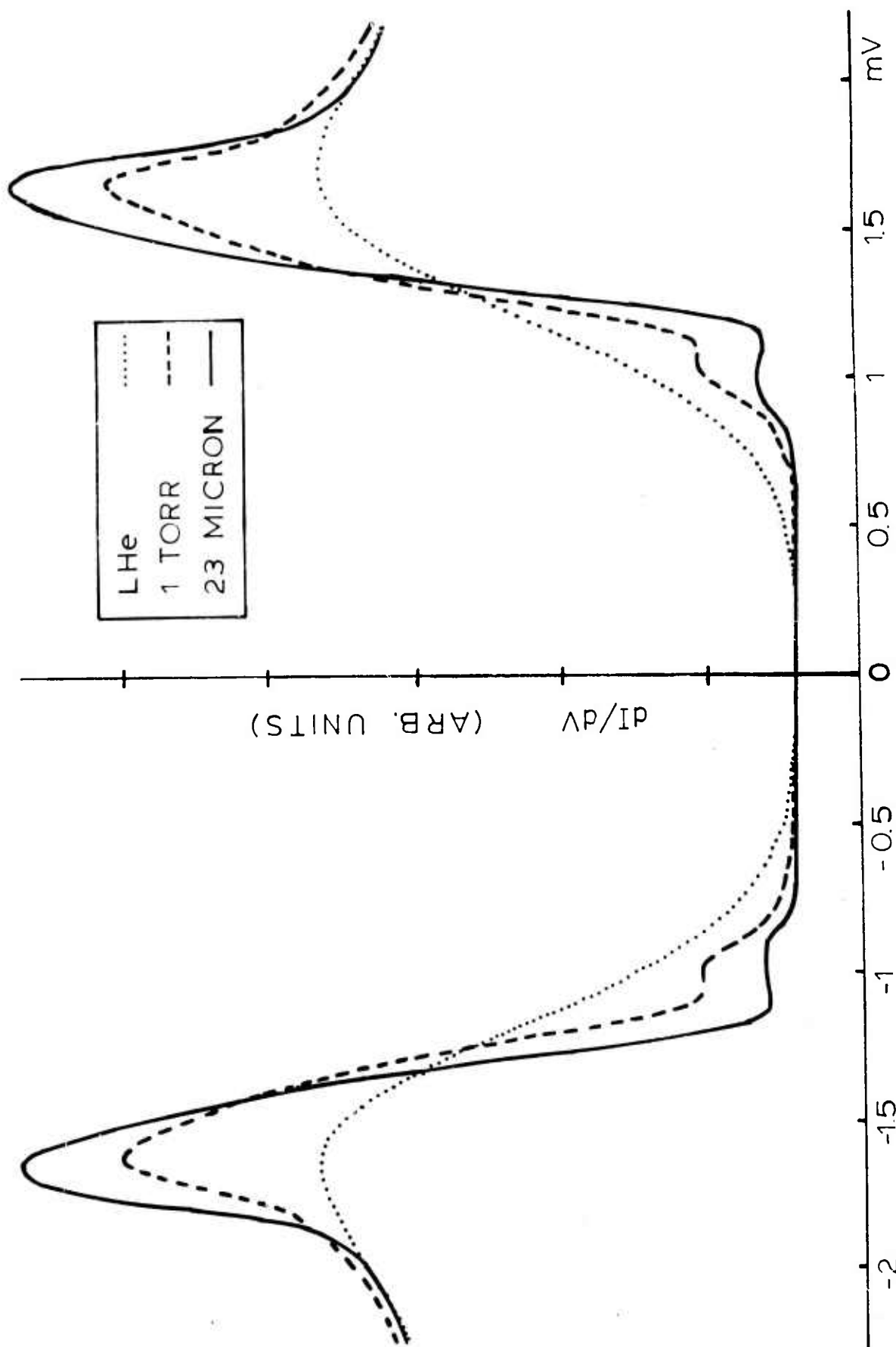
FIGURE 14. DENSITY-OF-STATES CHARACTERISTICS (dI/dV – V) FOR A BULK LEAD-IMPREGNATED VYCOR SUBSTRATE JUNCTION WITH A 95 Å THICK ELECTRON-BEAM DEPOSITED CARBON LAYER AND AN ALUMINUM COUNTERELECTRODE FOR THREE TEMPERATURES: ... 4.2 K; -- 1.3 K; AND —— 0.9 K. THE LEAD-IMPREGNATED SUPERCONDUCTING GLASS

This cryogenic temperature activation energy is a minimum possible value and is of comparable magnitude to superconducting energy gap values. Although this suggests that carbon barrier junctions will never be ideally free of excess currents, this minimum value for the activation energy confirms that carbon can be a viable barrier material. A more quantitative analysis of arc-evaporated carbon of $\sim$100 Å between lead electrodes using Holm's classic barrier model suggests that $\sim$120 mV at helium temperatures is a more realistic value for the activation energy.[7] On the very smooth surface of single crystal niobium and rhenium, we have observed it as high as $\sim$300 mV.[1,6]

Indium substrate junctions were also fabricated using both methods of carbon barrier fabrication. Again, the successful tunneling junctions were those made by electron-beam deposition. One of the successful junctions was even deposited at the extraordinarily slow rate of <1 Å/sec. Success with indium substrate electrodes is particularly encouraging since this material is known for serious agglomeration tendencies which made even natural oxide junction barrier fabrication unusually challenging. $2\Delta_{In}$ was 1.08 mV, in agreement with values reported in the literature.

Bulk lead-impregnated porous glass* is a good test of the carbon barrier technique. Figure 14 shows dI/dV - V for a junction with a 95 Å carbon layer fabricated by the electron-beam technique at 6.3 Å/sec. This is the first planar geometry tunneling data obtained on superconductor-impregnated vycor; previously, only limited success was obtained by the point-contact method and the data resulting was of dubious value for quantitative analysis.[14]

---

*Supplied by Corning Glass Works, Corning, N.Y.

The density-of-states curve is shown at three different temperatures to illustrate the appearance of difference peak, $(\Delta_{glass} - \Delta_{Al})$, as temperature decreased. The energy gap, $2\Delta_{glass}$, is 2.60 mV, slightly smaller, as was expected, than that of bulk lead (2.67 mV). The broad nature of the sum peak located at 1.69 mV, especially on the lower-bias side, suggests that the lead-impregnated vycor is not characterized by a single-gap value, but rather, multiple-gap values. Since the glass-pore size and, thus, the size of the superconducting lead particles is known to vary around an average size of 40 $\overset{o}{A}$, the existence of several gap values is not unexpected. In curves taken out to higher applied biases the phonon structure of the lead was clearly evident.

Tunneling structure was identifiable but accompanied by a major non-tunneling current contributions in junctions of substrate electrodes made of Au films and $Nb_3(AlGe)$ sputtered films and ribbons. The I-V charactertistics of such junctions typically resembled a polarity-independent semiconducting diode or varistor plot. Such behavior has been reported in sputtered carbon layers betwen aluminum film electrodes.[15] These plots indicate a very low barrier height, possible arising from impurities in the barrier itself or from effects of suboxide formation at the metal-carbon interface. The carbon films themselves are electrically continuous and of uniform coverage.

Tunneling structure was not identifiable in junctions fabricated with silver or lead-bismuth film substrate electrodes. Even in these junctions, however, as in all the previously discussed electron-beam deposited carbon layer junctions, the observed properties could be consistently reproduced, in

contrast to the results with arc-evaporated carbon.

Four general criteria for identifying good carbon barrier tunneling junctions have been determined. These concern the color of the carbon film, the deposition rate of the carbon film, the behavior of the slope of the I-V characteristic with temperature, and the junction resistivity at 4.2 K. The criteria do not all have to be simultaneously satisfied; eight of the junctions satisfied some of these criteria; three satisfied all four criteria. Unsuccessful junctions tended to satisfy two or less. It is interesting that all of the criteria relate directly to deposition rate to some degree. This suggests that it is the most crucial fabrication parameter in determining carbon barrier performance.

The visual color of the carbon film is tied to the thickness of the deposited carbon and to the resistivity of the junction. In Figure 15 the outline of the carbon barrier layer is clearly apparent in the sample's crossed-electrode geometry. We have been able to develop a color chart so that for a given deposition rate, the resistivity and final junction performance of such layers can be predicted from their appearance. Films up to 30 $\overset{\circ}{A}$ thick have a clear-to-faint-powdery-white appearance; 30-60 $\overset{\circ}{A}$ films have a nearly invisible, reddish-brown cast to them; around 80 $\overset{\circ}{A}$, films become distinctly reddish-brown and gradually darken to brownish-black as thickness increases; films in excess of 250 $\overset{\circ}{A}$ are mostly black with a brown cast.

The carbon barriers group according to their resistivity vs temperature behaviors. We can identify several categories of these behaviors, including one where: resistivity typically increases several orders of magnitude
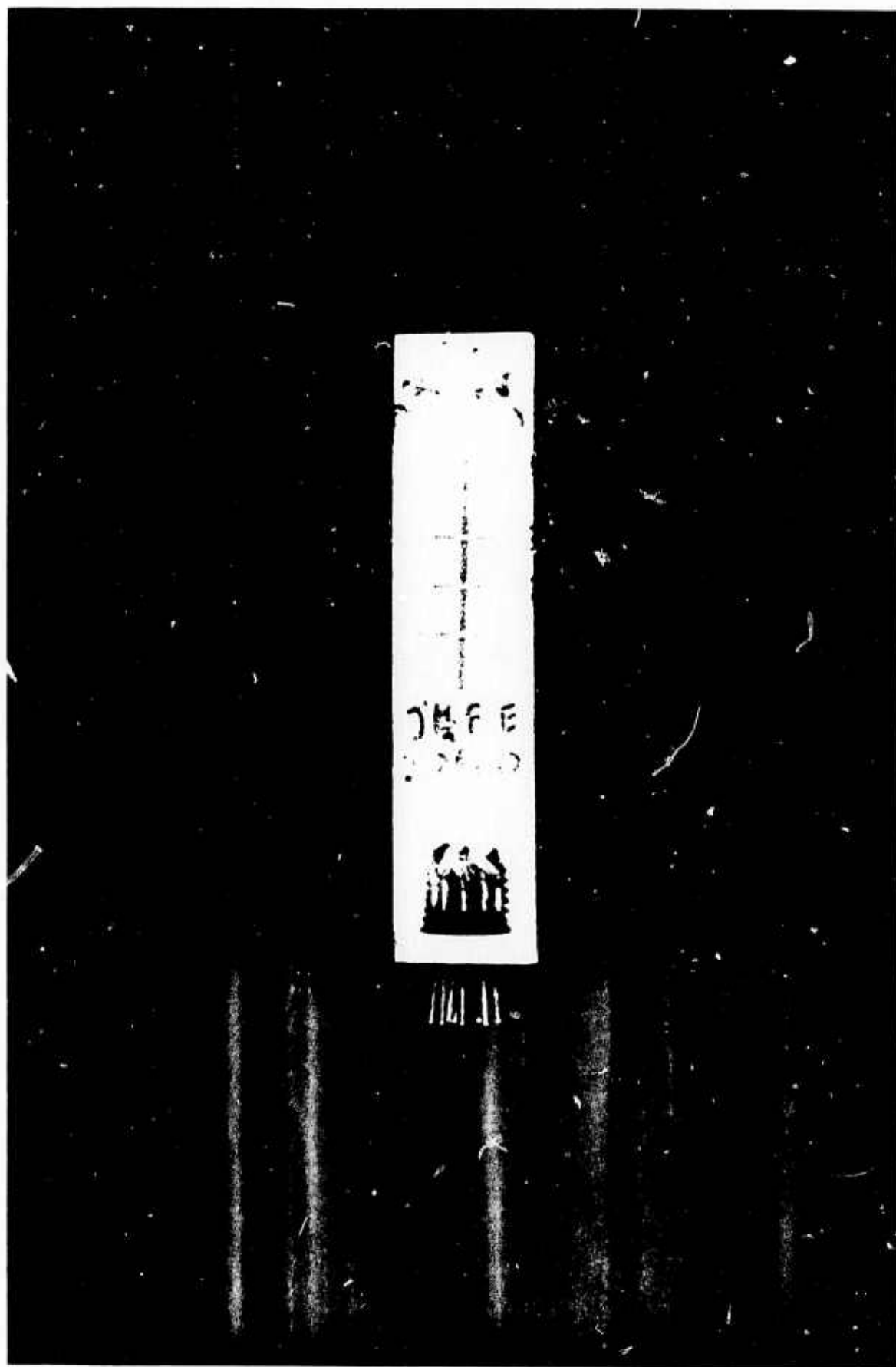
15. CROSSED METAL SUBSTRATE AND COUNTERELECTRODE FILMS SEPARATED BY A WIDER STRIP OF AMORPHO CARBON MAKING THREE JUNCTIONS ON THE GLASS SLIDE.

between room temperature and 4.2 K; the deposition rate is approximately 10 Å/sec; and film thickness is generally greater than 100 Å. All eleven of the successful tunnel junctions fall in this category of resistivity vs. temperature, deposition rate, and thickness. For the thiry-four junctions as a whole, resistivity generally varied inversely with deposition rate. For a given rate, resistivity was proportional to films thickness in a non-linear manner.

It was observed that the four-point probe configuration used on the junctions gave negative sloping I-V characteristics at some temperature. Sometimes these persisted well below 77 K before turning positive again in slope. Such behavior is encountered when junction tunneling resistance is of the same order of magnitude as the metal electrode resistance.[13] Reversal of slope sign as temperature decreases is a commonly used indicator of good quality tunneling junctions. Of the eleven successful carbon barrier junctions, nine exhibited this behavior.

As temperature decreased, resistivity increased. For the junction areas used, 4.2 K resistances were in the range of 10 to 7500 ohms, corresponding to liquid helium temperature resistivities of 10^5 to 10^9 Ω-cm, respectively. The literature suggests that good barrier resistance falls between 1-1000 ohms irrespective of barrier material or fabrication technique, and that the optimum oxide barrier resistivity is approximately 10^5 Ω-cm. These carbon barrier junctions are easily as rugged as natural oxide barriers. Repeated temperature cycling did not adversely affect their overall performance. In one respect, however, they tended to behave opposite to oxide barriers:

whereas oxide barriers generally age so as to eliminate tunneling curve
substructure related to the barrier nonuniformities or hasten dielectric breakdown;
carbon barriers age so as to enhance substructure (e.g., multiparticle
peaks) and maintain their dielectric strength.

Another rather intriguing property we sometimes observe in carbon films is a
time-rate of change of resistivity under sustained electric field at cryogenic
temperatures. In particular, in the sandwich geometry, the carbon layer
exhibited continuous changes in resistivity over individual testing periods
of approximately one to two hours of applied bias. One manifestation of
this change was an increasing smoothing of the superconducting density-of-
states as the excess current caused by the changing barrier resistivity
began to dominate the signal. There were also other manifestations in the
form of structure seemingly related to the barrier itself, not the electrodes.
These kinds of behaviors were observed for several electrode species, including
bulk $Nb_3(AlGe)$.[16] The effect was distinct from aging, which we also observed.
The field-dependent resistivity behavior seems related to a second property
sometimes observed in our sandwich geometries. In these cases, over a few
minutes or hours and once even over 46 days, the barrier experienced "break-up"
under applied bias. The term breakdown refers to the sudden decrease in
resistivity of sandwich dielectric layer. In the case of our carbon,
the resistivity suddenly increased. Such behavior was observed in different
combinations of electrode species.

Recently we have learned of independent observations of similar behaviors
by K. Antonowicz[17] who worked with Al-C-Al sandwiches at room temperature.
In these samples he observed a slowly decreasing resistivity under applied

bias behavior as we do, and slow time response as well. He observed "break-up" when the resistivity decreased so much as to pass current in excess of a threshold current related to sandwich geometry. The voltages he noted for "break-up" were approximately 2 volts, while our electrode-carbon combinations, tested at cryogenic temperatures, exhibited "break-up" at voltages in the millivolt range. For his voltages, Antonowicz observed that application of a weak magnetic field ($\sim \frac{1}{2}$ gauss) resulted in a sinusoidally varying threshold current, J_{max} vs H. The response time of his junctions was hours. Our junctions were always in the earth's background field; however, our gold substrate carbon barrier junctions did respond to a larger magnetic field with a J_{max} growing and diminishing as a function of increasing field. When we applied fields approximately 10 times larger than the earth's field, we were able to drive some of our junctions out-of, and into, the break-up resistivity mode by consecutive application and turning off, respectively, of the field. Even with no applied field other than the earth's background, we occasionally observed instabilities in the junction's preferred I-V (or resistivity) mode.

Sputtered amorphous carbon films of considerable thickness (1000-3000 $\overset{o}{A}$) have recently been reported by Morisaki, et al., [18] to switch differently at room temperature according to whether the electrodes were aluminum or copper, and according to whether a fabrication configuration was Al-C-Cu or Cu-C-Al. The carbon-aluminum interface was much more definitive in producing Morisaki's switching results than was the carbon-copper interface, the latter often exhibited no switching or memory effects, in fact. His conclusions are in agreement with many of our own observations concerning

the importance of the counterelectrode in the performance of a junction.[19]
The vacuum pressure during its deposition, its work function, and its energy
upon impact are all known to effect junction performance.[20] Our data further
suggest that for both oxide and carbon barriers, effects of the system of
substrate electrode-barrier-counterelectrode may be evident in the phonon
spectrum we determine from tunneling curves.

Artificial tunneling barriers need not be composed of carbon. An alternative
approach is to deposit a thin layer ($\sim$20 Å) of a simple metal on top of the
substrate material and then to throughly oxidize the layer to form a tough,
continuous, insulative oxide. Taylor[4] pioneered this technique utilizing
Al and Ti barrier layers. The junctions exhibited reasonable resistances,
help up well to temperature recycling and remained stable in characteristics
over several days. This barrier fabrication technique has two disadvantages:
its usefulness on relatively rough surfaces (such as some of our A15's)
is doubtful, and its yield of successful barriers for anyone except Taylor
has been almost 0%. On the other hand, no one has been up against a material
which is as difficult a substrate as the A15's before, and therefore they
did not have to seriously exhaust all barrier fabrication approaches.

We modified our counterelectrode evaporators with stroboscopic shutters
in order to be able to control deposition for metal thicknesses of the order
of 20 Å. Todate, approximately ten oxidized aluminum layer junctions have
been tried on $Nb_3(AlGe)$ and V_3Au arc-cast button external and fractured
surfaces. For very thin Al_2O_3 layers ($\sim$20 Å), junction I-V characteristics
were those of shorts. For very thick aluminum layers (several hundred Å),
the characteristics were those of a superconductor-normal junction--indicating

that the aluminum was not oxidized through and that the remaining aluminum
was "screening" the effects of the A15 substrate from appearing in the I-V
curve. At an intermediate thickness ($\sim$80 $\overset{o}{A}$), definite tunneling structure
did occur in the curves consistent with high energy gap values for the A15's,
However, the junction characteristics are still far from ideal.

(iii) Directions for Future Work

Preliminary attempts to fabricate bulk V_3Au junctions by formation of an
artificial aluminum oxide barrier proved unsuccessful. Subsequent micro-
scopic examination of the V_3Au substrate revealed sufficient surface roughness
to account for the barrier fabrication difficulties. Thus we must find
new methods to produce a smoother V_3Au surface, but we must also look to
a barrier fabrication technique with a tolerance for a rough substrate,
Electron-beam evaporated carbon films may be able to fulfill our requirements.
We intend to try out such films on vanadium compounds. Based on our experi-
ence to date, a carbon layer of $\sim$100 $\overset{o}{A}$ deposited in 10^{-5} Torr vacuum at
$\sim$10 $\overset{o}{A}$/sec should give us our best chance. We have also recently obtained
planar geometry sputtered Nb_3Ge films from Westinghouse and from Pennsylvania
State University. In addition to pursuing oxide barrier fabrication possi-
bilities, we will attempt carbon barriers on these substrates.

In order to optimize the Al_2O_3 artificial barrier technique and to maintain
microstructural integrity across the barrier-substrate interface, we intend
to use Nb_3Al as the substrate material. The danger of possible incomplete
oxidation of the barrier layer might be offset by the depletion of aluminum

at the alloy surface. We plan to continue to investigate Al_2O_3 barriers on
other A15 materials using layers of aluminum of intermediate thickness
oxidized in pure heated oxygen or by glow discharge in a partial pressure
of oxygen.

We may undertake trial fabrication of barriers on niobium-based alloys
[e.g., $Nb_3(AlGe)$, Nb_3Ge] by depositing very thin layers of niobium and oxidiz-
ing them through. The better properties of niobium, and the well known
oxidation tendencies of this element whenever researchers attempt to sputter
it, suggest that niobium oxide layers may be successful barriers on some of
our substrate materials.

There are several things that remain to be investigated about the carbon
technique itself which should lead to improved tunneling barrier heights:

    i)   low temperature annealing of the carbon-substrate system _in situ_
            before counterelectrode deposition;

    ii)   cooling of the metal substrate during deposition of the carbon;

  iii)   deposition of the carbon in the presence of particular gaseous
            species;

    iv)   intentional contamination of the substrate metal surface prior
            to carbon deposition.

IV. Superconducting Microwave Cavities

The goal of this aspect of our research is to develop the technology for the manufacture of practical superconducting microwave cavities. Low losses, high breakdown fields and durable, reliable performance with no degradation, even with exposure to humid air must be achieved before microwave superconductivity will enjoy wider application. The leading candidate material for superconducting cavities is, nominally, pure Nb, for various reasons which are discussed in detail in our previous proposals and publications.[1] However, the development of Nb cavities has been difficult, expensive, and somewhat disappointing in terms of reproducibility of properties, shelf life, and the very elaborate measures needed to produce good properties.[1,2]

Alloys as cavity materials have been relatively speaking, neglected. Several practical reasons for such neglect may be anticipated. Alloys are inherently inhomogeneous: even if the composition lies clearly in a single-phase field on the appropriate equilibrium phase diagram and the possibility of meta-stable second phases avoided, the phenomenon of coring or non-equilibrium solute segregation is almost completely unavoidable. It is also true that for many alloys the surface is not representative of the bulk,[3] although this need not be true for different alloys under special fabrication conditions. Historically, there was also the belief that H_{C1} would be the limiting AC field for microwave applications[4]; however, recent theoretical[5] and experimental[6] results suggest that the upper limit may be H_C rather H_{C1}.

Since the paractical problems associated with preparing Nb for cavity
material seems as great as the problems involved in preparing a good,
homogeneous binary substitutional alloy, we reexamined various alloy
systems with high transition temperatures for an alternative. We chose
to investigate $Mo_{.75}Re_{.25}$ for the following reasons:[7]

(1) it has a high T_c ($\sim 10°K$) to allow for low theoretical loss
at practical operating temperatures, and a high H_c (~ 1600 G);

(2) low κ to give a high H_{C1} (~ 500 G) since it had not been con-
clusively shown that H_c not H_{C1} is the limiting magnetic break-
down field. Furthermore a low κ increases the stability of
the low loss Meissner state and should lessen the effect of
small inhomogeneities via the proximity effect;

(3) it is a solid solution alloy and therefore eliminates many
of the bulk and surface homogeneity problems associated with
the compound;

(4) 25 at. %Re gives the highest T_c for the MoRe system without
the presence of the normal conducting σ second phase;

(5) solubility for interstitials is a minimum in the MoRe system at
25 at % Re;

(6) MoRe alloys have nearly ideal magnetization curves without the
extensive annealing required for similar behavior in Nb;

(7) the thermal conductivity of Mo-25Re is higher than that of
Nb at low temperatures which should increase thermal stability
at high power levels.

Approximately a year and a half ago we completed the first measurements
which demonstrate the feasibility of the Mo-25Re alloy as a superconducting
cavity material for microwave application.[1] The measurements were made on
TE_{011} mode Nb cavities with removable Mo-25Re backplates. We subsequently
showed that these measurements indicated an upper bound of 2.8 microhms
for the surface resistance of the backplate at 1.4°K and 11.2 GHz, and a
lower bound of 102 gauss for the breakdown field.[8] We believe these figures

to be quite conservative, as it is highly probable that the breakdown occurred in the Nb component, as did the losses due to resistance; in any case, such a surface resistance already corresponds to useful device applications if the breakdown field can be improved. Subsequently, we fabricated two cavities with removable backplates made entirely of Mo-25Re. Initial trials with one cavity after electropolishing and annealing in ultra-high vacuum gave encouraging results, but attempts to optimize surface preparation parameters yielded severely degraded Q-values until these were below our ability to measure them.

(i) Previously Reported Results

In this section we review briefly our initial feasibility study.[1] An electropolished and anodized Nb TE_{011} mode microwave cavity, resonant at 11.2 GHz built from a two piece design in the form of a cylindrical cup and flat circular endplate, was used to measure a $Mo_{.75}Re_{.25}$ sample backplate. The Nb cup and endplate stock were recrystallized at 1400°C in 10^{-8} torr for 2 hours, machined, and electropolished to remove 80μ of surface.[9] Before assembly the cavity pieces were again electropolished to remove 6μ and finally anodized at 20V, 0.5 mA/cm^2 in 12.5% NH_4OH solution. Then they were assembled wet in reagent methanol using In gaskets. The cavity was attached to the wave guide and tested with the single coupling hole always pointing down in order to keep dirt from falling into the cavity. The cavity was evacuated through the waveguide with a liquid N_2 roughing pump followed by a 25ℓ ion pump. The earth's magnetic field was screeneed to less than 6 mG with μ-metal shielding. The cavity

was measured by means of the decrement method after the Gunn diode micro-wave source had been passively stabilized to the cavity resonance. The coupling coefficient, β, could be varied by a factor of 30 by means of a movable Nb probe in the waveguide near the coupling hole. A β of 1.6 or less was thus maintained in order to obtain accurate measurements. High power measurements were made with a TWT amplifier and a novel oscillator locking technique which utilized passive stabilization.[1] After initial measurements were made on the all-Nb cavity, the Nb endplate was replaced by one made of Mo-25Re.

The Mo-25Re sample endplate was ground from an arc cast button with a small alumina wheel. The sample plate was then polished by hand with SiC polishing paper and then electropolished with 4:1 methanol to sulfuric acid to remove about 125µm. The final finish though shiny was uneven on a macroscopic scale, particularly at the grain boundaries. Chemical analyses on chips from the sample plate resulted in 900 ppm O, 2100 ppm C and 40.4 wt.%Re. The rather large amount of O and C present was probably due to the arc melting which is a fast melting process and in a large button results in a good deal of trapped gas. Measurements with a suscep-tability apparatus gave a T_c of 10.1°K. Similar measurements on a much smaller arc melted button resulted in 150 ppm O, 300 ppm C, 41.3 wt.%Re and a T_c of 9.75°K.

Before assemblage onto the Nb cup, the Mo-25Re endplate was electropolished to remove a further 8µ, then the Nb cup, as well as the backplate, were rinsed in reagent methanol and assembled wet. For an incident power level of 18 mW at 1.4K the Q_o for the all-Nb test was 5.85×10^8 and for the MoRe/Nb

combination 4.50 x 10^9, yielding a residual surface resistance R_o of
2.8 μ-Ω if the anodized Nb surface can be assumed not to have degraded
between tests.* If the Nb surfaces had degraded in any way, R_o for the
Mo-25Re would be less, making it even more useful as a cavity material.[1,8]
The results of high power tests with the Mo-Re backplate at 1.4K were
Q_o = 1.45 x 10^8 at 102 G when breakdown occurred. Although this break-
down probably occurred on the Nb surfaces, it may also be taken as a lower
bound for the alloy. A more realistic figure can only be determined in
tests with an entire Mo-25Re cavity. It should noted, however, that an
increment of a factor of three in this figure would make Mo-25Re as good
a cavity as those presently in use in linear accelerator operation.**

(ii) Current Research

Subsequently, in order to obtain quantitative measurements rather than
upper and lower bounds, we proceeded to fabricate cavities entirely of
Mo-25Re. An ingot with material adequate for two X-band cavities of
Mo-25Re was electron-beam melted. After a certain amount of redesign,
the first cavity was machined: rough machining was performed by the
electrical discharge technique and the final "machining" done by hand
grinding. Various trials were carried out on small pieces of the alloy
to optimize the electropolishing sequence. A preliminary test was
performed on the cavity in the as-ground condition with no heat treatment

---

*In fact, previous testing of the entire Nb cavity indicates this is
not so: the cavity always degraded between such tests.[1]

**See Ref. 8 for LINAC parameter estimates.

or electropolishing. The result was an unloaded Q (at 1.4K) of about 10^6, which was encouraging considering the severely disturbed and irregular condition of the ground surfaces. As a test of the relative importance of the severely deformed surface layer (created by the final grinding to shape), we removed 50μ more from the interior of the cavity by electro-polishing and then remeasured Q_0 which was found to have increased to ca. 10^7 although the cavity was not even on resonance. We estimate that only about half of the disturbed layer had been removed. (No high-temperature annealing had as yet been performed.) A second such test brought the cavity Q to 4×10^7.*

In the first trial of cavity I after a firing anneal at 1800 C in 4×10^{-8} torr pressure a Q_0 of 1×10^9 at 1.4K resulted. (This corresponds to a residual surface resistance of 0.7 μ-Ω.) The details of the surface preparations are given in Table (1), entry 4. Before annealing the cavity for this trial, it should be noted, the surfaces resulting from the previous polishing procedures were smooth, bright, and mirror-like except for a few etch pits on the bottom of the cavity. After the heat treatment there were large and visible grains. In addition, during the annealing/assemblage stage the inside of the cavity was accidentally con-taminated with diffusion pump oil. An aging test on this cavity showed a Q degradation to $\sim 3 \times 10^8$ after three days; and even cleaning up the pump oil or electropolishing to smooth the surface did not return the cavity Q to 10^9. After this, Q values degraded to very low values even

---

*Most of the tests on the Mo-25Re cavities are low power tests with 10 mW incident power levels.

TABLE 1.

Sequential Surface Preparation -- Cavity 1

Test No.	Treatment	Q at ~ 1.4 K
1.	(As machined) Ultrasonically cleaned; trichlor, acetone, methanol; Rinsed (4 times): methanol.	$\sim 10^6$

2.	Electropolished (11 times) at 27 V
	   using 6:1 methanol/H_2SO_4;
	Rinsed: H_2O, NH_4OH, then (3 times)
	   methanol.
		1.2×10^7

3.	Electropolished 4 times as above; Rinsed: methanol, (2 times) H_2O, then (2 times) methanol.	4.0×10^7

4.[a]	Ultrasonically cleaned as in #1;
	Annealed in rf induction furnace:
	  <u>Cup--Diffusion pump</u>
	    temperature $\leqslant 1800$ C
	    pressure = 4×10^{-8} torr
	    duration = 8 hours
	    cooling time = 23 hours
	
	  <u>Plate--Ion Pump</u>
	    temperature $\geqslant 1800$ C
	    pressure = 4×10^{-8} torr
	    duration = 5 hours
	    cooling time = 2 hours;
	Backfill with N_2 gas.
		$\sim 1 \times 10^9$

5.	Aged #4 for 3 days.	3×10^8
6.	Degreased: trichlor; Ultrasonically cleaned: methanol; Rinsed (3 times): methanol.	4×10^8
7.[b]	Electropolished 3 times as in #3; Rinsed: H_2O, methanol, H_2O, (2 times) methanol.	3×10^7

TABLE 1. Continued

Test No.	Treatment	Q at ~ 1.4 K
8.	Electropolish plate as in #3; Annealed cup/plate in rf furnace with ion pump: temperature ~ 1550 C pressure = 2 x 10^{-8} Torr duration = 8 hours cooling time = 2 hours; Backfill with N_2 gas.	6.5 x 10^8
9^c	Aged #8 1 day; Retested in situ (high power).	~ 2.8 x 10^8
10.	Electropolish at 19.5 V as in #3: cup--8 times plate--6 times.	1 x 10^8
11^d	Annealed cup/plate in rf furnace with ion pump: temperature = 1740 C pressure = 4 X 10^{-8} Torr duration = 3 hours cooling time = 16 hours; Backfill with N_2 gas.	2 x 10^7

a. During N_2 backfill, pump oil contamination of surface.

b. A visible bad spot appeared on cavity wall, probably due to arcing.

c. Breakdown field = 74 Gauss.

d. Subsequent treatments $Q \leqslant 4$ x 10^6 until cavity remachined.

using very similar surface treatment as described above (see other entries Table 2) indicating that perhaps a drastic change had taken place in the surface composition or that the alloy texture itself had changed because of the various heat-treatments.*

In order to determine if our heat treatments were responsible for the degraded Q's we returned cavity I for remachining. About 70μ of material was removed from the interior surface of the cavity. In the as-received condition there were visible grooves so the cavity was electropolished with a 5:1 solution of methanol and surfuric acid (as in entry 3, Table 1) before testing. Just as before the cavity was remachined, the Q-value was too low to be determined with the present configuration ($\leqslant 10^6$). While this cavity was unavailable our second cavity (cavity II) was received and testing initiated. The results of those trials made us hesitant to reanneal cavity I with our previous heat treatment until we are reasonably sure of the mechanisms operating to degrade our surfaces.

The performance of cavity II has been consistently lower than the best rf values obtained with cavity I. The history of the surface treatments for cavity II are given in Table 2. Initial tests on the as-machined cavity after electropolishing (as in entry 3, Table 1) gave a $Q \sim 6 \times 10^7$ which is a factor of 5 better than for cavity I. This did not surprise us

---

*We calculated the Mo and Re profiles at the surface as a function of annealing temperature to determine the effects of the 1850 C firing. An optimal solution of the Fick diffusion equations (with respect to preferential Mo loss) predicts that an 8 hour 1650 C anneal would result in a decrease of only one at.% Mo at the surface which, of course, should not seriously alter the desired alloy properties. Hence, we lowered our annealing times to be on the safe side.

TABLE 2.

Sequential Treatment: Cavity II

Test No.	History	Q at 1.4 K
1.	(As-machined) Cleaned and Rinsed: Trichlor, acetone, and methanol	$\sim 10^6$
2.	Electropolished to remove 45 μm	6.2×10^7
3.	Anneal at 1650 C for 4 hours (Cooling time = 13 hours)	6×10^7
4.	Electropolish to remove 10 μm Anneal at 1800 C for 8 hours (furnace cool, 14 hours).	$< 10^6$

because after this polishing the surface of cavity II looked much smoother and more mirror-like than the same surface for cavity I.* Cavity II was then fired at 1650 C for four hours, wet assembled and measured; Q remained 6×10^7. All subsequent tests, after both additional electropolishing and annealing have had unmeasurable Q's ($<10^6$).

In order to account for these results, several studies have been done on machine chips from the starting ingot, actual cavity surfaces, and on buttons removed from various sections of the starting ingot. We summarize below the various tests and our results.

Chemical Analysis

While the overall composition is close to the Mo-40 wt%Re alloy anticipated, there were indications of small compositional variations through out the ingot.

X-ray Powder Diffraction

The powder pattern for the alloy annealed at 1000 C for 65 hours indicated a pure b.c.c. structure with a lattice constant of 3.1212 Å which is close to the expected value for Mo-25Re. For unannealed samples there were extra unexplained peaks that could have resulted from mechanical strain or oxides.

Electron Probe Microanalysis

This study is inconclusive at the present time but there is a strong indication of the presence of very localized ($\sim15\mu$) regions where there

---

*It is true, however, that the visual surface conditions are usually not well correlated to the resulting Q's.

is no Re at all and the Mo content is low in comparison with the matrix. The existence of such regions could easily nucleate the normal regions making the attainment of high Q's all but impossible. The next step in this study is to do a line scan study for the variation in composition on the surface of the various metals used in all aspects of this research (and which could contaminate the surface). Thus, apart from checking the variation of Mo and Re we plan to check for Fe, In, Cu, W, Ta, Nb, and Al, especially Cu.

SEM/EDAX and Photomicrography

These have indicated that, in general, our surfaces for rf tests are smooth. Depending on the type of surface treatment, surface compounds, probably oxides or either Re or Mo, or both, may have been slowly formed on the surface.[10] These could conceivably produce the low Q's we have observed after such treatments. The effects of our heat treatment has been studied by preparing Mo-25Re buttons taken from the starting ingot in the same manner as the actual cavity surfaces. Figure (16a) shows the results (X1,150) of heating at 1850 C (8×10^{-8} Torr) and quench cooling in Argon gas. Subsequent heat treatment, it is felt, might bring up the light "dots" into precipitates. A button heated at 1850 C (10^{-7} Torr) and allowed to furnace cool (x1,150) is shown in Fig. (16b). One of the small diamond shaped precipitates is shown at a larger magnification (x23,200) in Fig. (17a). This sample was then heavily etched in solution 6:2:92 (potassium ferricyanide, potassium hydroxide, water) with results as shown in Fig. (17b) at x5,350. In general, the precipitates are pseudo-acicular in shape, resembling primitive arrowheads, and have a well-defined orientation relative to the crystal structure of the matrix. The appearance of the precipitates in

FIGURE 16. PHOTOMICROGRAPHS OF MO-25RE BUTTONS.
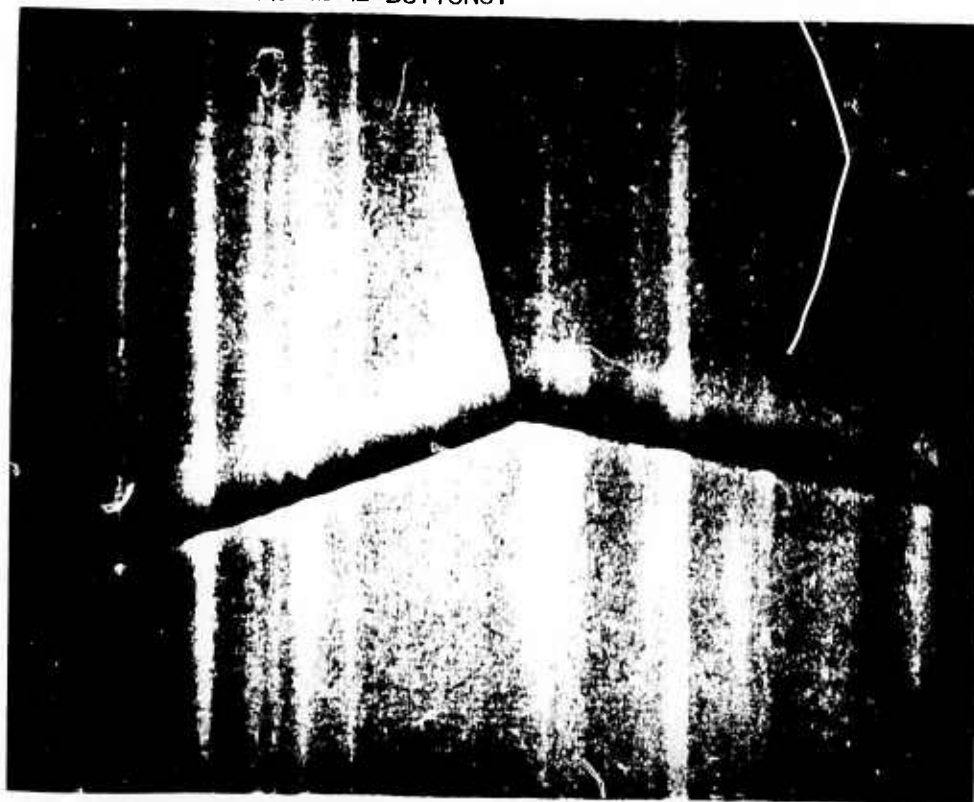
ARGON QUENCH
COOLED (x2320);

(A)

FURNANCE COOLED
OVERNIGHT (x115

(B)

FIGURE 17. PHOTOMICROGRAPHS:

(A)

MAGNIFICATION OF A
DIAMOND-LIKE STRUCTURE
OF FIG. (16B)
X23,2000;

(B)

RESULTS OF ACID ETCH
(CF. TEXT) ON STRUC-
TURE IN (A), MAGNIFI-
CATION X5350.

Figs. (16b) and (17a) is due to the section being perpendicular to the preferred acicular axis.

Our preliminary evidence is that these precipitates are alloy oxides. In support of this conjecture, a recent paper[10] on the oxides of foils of Mo_2Re has reported preferential oxidation and evaporation of Mo. In addition, the author points out that the Mo and alloy precipitates form even at low temperatures and on each reheating fresh precipitates have been found. These also have a needle shape although they are not as pronounced as in our study. In our case if we have oxide precipitates, then because the oxides of Mo and Re are both reduced by hydrogen above 800 C, we should be able to "recondition" our srufaces by modifying our tube furnace with flowing H_2 gas.

(iii) Direction of Future Work

The surfaces of our Mo-Re cavities are now being annealed in a hydrogen gas atmosphere at $\simeq 1000$ C. We feel that with the cavities in their present state the hydrogen will reduce the oxides and return our surfaces to their original condition. The first trial with this method made it possible, once again, to measure a Q for cavity I ($\sim 10^7$). Having reconditioned the material, we intend to continue to search for optimal surface preparation techniques. We will then make measurements of the surface resistance and breakdown field as functions of temperature, and investigate other practical considerations such as conduction aging, "shelf-life", and sensitivity to mere atmospheric exposure. These cavities will then be used for measurements of basic properties at the alloy surface as a function of surface condition.

V. References

Section II.

1. K. Heckler, G. Horn, G. Otto, and E. Saur, J. Low Temp. Phys. $\underline{1}$ (1969) 29.

2. J. A. Gregory, J. Bostock, M.L.A. MacVicar, and R. M. Rose, Phys. Lett. $\underline{46A}$ (1973) 201.

3. James Allen Gregory, S.B. Thesis, MIT (Metallurgy and Materials Science, 1973) unpublished.

4. B. Hillenbrand, H. Martens, H. Pfister, K. Schnitzke, and G. Ziegler, Proc. of 1974 Appl. Supercond. Conf., Illinois IEEE Trans. MAG-11 (1975) 420.

5. ARPA Semi-Annual Technical Report #1, 1 July 1973-31 December 1973,

6. R. Löhberg, T. W. Eager, I. M. Puffer, and R. M. Rose, Appl. Phys. Lett. $\underline{22}$ (1973) 69.

7. J. L. Miles and P. H. Smith, J. Elec. Soc. $\underline{110}$ (1963) 1240.

8. T. P. Sheahan, Phys. Rev. $\underline{149}$ (1966) 368.

9. A. Müller, Z. Naturforsch. $\underline{25A}$ (1970) 1659; G. Arrhenius, et al., Proc. Nat. Acad. Sci. $\underline{61}$ (1968) 621.

10. Jeffrey G. Kohr, Ph.D. Thesis, MIT (Metallurgy and Materials Science, 1971) unpublished; C.E. Lundin, A.S. Yamamoto, Trans. AIME $\underline{236}$ (1966) 836.

11. Noah Mendelsohn, S.B. Thesis, MIT (Physics, 1974) unpublished; Myron Hale Frommer, Ph.D. Thesis, MIT (Metallurgy and Materials Science, 1975) unpublished.

12. J. Bostock, Kofi Agyeman, M.H. Frommer, and M.L.A. MacVicar,
     J. Appl. Phys. 44 (1973) 5567.

13. W. N. Cheung (unpublished).

14. L.E. Hasselberg, M.T. Levinsen, and M.R. Samuelsen, Phys. Rev. B9
     (1974) 3757; I. Giaever and H.R. Zeller, Phys. Rev. B1 (1970) 4278;
     N.R. Werthamer and Sidney Shapiro, Phys. Rev. 164 (1967) 523; N.R.
     Werthamer, Phys. Rev. 147 (1966) 255.

15. ARPA Semi-Annual Technical Report #1, 1 July 1973-31 December 1973;
     and Alan Jay Dubin, S.B. Thesis, MIT (Electrical Engineering, 1973)
     unpublished.

16. W. Hubin, Tech. Rept. 182 (Department of Physics, University of Illinois,
     Urbana) 1970 (unpublished); W.L. McMillan and J.M. Rowell,
     Phys. Rev. Lett. 14 (1965) 108.

17. Kuang-Hsin (Ken) Lo, Ph.D. Thesis, MIT (Materials Science and Engineering,
     1975) unpublished.

18. R.I. Sharp, J. Phys. C (Sol. St.) 2 (1969) 421 and 431.

19. W.L. McMillan, Phys. Rev. 167 (1968) 331.

Section III.

1. S. I. Ochiai, M.L.A. MacVicar, and R.M. Rose, Solid St. Comm. 8: 1031
    (1970).

2. J.L. Miles and H.O. Mahon, J. App. Phys. 32: 1176 (1961); J.L. Miles,
    S. Shapiro, P.I. Strong, J. Nicol, and P.H. Smith, IBM Journ. 6:34 (1962).

3. I. Giaever, Phys. Rev. Lett. 20: 1286 (1968); I. Giaever and H. Zeller,
    Phys. Rev. Lett. 21: 1385 (1968).

4. B.N. Taylor, Ph.D. Thesis, Univ. of Pennsylvania (Department of Physics, 1963) unpublished.

5. M.L.A. MacVicar, S.M. Freake, and C.J. Adkins, J. Vac. Sci. Tech. 6: 717 (1969).

6. M.L.A. MacVicar, J. App. Phys. 41: 4765 (1970).

7. Kenji Hatada, M.S. Thesis, Kyushu University (Department of Physics, 1971) unpublished.

8. R.C. Morris and R.V. Coleman, Phys. Lett. 43A: 11 (1973).

9. J. L. Bostock, M.L.A. MacVicar, and R.M. Rose, ARPA Semi-Annual Technical Report #3 (December, 1974).

10. J. Kakinoki, Proc. 5th Conf. Carbon, vol. 2, McMillan Co. (New York, 1963) pp. 499.

11. Keith R. Milkove, S.B. Thesis, MIT (Department of Physics, 1975) unpublished.

12. N.F. Mott, Adv. Phys. 16: 49 (1967); C.J. Adkins, S.M. Freake, and E.M. Hamilton, Phil. Mag. 22: 183 (1970).

13. R.L. Pedersen and F.L. Vernon, Jr., Appl. Phys. Lett. 10: 29 (1967).

14. S.E. Moore and P.P.M. Meincke, J. Appl. Phys. 44: 3754 (1973); R. Soulen, Heat Division, National Bureau of Standards, unpublished.

15. H. Morisaki, H. Iwasaki, and K. Yazawa, App. Phys. Letts. 26: 294 (1975).

16. J.A. Gregory, J. Bostock, M.L.A. MacVicar, and R.M. Rose, Phys. Lett. 46A: 201 (1973); J. Bostock, M.L.A. MacVicar, and R.M. Rose, ARPA Semi-Annual Technical Report #1 (December, 1973).

17. K. Antonowicz, Nature 247: 358 (1974).

18. H. Morisaki, K. Saigo, S. Shintani, and K. Yazawa, J. Noncrystal. Sol. 15: 531 (1974).

19. M.H. Frommer, J.L. Bostock, K. Agyeman, and M.L.A. MacVicar, to be published; K. Lo, N. Cheung, J.L. Bostock, M.L.A. MacVicar, and R.M. Rose, to be published.

20. R.M. Handy, Phys. Rev. 126: 1968 (1962); S.R. Pollack and C.E. Morris, J. Appl. Phys. 35: 1503 (1964); J.C. Fisher and I. Giaever, Phys. Rev. Lett. 5: 464 (1960).

Section IV.

1. John Allen Yasaitis, Ph.D. Thesis, MIT (Metallurgy and Materials Science, 1974) unpublished; and ARPA Semi-Annual Techanical Report #2: 1 Jan. 1974-1June 1974; and references therein.

2. H.A. Schwettman, IEEE Trans NS-18 (1971) 134; J.P. Turneaure, IEEE. Trans. NS-18 (1971) 166; P.B. Wilson, Z. D. Farkas, H. A. Hogg, and E.W. Hoyt, IEEE Trans. NS-20 (1973) 104; and P. Kneisel, O. Stoltz, and J. Halbritter (unpublished).

3. J.A. Gregory, J. Bostock, M.L.A. MacVicar, and R.M. Rose, Phys. Lett. 46A (1973) 201.

4. J.P. Turmeaure, Proc. 8th Int. Conf. on High Energy Accel. (CERN, 1971) p. 51.

5. J. Halbritter, Interne Notiz. No. 130 (1971) Institut für Exp. Kernphysik, Karlsruhe.

6. P. Kneisel, et al., IEEE Trans. NS-20 (1973) 63; and K. Schnitzke, et al., Phys. Lett. 46A (1973) 241.

7. J. Dickinson and L. Richardson, Trans. ASM 51 (1959) 1055; J. Halbritter, Proc. 1972 Appl. Supercon. Conf, Annapolis (IEEE Bulletin) p. 622;

W.C.H. Joiner and R.D. Blaugher, Rev. Mod. Phys., 36 (1964) 67;

R.T. Bryant J. Less-Common Met. 4 (1962) 62; D.A. Robins, J. Less-Common

Met. 1 (1959) 396; J.H. Brophy, R.M. Rose, and J. Wulff, J. Less-Common

Met. 5 (1963) 90; and A.C. Anderson and S.G. O'Hara, J. Low Temp.

Phys. 15 (1974) 323.

8.   J.A. Yasaitis and R.M. Rose, Appl. Phys. Lett. 25 (1974) 354; and

J.A. Yasaitis and R.M. Rose, IEEE Trans. MAG-11 (1975) 434.

9.   H. Diepers, O. Schmidt, H. Martens, and F. S. Sun, Phys. Lett. 37A

(1971) 139.

10.   M. J. Witcomb, J. Less-Common Met. 41 (1975) 45.

SECURITY CLASSIFICATION OF THIS PAGE (When Data Entered)

REPORT DOCUMENTATION PAGE

READ INSTRUCTIONS
BEFORE COMPLETING FORM

1. REPORT NUMBER	2. GOVT ACCESSION NO.	3. RECIPIENT'S CATALOG NUMBER

4. TITLE (and Subtitle)	5. TYPE OF REPORT & PERIOD COVERED
RESEARCH IN MATERIALS SCIENCE; Superconducting Transition Metal Alloys.	End of Contract Report June 1, 1973 -- May 31, 1975
	6. PERFORMING ORG. REPORT NUMBER

7. AUTHOR(s)	8. CONTRACT OR GRANT NUMBER(s)
R. M. Rose M. L. A. MacVicar J. L. Bostock	DAHC-15-73-C-0316

9. PERFORMING ORGANIZATION NAME AND ADDRESS	10. PROGRAM ELEMENT, PROJECT, TASK AREA & WORK UNIT NUMBERS
Center for Materials Science and Engineering, Massachusetts Institute of Technology Cambridge, Mass. 02139	3D10

11. CONTROLLING OFFICE NAME AND ADDRESS	12. REPORT DATE
Defense Supply Service - Washington Room ID 245 - The Pentagon Washington, D.C. 20310	July 31, 1975
	13. NUMBER OF PAGES
	76

14. MONITORING AGENCY NAME & ADDRESS(if different from Controlling Office)	15. SECURITY CLASS. (of this report)
ONR Resident Representative Massachusetts Institute of Technology Room E19-629 Cambridge, Mass. 02139	Unclassified
	15a. DECLASSIFICATION/DOWNGRADING SCHEDULE

16. DISTRIBUTION STATEMENT (of this Report)

Unlimited

17. DISTRIBUTION STATEMENT (of the abstract entered in Block 20, if different from Report)

Unlimited

18. SUPPLEMENTARY NOTES

19. KEY WORDS (Continue on reverse side if necessary and identify by block number)

A15 compounds	$Nb_3(Al,Ge)$	amorphous carbon
superconductivity	Nb_3Al	Nb
tunneling	Nb_3Sn	β-W alloys
microwave cavities	junction barriers	transition metal alloys
Mo-Re	artificial barriers	transition metal oxidation

20. ABSTRACT (Continue on reverse side if necessary and identify by block number)

Good superconductive tunneling has been obtained into $Nb_3(Al,Ge)$ ribbon substrates and sputtered films. Unfortunately, the data is surface limited and represents a disturbed layer of $T_c < 7K$. Arc melted buttons of $Nb_3(Al,Ge)$ used as junction substrates have derivative curves which are reminiscent of deformed Nb tunneling data and are, therefore, difficult to interpret. Nb_3Sn substrates formed by the diffusion of Sn into Nb single crystals yield reproducible junctions with gap values ~3.6 mV; the tunneling characteristics are, however, not ideal. A systematic study of the electronic behavior of arc-evaporated amor-

DD FORM 1473 EDITION OF 1 NOV 65 IS OBSOLETE
1 JAN 73
S/N 0102-014-6601 |

SECURITY CLASSIFICATION OF THIS PAGE (When Data Entered)

Block 19

deformed surface layers	tunnel junction deconvolution
X-band cavities	single crystal Nb
surface impedance	deformed Nb
numerical analysis	oxypolishing technique

Block 20

phous carbon films as a function of deposition rate, vacuum pressure, film thickness, ageing, and annealing was completed. General fabrication and performance criteria for effective tunneling barriers between a variety of metal and alloy substrates have been established. Superconductive tunneling was observed with electron beam evaporated amorphous carbon barriers on tin, indium, lead-impregnated porous glass, and bulk $Nb_3(Al,Ge)$. Using a $Mo_{75}Re_{25}$ alloy endplate on an X-band Nb cavity, an upper bound for the Mo-Re residual surface resistence was found to be 2.8 $\mu\Omega$ and a lower bound for the breakdown field 102 G. Initial tests with an entire Mo-Re cavity indicated unloaded Q-values of $5 \times 10^7 - 1 \times 10^9$. Subsequent electropolishing and annealing reduced these Q-values to less than 10^7. Ongoing studies indicate alloy segregation and slowly-forming surface oxides as the cause of the cavity degradation.

FINAL TECHNICAL REPORT
Period: June 1, 1973 - May 31, 1975

Title: Research in Materials Sciences

Project Title:
Chemical Synthesis Using High Temperature Lithium Vapor Species

Contract Number: DAHC 15-73-C-0316

ARPA Order Number: 2469

Program Code Number: 3D10

Name of Contractor: Massachusetts Institute of Technology
Cambridge, Mass.   02139

Principal Investigator: N.J. Grant (617) 253-5633

Project Scientists or Engineers: Richard J. Lagow

Effective Date of Contract: June 1, 1973

Contract Expiration Date: May 31, 1974

Amount of Contract: $770,233

Amount of Project: $124,798

Chemical Synthesis Using High Temperature Lithium Vapor Species

Abstract and Objective

Recent work in our laboratory has resulted in the discovery of several new routes to polylithiocarbons, perlithiocarbons, and inorganic polylithium species. Previously for these classes of compounds, there were very few known examples, and there were no general synthetic routes in the literature. The new synthetic methods are all in the early stages of development and all involve the reaction of high temperature lithium vapor in the range of 800 - 1000°C with various organic, inorganic and polymeric species. During the past year we have succeeded in the synthesis of the first perlithioalkanes, tetralithiomethane, $C(Li)_4$, and hexalithioethane, C_2Li_6. We have also prepared hexalithiobenzene, C_6Li_6, and presently have characterized over thirty such polylithium compounds. An intensive study of these species is now underway and efforts are underway to prepare other polylithiated species. It now appears that polylithiocarbons will be very useful reagents in organic synthesis as well as important monomers and crosslinking agents in polymer synthesis. The synthesis of several types of three dimensional polymers and high temperature materials is underway and is based on routes involving these new polylithium species. The preparation of a new series of diamond-like polymeric materials has been proposed and should result in a new class of high performance materials. Very significant progress has been made over the last year in the polymer area, although a significant amount of time and effort was spent on the constructon of high temperature - high pressure apparatus for such syntheses. Polylithium compounds may also be useful as catalysts.

Summary of Research Progress in the Synthesis Characterization
and Reactions of Polylithium Compounds
8-16-75

Over the past three months, this project has reached a degree of
maturity such that the phase of our research program involving the synthesis
of polymers and diamond-like materials has been initiated. The initial
studies in several areas have been very promising. However, the major
problem remains the purification and separation of the novel polylithium ·
compounds.

The polymer synthesis program is developing in three different
areas. These are the synthesis of polymers in a high pressure - high
temperature apparatus, the synthesis of three dimensional polymers in solu-
tion, and the synthesis of polymers by means of gas phase reaction. The
first high pressure - high temperature studies were conducted a month ago
in a tetrahedral anvil system. A large amount of effort has been devoted
over the past year to the construction of a large high temperature - high
pressure press which is capable of obtaining 40 Kilobar pressures at
$400^{\circ}C$ with significant reaction container sizes on the order of 2 inches
in diameter. Calibration runs were made in November on this new apparatus.
Because the starting materials for these polymer syntheses had been pro-
duced in our program several months ago and because the potential value of
these experiments is so great, a graduate student was flown to a tetra-
hedral anvil facility in Houston to conduct preliminary studies on the
program and in a related area. Even though the container size for such a
high pressure device is only one-eighth inch in diameter, eight experiments
were conducted. The results are now being evaluated. With the completion
of the larger scale high pressure apparatus extensive experimentation will
be undertaken in this area during the next fiscal year, with this being
one of the most important efforts anticipated.

Very promising and exciting results have been obtained in the
development of synthetic reactions in solution between monomer polylithium
compounds and difunctional alkanes. The reaction of dilithiomethane,
H_2CLi_2, with methylene chloride, H_2CCl_2, and with 1,2 dichloroethane have
yielded higher alkanes and a polymer which is very much like polyethylene.
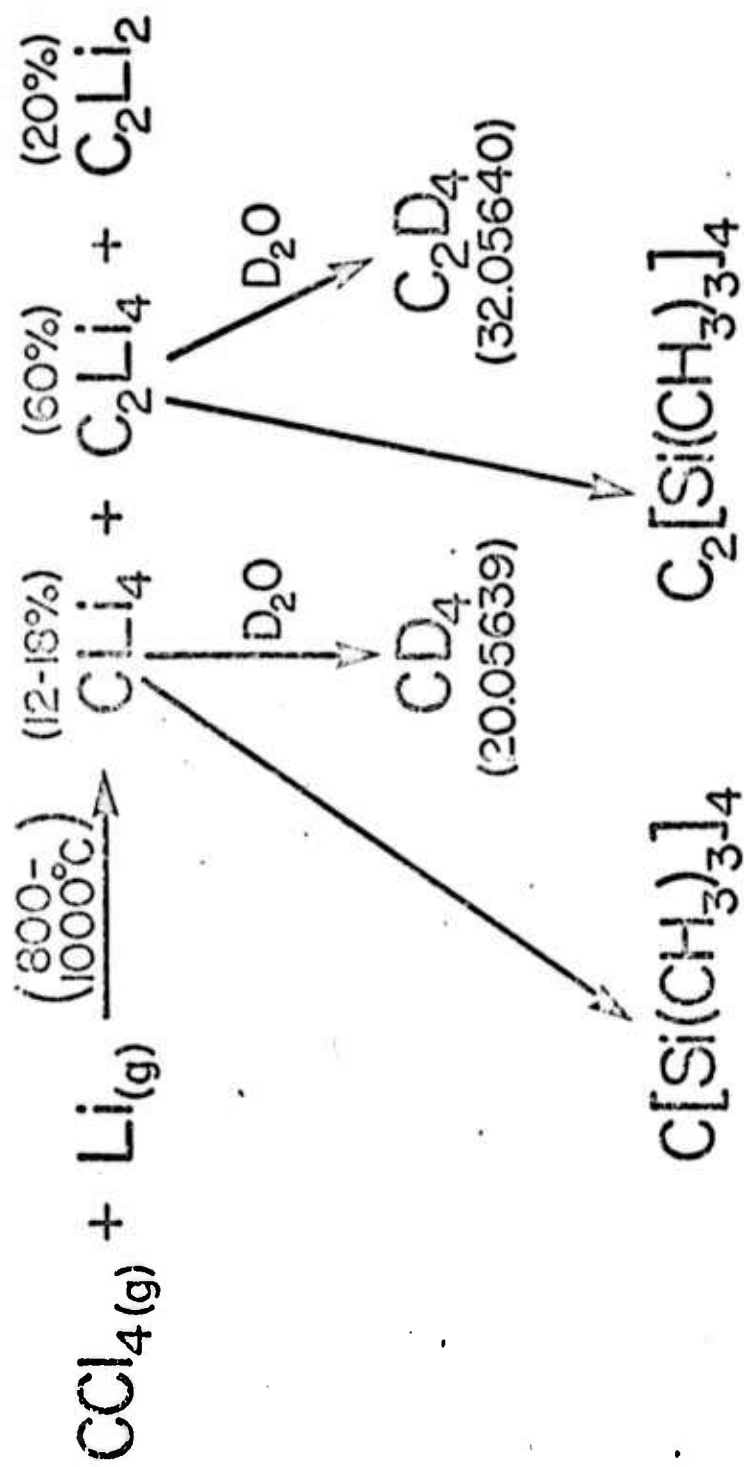This result is a giant step toward the synthesis of three dimensional

polymers from other polylithium compounds and indicates the feasability of such processes. Efforts to maximize and establish the molecular weights are underway.

The discovery that polylithium compounds such as C_3Li_4 may be vaporized without extensive decomposition has led to an experimental program designed to study the reaction of such vapor species with difunctional monmeric materials. The degree of polymerization of such reaction products is under study.

Earlier in our program, a study of the reaction of carbon tetra-chloride, CCl_4 and the reaction of hexachloroethane C_2Cl_6 was conducted with lithium vapor at a $1000^{\circ}C.$[1] The products of the initial reaction were tetralithiomethane CLi_4 and tetralithioethulene Li_2C-CLi_2. (See Figure 1.) These compounds were characterized and it has been found that they react with various organic and inorganic substrates in the manner characteristic of other lithium compounds such as the conventionally prepared monolithium compounds. This experimental result provides evidence of the suitability of such polylithium compounds for reactions as monomers in the proposed diamond-like polymer systems. Subsequently, the reaction of hexachloroethane (see Figure 2) with lithium produced hexolithio-ethane in approximately 80 per cent yield. Again this material has been shown to be a potentially reactive monomer.

A study of the reaction of carbon vapor generated from a carbon arc apparatus at $2500^{\circ}C$ (see Figure 3) was undertaken to establish an alternative method for synthesizing polylithium compounds.[2] (See Figure 4.) The principal product was C_3Li_4 which appears to have the allene structure and might be an attractive monomer. Varying amounts of tetra-lithiomethane and tetralithioethylene were also produced in this study.
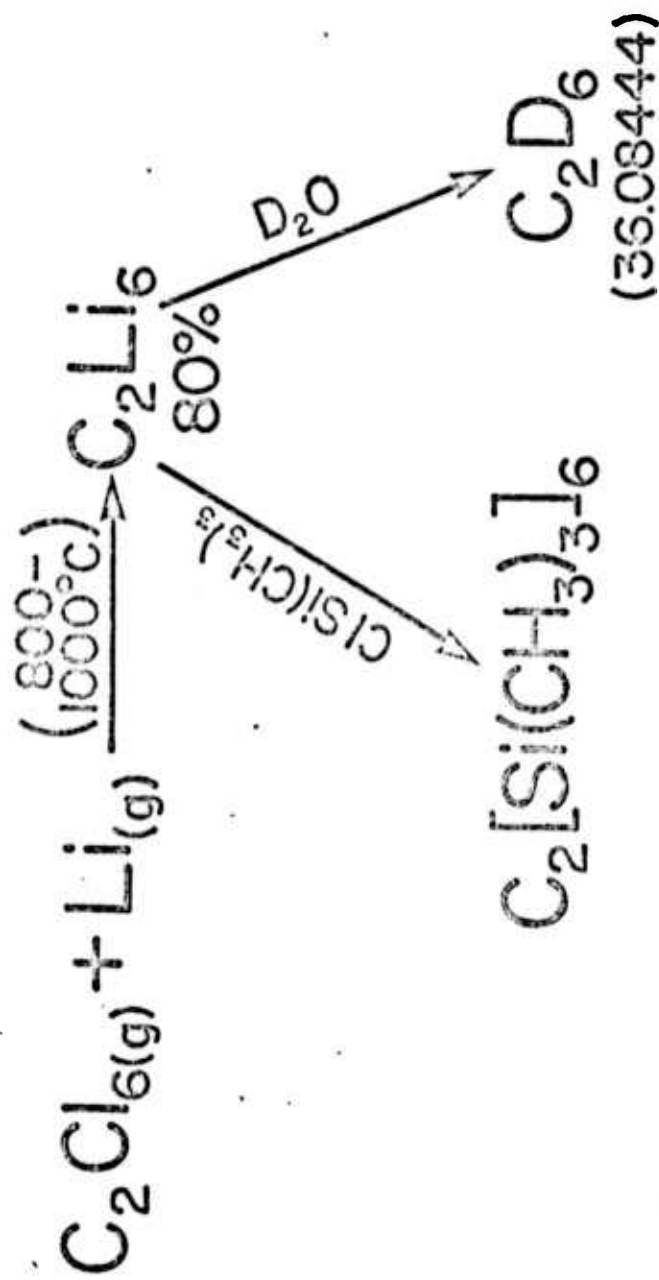
A third publication has resulted from the reaction of lithium vapor with benzene.[3] While for most of our systems the reactants are admitted to the reactor at room temperature and reacted with the high temperature lithium vapor, initial studies giving a small yield of hexa-lithiobenzene prompted us to do a more extensive study based on the reaction of lithium vapor plus benzene at various temperatures. A new type of reactor was designed for this purpose. At room temperature one gets a distribution of lithiated benzene ranging from over the range of $C_6Li_{6-n}H_n$ where $n = 1$ to 6. At room temperature the species of highest yield is dilithiobenzene. As one raises the temperature progressively to $800^{\circ}C$ a

$$CCl_{4(g)} + Li_{(g)} \xrightarrow{\;(800\text{-}1000°C)\;} \underset{(12\text{-}18\%)}{CLi_4} + \underset{(60\%)}{C_2Li_4} + \underset{(20\%)}{C_2Li_2}$$

$CLi_4 \xrightarrow{D_2O} CD_4$ (20.05639)

$CLi_4 \rightarrow C[Si(CH_3)_3]_4$

$\gamma = 9.80$

$C_2Li_4 \xrightarrow{D_2O} C_2D_4$ (32.05640)

$C_2Li_4 \rightarrow C_2[Si(CH_3)_3]_4$

C. Chung and R.J. Lagow, Chem. Comm. 1078 (1972)

Fig. 1

$$C_2Cl_{6(g)} + Li_{(g)} \xrightarrow{(800-1000°C)} C_2Li_6$$

80%

$$C_2Li_6 \xrightarrow{D_2O} C_2D_6$$

(36.08444)

$$C_2Li_6 \xrightarrow{ClSi(CH_3)_3} C_2[Si(CH_3)_3]_6$$

C. Chung and R.J. Lagow.

Chem. Comm. 1078, (1972)

Fig. 2

Fig. 3

$$C_{(s)} \xrightarrow{2500^\circ - 3000^\circ C} C_1, C_2, C_3, C_4, C_5, C_{6(g)}$$

$$C_{3(g)} + 4Li_{(g)} \xrightarrow{900^\circ C} C_3Li_4 \ (40\text{-}65\%)^*$$

$$C_2Li_4 \ (15\text{-}40\%)^*$$

$$CLi_4 \ (0\text{-}10\%)^*$$

$$C_2Li_2 \ (10\text{-}30\%)^*$$

$\downarrow ClSi(CH_3)_3$

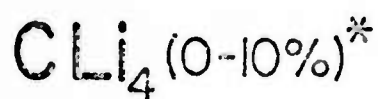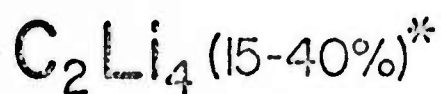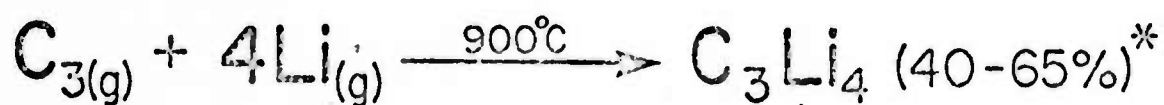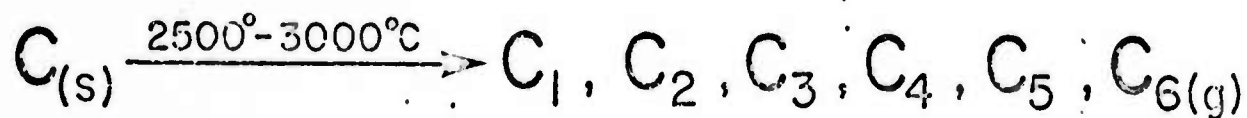$(CH_3)_3Si$ — $Si(CH_3)_3$

$C=C=C$

$(CH_3)_3Si$ — $Si(CH_3)_3$
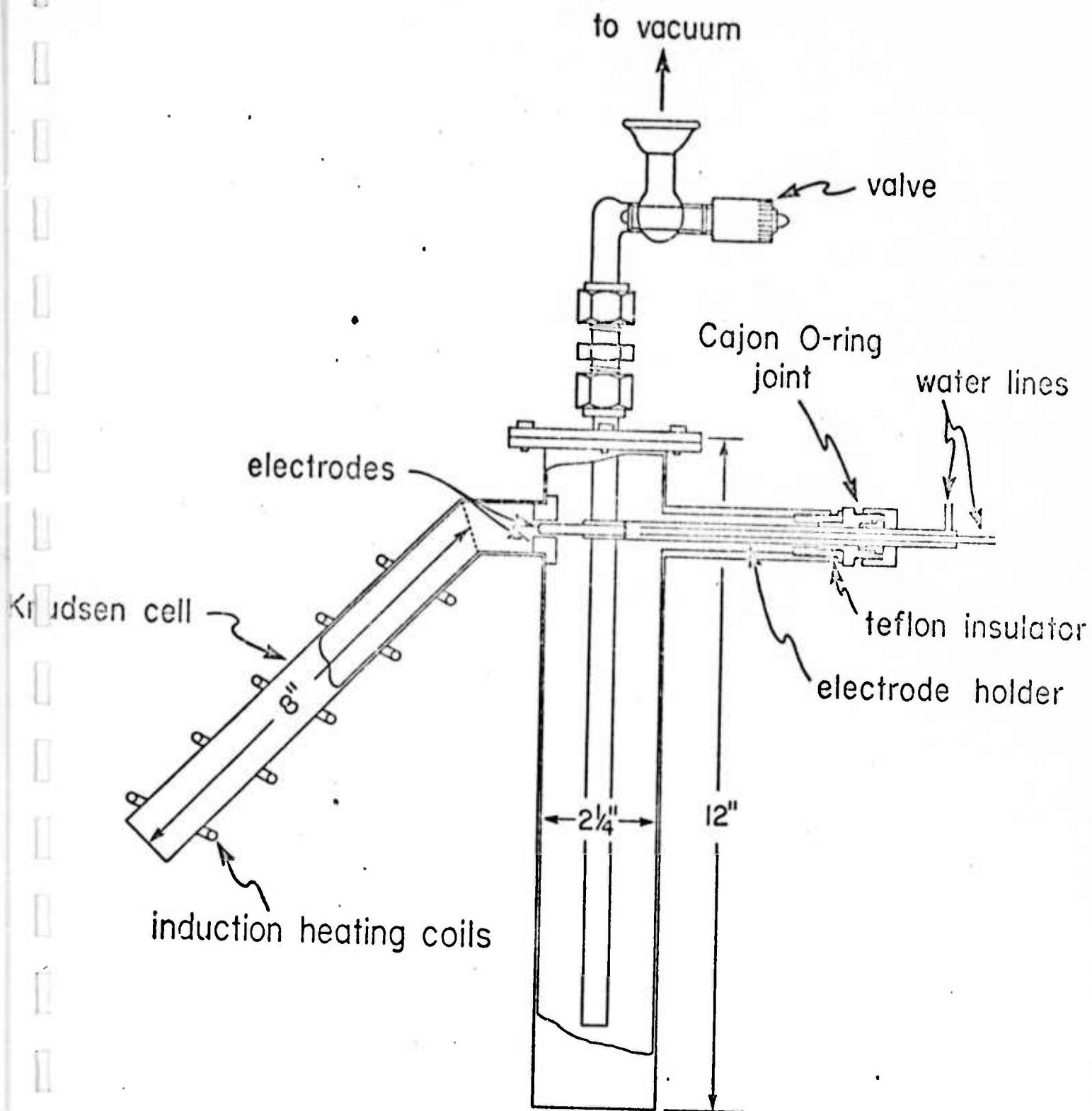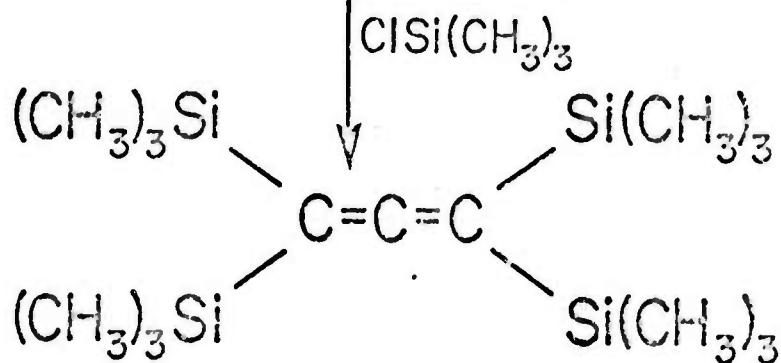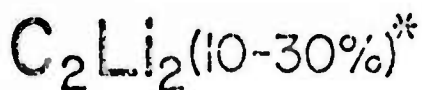
$\mathcal{T} = 9.89$

*Based on Carbon Vaporized

L. A. Shimp and R. J. Lagow, J. Am. Chem. Soc. 95, 1343 (1973)

Fig. 4

shift toward the higher benzene polylithium compounds is noted. The temperature of the benzene is raised to 900°C and a striking new result is attained. One begins to obtain polylithiated cyclohexanes from the benzene starting material. This results from a tendency for the lithium to add to the double bonds as well as replace the protons on the ring. Studies were made up to temperatures of 1200°C producing such striking compounds as perlithiocyclohexane and $C_6Li_6H_6$. It has been found subsequently that the reaction of hexachlorobenzene with lithium provides a much cleaner route to hexalithiobenzene.[4]

The reaction of methane gas with lithium has also been extensively investigated.[5] We predicted and found that lithium at 1000° will not react with methane gas at room temperature. The activation energy for this reaction appears to be in the 30 kcal mole range. Lithium at 1000°C usually has about 3 kcal mole of translational or kinetic energy and only a very small percentage of lithium in the first excited electronic state. Therefore, the activation energy for the lithium-methane reaction is not likely to be available under these reaction conditions. The reaction between methane and lithium would be a very important one for the production of tetralithiomethane which we consider to be one of the important materials in subsequent polymer synthesis. We have used several approaches to provide the activation energy for this reaction. We have found that if we either electronically excite the lithium or vibrationally excite the methane the reaction proceeds in a satisfactory manner. We have conducted an experiment in which the methane was heated to 900°C and obtained satisfactory results. Increased temperatures populate higher vibrational states in the methane and thus allow a very significant decrease in the activation energy of the reaction. We also used a radio frequency source to excite the lithium vapor electronically and produced a successful reaction. Still another piece of work has been done using a methane plasma source which vibrationally excites the methane and allows the reaction to proceed. The most important result in this area is discussed in the "newest results" section and involve the study of the reaction of lasar induced electronically excited lithium.

In the study of tetralithiomethane, a fourth synthesis is being completed which involves initial synthesis of dilithiomethane and subsequent pyrolysis to give a substantial yield of tetralithiomethane.[6] Using this method we have obtained substantial quantities of tetralithiomethane.

Extensive work has been done on solvent systems for tetralithiomethane so that one may do the polymer synthesis in solution   Several successful solvent systems are being developed and the concentrations of the poly-lithium compounds in solution are being determined by NMR studies and the preparation of derivatives.

An extensive study has been recently completed on the reactions of olefins with lithium vapor.[7] (See Figure 5.) A large number of new polylithium compounds such as tetralithio cyclohexadiene, 2,3 dilithio 2 butene, 2,3 tetralithio 2 butene, 1,2 dilithio isobutane, 1,4 dilithio 2 butene, and 1,2 trilithio isobutane have been prepared in this study. We have seen instances of both substitution for hydrogen on sites requir-ing a low activation energy for reaction and addition to double bonds. This study has established another general route to polylithium compounds.

Studies of reactions of inorganic species with lithium have also been undertaken. The reaction of silicon tetrachloride, $SiCl_4$, with lithium has been recently studied and the polylithium compound $SiLi_4$ was obtained in good yield.[8] Hydrolysis and deuterolysis of the compound produced silanes and perdeutero silanes. A subsequent study of the reac-tion of tetralithiosilane with methyl chloride resulted in a 15 per cent yield of tetramethyl silane indicating that the $SiLi_4$ is also a potential monomer. The reaction of BCl_3 and PCl_3 are currently under study. A fair yield of trimethylborane $B(CH_3)_2$ was obtained from the reaction of BLi_3 with methyl chloride. Additionally the synthesis of polylithiated car-boranes has been attempted and a workup is now in progress. Isolation of a higher purity $SiLi_4$ is being undertaken. It should be pointed out that if the diamond syntheses from tetralithiomethane are successful, a syn-thesis of a silicon analog for a diamond will be attempted using the $SiLi_4$. Such a diamond-like silicon structure would have many unusual electrical and physical properties. This type of structure has been the object of numerous unsuccessful synthetic studies utilizing the phase dia-gram of silicon. This potentially valuable species has previously eluded all other synthetic approaches.
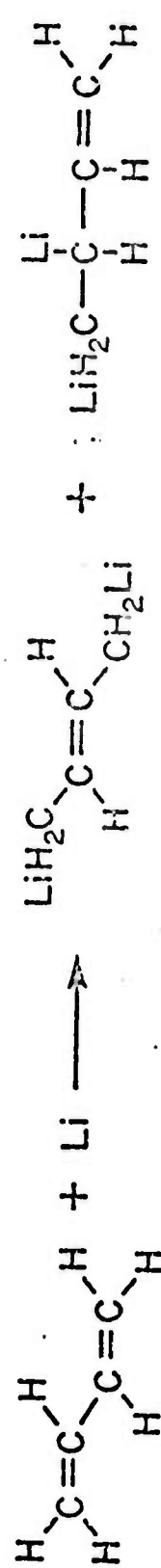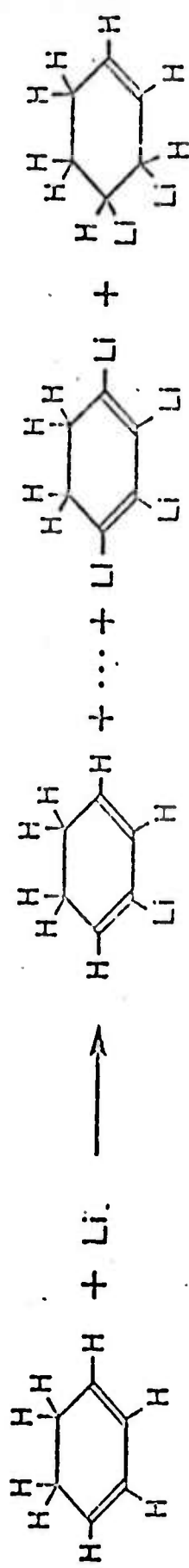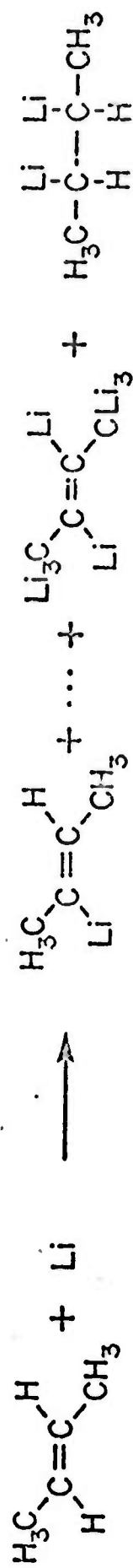
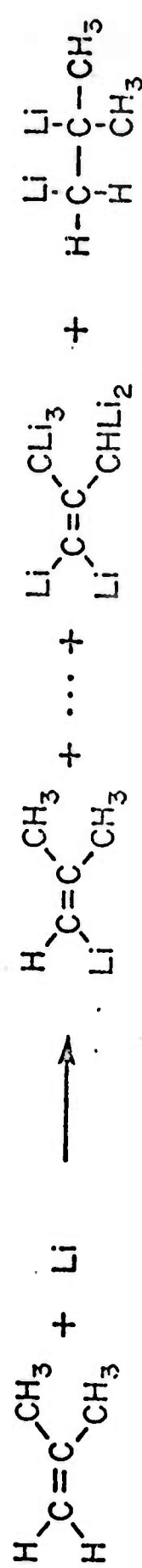# Major Products of the Reaction of Lithium with Alkenes

Fig. 5

6

Most Recent Results

One of the most exciting recent results in this area is the synthesis of the first polylithium ethers. $C_3Li_7OC_3Li_7$ has been prepared recently and is being characterized. This development opens many possibilities in the polymer area such as using structures with ether linkages as monomers and the possibility of obtaining other oxygen containing polylithium compounds.

Another completed study[9] has indicated that perlithiocarbons may be obtained by the reaction of lithium vapor with partially chlorinated hydrocarbons. Perlithio propane C_3Li_8 has been obtained from several monochloro isomers. Similar reactions have produced other novel polylithium compounds. These results suggest that the replacement of a halogen by lithium is so exothermic, that the activation energy required for the lithium to abstract hydrogen is available. The result is similar to that obtained with a vibrationally excited alkane and suggests vibrational excitation.

Recently structural studies have been initiated on several polylithium compounds. We have been interested in the lithium and carbon 13 NMR spectra and the laser-raman spectra of polylithium compounds both in solution and in the solid state. Very encouraging results have been obtained. Such studies will also lead to accurate methods for determination of concentration of reactive polylithium intermediates in solution and for identification of polylithium compounds.

A major breakthrough[10] of great significance in synthetic chemistry and of prime interest in physical chemistry has come about through a collaboration with Professor J. S. Steinfield of our department. Lithium vapor generated at $1000^\circ C$ has been selectively excited to the first excited electronic state (1.56 ev above ground state) with a tunable dye laser in 80 per cent yield. This electronically excited lithium has been found to react very efficiently with methane in contrast to no reaction at all when lithium is in the ground state. This reaction opens a whole new field of synthetic chemistry: the reaction of electronically excited lithium vapor. This chemistry will surely differ greatly from the chemistry of lithium vapor in the ground state. This event is also very significant because it is believed to be the first study of any synthetic reaction of a selectively electronically excited metal vapor and because it may provide input into synthetic routes to CLi_4 and C_2Li_6.

1. C. Chung and R. J. Lagow, "The Reaction of Lithium Atoms at 1000°C with Chlorocarbons; A New Route to Polylithium Compounds", Chem. Comm. 1079 (1972).

2. L. A. Shimp and R. J. Lagow, "The Reaction of Carbon Vapor with Lithium Atoms; A Direct Synthesis of Polylithium Compounds". J. Amer. Chem. Soc. 95, 1343 (1973).

3. L. A. Shimp, C. Chung, J. A. Morrison and R. J. Lagow, "The Reaction of Lithium Vapor with Benzene." J. Am. Chem. Soc. (in press).

4. L. A. Shimp and R. J. Lagow, "The Synthesis of Hexalithiobenzene" (to be published).

5. L. A. Shimp and R. J. Lagow, "The Reaction of High Temperature Lithium Vapor with Methane", submitted to J. Am. Chem. Soc.

6. J. A. Morrison and R. J. Lagow, "A New Synthesis for Tetralithiomethane", submitted to J. Am. Chem. Soc.

7. J. A. Morrison, C. Chung and R. J. Lagow, "The Reaction of High Temperature Lithium Vapor with Olefins; A Synthesis for Polylithium Compounds", J. Am. Chem. Soc., Feb. (1975) (in press).

8. J. A. Morrison and R. J. Lagow, "The Synthesis of $SiLi_4$, $GeLi_4$ and BLi_3" (manuscript in preparation).

9. L. G. Sneddon and R. J. Lagow, "The Reaction of Chloroalakanes with High Temperature Lithium Vapor", submitted to J. Am. Chem. Soc.

10. R. J. Lagow, L. A. Shimp, F. Lucer and J. S. Steinfield, "The Reaction of Lasar Induced Electronically Excited Lithium with Methane", (manuscript in preparation).

Introduction

A large amount of research has been conducted over the last twenty to thirty years on the production, characterization, and physical properties of high temperature vapor species formed by evaporation of solid elements and compounds. The species have been identified by their ultraviolet, infrared, microwave, electron spin resonance and mass spectras and studies have been made of their electronic structure, rotational, vibrational and electronic energy levels, their geometry (in the case of molecular species), vapor equilibrium, and other thermodynamic properties. As a result of this work, methods and apparatus now exist for the evaporation of at least a gram per hour of most materials at temperatures up to 3500^0C and pressures of 10^{-6} torr or lower.

The species produced by these methods are in general extremely reactive high energy species which often undergo novel chemical reactions not characteristic of the elements in the condensed phase at lower temperatures. Use of these species for chemical synthesis has been neglected until the last few years when more investigators have begun to appreciate the potential of these techniques, yet most of the promising systems are unexplored. Pioneering work was done by Skell[1] with carbon and silicon atoms and Timms[2] with

boron, iron, nickel, copper and silver atoms and Margrave with SiF$_2$ species[3].

Two of the convenient experimental apparatus for producing the desired species are electron bombardment heating using a Varian "e-gun" to evaporate a rod under high vacuum, and evaporation using a Knudsen cell containing the sample in an inert crucible or boat. In the second method electrical resistance or induction heating is used. This method is probably the most versatile since it is easily scaled up to where many grams of sample may be evaporated over a short period of time and one also has a more certain knowledge of the temperature of the system.

Status of the Field

Recently there has been a surge of interest in polylithium compounds because one conventional synthetic route has been found which is capable of producing special types of unsaturated species from starting materials which are structurally similar. This route involves the reaction of butyl lithium or a mixture of butyl lithium and tetramethylenediamine with special types of un- saturated organic systems in solution. The synthesis of tetralithio- allene, Li$_2$C = C = CLi$_2$, from propyne in with this technique was re- ported by West[4] and coworkers. Subsequently they were able to lithiate several more acetylenic species, and species which were isostructural with acetylene[5,6]. This work, although not a general synthesis, was

B

D

$11\frac{3}{4}"$

C

A

6"

$1\frac{1}{2}"$ O.D.
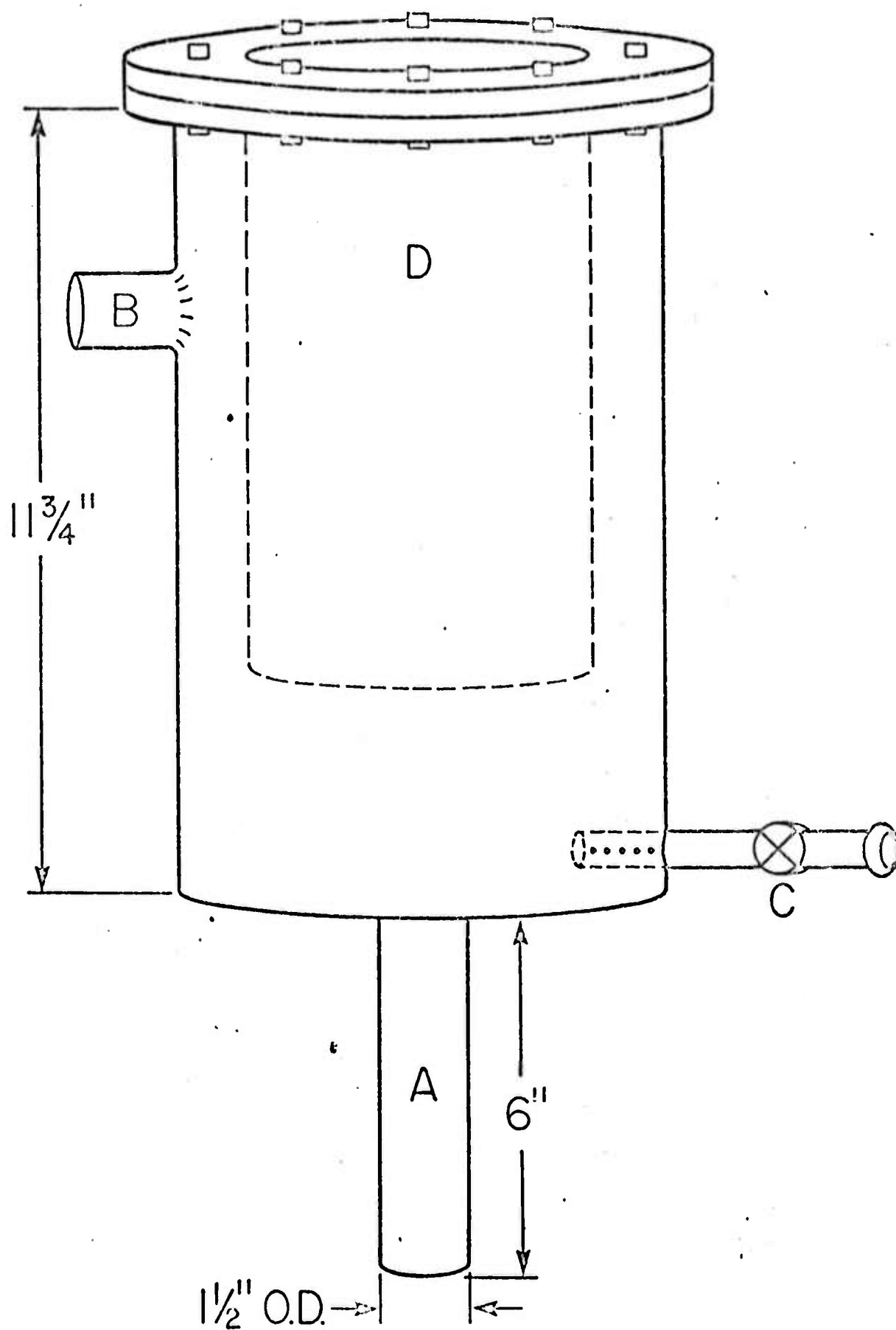
Inverted Dewar Type Reactor

Fig. 6

an outstanding contribution. Other workers have used this technique to produce interesting polylithium compounds.[7,8]

Lithium Atoms

Matrix isolation studies on a very small scale of molecules formed by lithium atom reactions have been reported by Andrews and Pimentel.[9] Novel species such as the trichloromethyl radical, lithium nitrocide (LiON), and lithium superoxide (LiO_2) have been formed by the reaction of Lithium atoms with carbon tetrachloride, nitric oxide, and oxygen matrices respectively. The hot lithium atoms, as indicated by the products obtained, are very reactive and sufficient energy is available to overcome activation energies with many reactants. The lithium vapor at room temperature has a free energy of formation of + 30.6 Kcal/mole relative to the solid metal at 298^0K. We have found that lithium atoms have an extensive chemistry and a reaction is obtained with almost any reactant.

Experimental

Lithium atoms may be generated from lithium metal using a Knudsen cell apparatus of stainless steel maintained at a temperature of 800^0 - 1000^0C. A simple apparatus which we have used in some of our initial studies is illustrated in fig. 6. In this range of

temperature less than .4% Li_2 species are produced. The lithium vapor diffusing out of the cell is then routed to various reaction chambers. An elaborate vacuum line is then used for separation of volatile products. The lithium compounds produced are very unstable to water, and air, making dry box work and other special handling techniques necessary.

When gaseous reactants are involved, the reaction may be carried out in the gas phase. Different products have been obtained from the same system as one varies both the temperature of the reactant and the lithium atoms. Lithium atoms may also be reacted with compounds which are solids and liquids at room temperature because the singlet-triplet reactivity problems which are encountered in many other high temperature systems are not a factor in lithium atoms.

Recent Progress and Proposal for Further Work

During the past year, the unusual new compounds tetralithiomethane, CLi_4; hexalithioethane, C_2Li_6; hexalithiobenzene C_6Li_6 and tetralithioethylene C_2Li_4 have been prepared and characterized in our laboratory. One communication is in press in Chemical Communications and is included as an item in this proposal, and two more communications and one full paper are in preparation. The

reactions of chlorocarbons with excess lithium atoms at 800°C have been extensively studied in our laboratory during the past year. The preparation of polylithium compounds from chlorocarbons in solution has been precluded by the formation of certain reactive intermediates, by the elimination of LiCl. such as dichlorocarbene, which react with the solvent present. We have used a large excess of lithium vapor under high vacuum conditions to prevent reaction of intermediates with species other than atomic lithium.

The reaction of carbon tetrachloride with excess lithium atoms at 800° in an inverted Dewar reactor (fig. 1) has produced the poly-lithiated products tetralithiomethane and tetralithioethylene. The yield of tetralithiomethane was 18% with a 61% yield of tetralithio-ethylene based on CCl_4. The detail of this synthesis may be found in the communication. The products were characterized by reaction with D_2O yielding CD_4 and C_2D_4, the expected hydrolysis products. These species

$$C(Li)_n + nD_2O \rightarrow C(D)_n + nLiOD$$
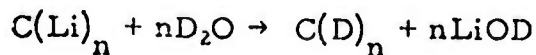
were identified on a double focusing high resolution CEC-21-110B mass spectrometer. The polylithium compounds were also characterized by preparing trimethylchlorosilane derivatives. The compounds $C(SiMe_3)_4$ and $C_2SiMe_3)_4$ were prepared in this manner and characterized by high resolution mass spectroscopy and proton N. M. R.

The reaction of C_2Cl_6 with excess lithium atoms produced C_2Li_6 in 80% yield based on C_2Cl_6. The product was characterized by deuteration with D_2O to produce C_2D_6 and by derivatization with $ClSi(Me)_3$ to produce $C_2(SiMe_3)_6$. These resulting products were characterized by high resolution mass spectroscopy and by N.M.R.

We have also conducted experiments in which hydrocarbons were the reactants. The reaction of benzene with lithium vapor at 1000^0C has been extensively studied. A 10% yield yield of hexalithiobenzene C_6Li_6 has been obtained along with higher yields progressively of C_6Li_5H through C_6LiH_5. The products of this reaction have also been deuterated and their derivatives with trimethylchlorosilane have been prepared.

We have established that the reason that only 10% yield of hexalithiobenzene is obtained using an excess of lithium is that only the electronically excited lithium atoms have the activation energy necessary to react with benzene. The activation energy for the reaction of lithium atoms with hydrocarbons such as methane or benzene is in the range of 25 to 35 k cal./mole. The first excited state of Li is 1.94 eV above the ground state. A reactor which uses a strong radio frequency field to excite the lithium atoms as they effuse from the Knudsen cell has been designed and is in operation

in our laboratory. Preliminary indications are that the yields are significantly higher.

We are devoting a large effort at present toward finding satisfactory solvents for these new reactive polylithium compounds. If our search is successful, the derivative chemistry of these species will be greatly enhanced and many of their potential applications will be closer to realization. We have found two solvents in which the compounds are soluble without reaction for short periods of time. We are currently trying to obtain Li N.M.R. spectra in these solvents.

The potential for important applications of polylithium compounds which solve existing materials problems is very high and we propose to explore many promising areas. The most intense efforts in this program will be the synthesis of new polylithium compounds and the synthesis of new materials from these polylithium compounds.

1. We propose to open a general route to the synthesis of polylithium compounds from corresponding hydrocarbons by developing the technique we have used to obtain the electronically excited lithium atoms in the benzene reaction. Using this radio frequency excitation technique we shall prepare a number of interesting perlithiocarbons including polymeric species.

2. We shall study the reaction of lithium atoms with a series of halocarbons to obtain new polylithium compounds which appear to have potential as intermediates in the synthesis of new materials.

3. Recently, we have found two solvents in which the compounds are soluble for short periods of time without reaction. We are initiating a series of lithium N.M.R. studies in these solvents for structural information and to use as a tool for characterization of these species. We are also initialing a series of Raman vibrational spectral studies to the same ends. The Raman spectra may be obtained in the solid phase or liquid phase using a Raman-laser spectrometer.

4. We are studying the reaction of methane with lithium atoms at 1000^0C in a reactor designed for methane to enter the lithium vapor after passing through a furnace at 1000^0C. Based on Janaf table equilibrium data, methane is unstable above 900^0C. We hope to produce vibrationally excited methane which will react with thermal lithium atoms to give tetralithiomethane. The success of this technique would open a new route to polylithium compounds and provide an alternate synthesis for tetralithiomethane.

5. In another experiment it is proposed to excite the methane in a low temperature radiofrequency glow discharge before reaction with lithium atoms to compare the results with the technique proposed in item four.

6. It is well known that when carbon is vaporized at very high temperatures using a carbon arc between graphite rods that atomic

and polyatomic carbon species are formed containing species C_1 to C_6. Carbon atoms (C_1) are the specie of highest concentration. It has been shown by Skell[10] that carbon atoms are highly reactive species capable of insertion into carbon-carbon bonds. We propose to study the reaction of these carbon species with high temperature lithium atoms.

7. We have conducted some preliminary studies which have indicated that high temperature lithium vapor will selectively react with double bonds in unsaturated hydrocarbon species. We propose to explore this type of reaction.

8. We have found that hydrocarbons with several specific chlorinated sites will react with lithium vapor under mild conditions to selectively lithiate these sites. The desirability of polylithium compounds of this type will become obvious as the potential applications are subsequently discussed. We propose to explore this aspect thoroughtly.

9. We have made preliminary studies of the reactions of lithium vapor with inorganic halides such as $SiCl_4$ and $SnCl_4$. Very reactive compounds result which may be $SiLi_4$ and $SnLi_4$. Many possibilities exist in this area for new compounds, inorganic polymers, and synthetic applications.

10. It is proposed that such species as perlithiocyclohexane, perlithioorganic polymers, perlithiographite, perlithioadamantane,

perlithionapthalene and perlithioanthracene be sought for potential as synthetic intermediates in materials synthesis.

Synthetic Applications for New Polymeric Materials

11. CLi_4 species is in effect a "captive carbon atom" which should react with most RX species to produce species with C-R bonds such as CR_4 where X is I, Br, or Cl. Tetralithiomethane will almost surely become an important reagent in organic synthesis due to its simple and basic structure. It is proposed that the reaction of RX_2 species with CLi_4 be investigated in search of new three dimensional polymers. One might expect that many of these rigid three dimensional polymers would have many characteristics similar to diamond such as thermal stability and similar physical properties. This rigidity would be expected because each carbon atom from tetralithiomethane would be the site of four equivalent interlocking polymer chains. The types of R groups one could select might vary from linear species to aromatic species such as paraiodobenzene. Also CLi_4 or CH_2Li_2 may be used to crosslink halogen containing polymers and elastomers. Many other polylithium compounds should possess the same capability. Hexalithiobenzene, for example, may react with RX_2 species to produce a polymer system based on six extending chains. If this type of reaction works, the applications are unlimited. Also, CH_2Li_2 may be used to

prepare linear polymers and elastomers.

12. The compound tetrathioethyler which we have already prepared and characterized might be of som interest as a synthetic intermediate. $Li_2C = CLi_2$ may react with RX compounds to produce symmetrically substituted ethylenes which may then be polymerized to produce new polymers.

13. We propose to apply the techniques which are generated in this program to produce perlithiated and partially lithiated polymers and polymer surfaces from both hydrocarbon and halocarbon polymers by direct reaction of these materials with lithium atoms. Studies of reactions of lithium atoms with monomers and polymers during gas phase polymerizations may also be studied. The lithium-carbon bonds produced in polymers would serve as sites for further chemistry on the polymer system. New functional groups and side branches may then be added to the polymer chain or surface. The polymers may also become highly crosslinked by reaction with RX_2 species where RX_2 could be exotic species such as para iodobenzene (I-⬡-I).

14. High pressure - high temperature reactions between per-lithiated species such as perlithiated anthracene or adamantane and perfluorinated anthracene or adamantane (both of which have recently been prepared in our laboratories) will be conducted in an attempt to make diamond. This chemical synthesis of diamond should occur

under much less extreme conditions than the graphite diamond "brute-force" synthesis because the carbon is already in sp^3 tetrahedral coordination and a considerable amount of energy is released when lithium fluoride is formed. A relatively high pressure will be necessary (~ 20 - 30 kilobars) in order to insure a close-packed configuration to promote bonding. Excess lithium may also serve as a solvent to facilitate faster diamond formation.

15. An important part of the presently used process for producing man-made diamonds involves the breakdown of the graphite lattice and an "atom by atom transport" of carbon through a molten transition metal solvent to be deposited in the tetrahedral lattice of the growing diamond crystal.[11] In the case of a tetralithiomethane solution in molten lithium, the carbon atoms are already in an sp^3 configuration and the energy required to break apart the graphite lattice in the conventional synthesis is not necessary. It is very possible that a simple high temperature, high pressure experiment in a tetrahedral anvil with this system would result in a more facile diamond synthesis.

16. It is possible that many dilithiated species could be used as conventional monomers for reaction with RX_2 species.

17. Polylithium compounds may be useful as catalysts in chemical processes. The number of organometallic catalysts now

in use is large and intuitively it would appear that many of these polylithium compounds should have potential in this area.

————————

The initial funding for this project came as "seed money" from the Advanced Research Projects Agency through the M. I. T. Center for Materials Science and Engineering. We are very excited about this field of research and we urgently need funds to expand our efforts to a three-man team in this area. We really can't imagine an area with higher potential for materials application.

References

1. P. S. Skell and P. W. Owen, J. Am. Chem. Soc., 89, 3933 (1967); P. S. Skell, L. D. Wescott, J. P. Goldstein and R. R. Engel, ibid., 87, 2829 (1964).

2. P. L. Timms, Chem. Commun. 258 (1968); P. L. Timms, Endeavor 27, 133 (1968).

3. J. L. Margrave, P. L. Timms, R. A. Kent, and T. C. Ehlert, J. Am. Chem. Soc. 87, 2824 (1965).

4. R. West, P. A. Carney, and I. C. Minco, J. Am. Chem. Soc. 87 3788, (1965).

5. R. West and P. C. Jones, J. Am. Chem. Soc. 91, 6156 (1969).

6. R. West and G. A. Gornowicz, J. Am. Chem. Soc. 93, 1714 (1971); J. Am. Chem. Soc. 93, 1720 (1971).

7. M. D. Raush and D. J. Ciappenelli, J. Organometal. Chem. 10 127 (1967).

8. A. F. Halasa and D. P. Tate, J. Organometal. Chem. 24, 761 (1970); J. Organometal. Chem. 31, 369, (1971).

9. W. L. S. Andrews and G. C. Pimentel, J. Chem. Phys. 44, 2361 (1966); L. Andrews, ibid., 48, 972 (1968); L. Andrews, J. Am. Chem. Soc. 90, 7368 (1968).

10. P. S. Skell and R. R. Engel, J. Am. Chem. Soc. 87, 1135 1965.

11. H. T. Hall, J. Chem. Educ., 38, 484 (1961).